

VOLUME 29

MARCH, 1951

NUMBER 2

# Canadian Journal of Physics

*Editor:* G. M. VOLKOFF

*Published by* THE NATIONAL RESEARCH COUNCIL  
OTTAWA CANADA

## CANADIAN JOURNAL OF PHYSICS

This was formerly *Section A, Canadian Journal of Research*. The change to the new name took place January 1, 1951. The CANADIAN JOURNAL OF PHYSICS is published six times annually.

The CANADIAN JOURNAL OF PHYSICS is published by the National Research Council of Canada under the authority of the Chairman of the Committee of the Privy Council on Scientific and Industrial Research. Matters of general policy are the responsibility of a joint Editorial Board consisting of members of the National Research Council of Canada and the Royal Society of Canada.

The National Research Council of Canada publishes also the following Journals: *Canadian Journal of Botany, Canadian Journal of Chemistry, Canadian Journal of Medical Sciences, Canadian Journal of Technology, Canadian Journal of Zoology*.

### EDITORIAL BOARD

<i>Representing</i>	<i>Representing</i>	
NATIONAL RESEARCH COUNCIL	ROYAL SOCIETY OF CANADA	
DR. H. P. ARMES ( <i>Chairman</i> ), Emeritus Dean of Arts and Science, University of Manitoba, Winnipeg, Man.	DR. G. M. VOLKOFF, Professor of Physics, University of British Columbia, Vancouver, B.C.	} Section III
DR. OTTO MAASS, Macdonald Professor of Physical Chemistry, McGill University, Montreal, P.Q.	DR. J. W. T. SPINKS, Dean, College of Graduate Studies, University of Saskatchewan, Saskatoon, Sask.	
DR. J. H. L. JOHNSTONE, Professor of Physics, Dalhousie University, Halifax, N.S.	DR. H. S. JACKSON, Head, Department of Botany, University of Toronto, Toronto, Ont.	
DR. A. BERTRAND, Professor of Bacteriology, Faculty of Medicine, University of Montreal, Montreal, P.Q.	DR. E. HORNE CRAIGIE, Department of Zoology, University of Toronto, Toronto, Ont.	} Section V
<i>Ex officio</i>	<i>Representing</i>	
DR. LÉO MARION, <i>Editorial Adviser</i> , Division of Chemistry, National Research Laboratories, Ottawa.	THE CHEMICAL INSTITUTE OF CANADA	
DR. H. H. SAUNDERSON, Director, Division of Information Services, National Research Council, Ottawa.	DR. H. G. THODE, Department of Chemistry, McMaster University, Hamilton, Ont.	

Subscription rate: \$2.00 a year. Special rates can be obtained for subscriptions to more than one of the Journals published by the National Research Council. All enquiries concerning subscriptions should be addressed to the CANADIAN JOURNAL OF PHYSICS, National Research Council, Ottawa, Canada.







# Canadian Journal of Physics

Issued by THE NATIONAL RESEARCH COUNCIL OF CANADA

VOLUME 29

MARCH, 1951

NUMBER 2

## THE ABSORPTION OF MICROWAVES IN EXCITED HYDROGEN<sup>1</sup>

By G. E. REESOR<sup>2</sup>

### Abstract

Direct absorption measurements were made upon excited atomic hydrogen in a discharge tube placed inside a wave guide. Two ranges of wave lengths in the 3 cm. region were investigated. The results can be satisfactorily explained by absorption due to free electrons. Although the  $2s\ ^2S_{1/2}$  to  $2p\ ^2P_{3/2}$  transition of atomic hydrogen is in this region, no selective absorption was observed.

### Introduction

The energy levels of the hydrogen atom for the second quantum state as calculated by the Dirac theory are shown in Fig. 1(a). Since transitions are allowed between levels of the same principal quantum number  $n$ , then according to the selection rules for electric dipole radiation, a transition between the  $2s\ ^2S_{1/2}$  and the  $2p\ ^2P_{3/2}$  levels is permissible. This transition has a wave number

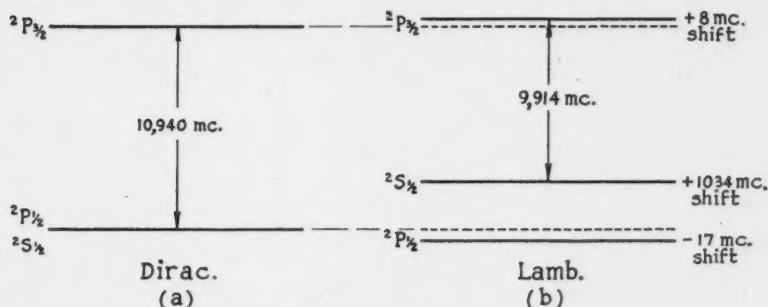


FIG. 1. Energy levels of the hydrogen atom for the  $n = 2$  quantum state as predicted by Dirac and as determined by Lamb.

of  $0.365\text{ cm.}^{-1}$  which corresponds to a wave length of 2.74 cm. Thus microwave energy of wave length 2.74 cm. or frequency 10,940 mc. should be absorbed by atoms in the  $2s\ ^2S_{1/2}$  state, causing them to jump to the  $2p\ ^2P_{3/2}$  state.

<sup>1</sup> Manuscript received in original form July 18, 1950, and, as revised, November 9, 1950. Contribution from the McLennan Laboratory, Department of Physics, University of Toronto, Toronto, Ont.

<sup>2</sup> Holder of two Fellowships under the National Research Council of Canada, 1945-47. Now at Ferranti Electric Limited Research Department, Toronto, Ont.

Recent experiments performed by Retherford and Lamb (11) indicate that the energy levels are shifted from the positions predicted by the Dirac theory. This shift has been shown to be due to interaction of the electron with the radiation field (2) and resulting levels are shown in Fig. 1(b). This indicates that an electromagnetic wave of frequency 9914 mc. would be absorbed. The results of Retherford and Lamb show better agreement with the fine structure components of the  $H_\alpha$  line found spectroscopically. Although it is most probable that the energy separation is close to 9914 mc., absorption measurements were also made in the region of 10,940 mc.

The amount of absorption that might reasonably be expected was calculated. This required an estimate of the fraction of the total number of molecules in the discharge which give rise to atoms in the  $2s\ ^2S_{1/2}$  state. Estimates of this fraction for a similar hydrogen discharge reported by Carst and Ladenburg (4) and by Haase (6) differ by a factor of  $10^5$ . A calculation based on Carst and Ladenburg's estimate, the more favorable of the two, indicated that the absorption might just be on the borderline of possible measurement. The importance of a direct measurement of this energy separation justified an attempt to measure the absorption even though success was doubtful.

The natural breadth of the absorption line was calculated from the mean lives of the energy levels from which it arises. It was found to be 100 mc. The Doppler broadening of the line is less than 1 mc. which is negligible compared with the natural breadth. Since the line breadth is so great, the conventional sweep frequency methods of microwave spectroscopy cannot be used. It is therefore necessary to use fixed frequency methods. Any method of producing excited hydrogen atoms in large numbers will also give rise to ions and free electrons. These ions and free electrons will absorb microwave energy resulting in a continuous background of absorption.

Early attempts by other workers (3, 6, 7) to detect microwave absorption in excited hydrogen were unsuccessful. The development of microwave techniques made possible more refined absorption experiments. Lamb and Retherford (8, 9) obtained their results by a microwave method but did not measure absorption directly.

### Apparatus

The experiment required the production of as high a concentration of excited hydrogen atoms as possible in a container through which microwave energy could be passed. An electrodeless discharge tube placed inside a wave guide was used for this purpose. The amount of energy absorbed was measured at two ranges of frequencies. Fig. 2 is a block diagram of the whole apparatus.

Microwave energy was supplied by a klystron pulse modulated at a frequency of 60 c.p.s. with a pulse about 20 microseconds wide. The modulator supplied a keying pulse for a high speed oscilloscope on which output levels were displayed.

The main components of the wave guide transmission line and measuring equipment block are shown in Fig. 3. The variable attenuator was calibrated at the frequencies used and measured differences of attenuation with an accuracy of considerably better than 0.1 db. A small fraction of the energy

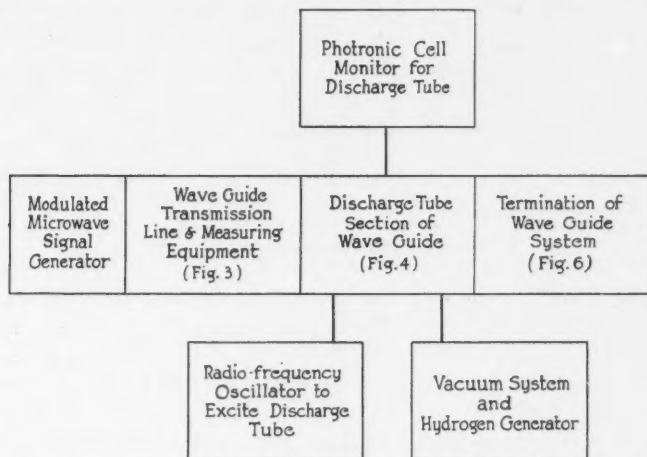


FIG. 2. Block diagram of the apparatus.

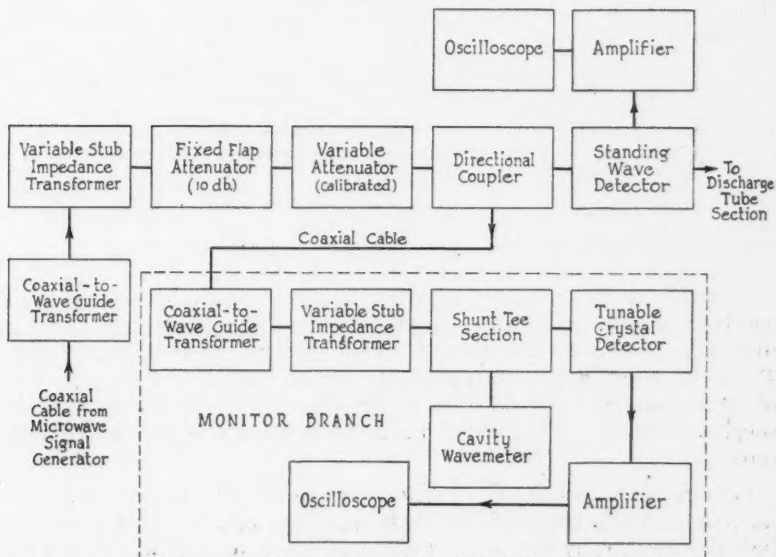


FIG. 3. Block diagram of wave guide transmission line and measuring equipment.

was fed through a directional coupler to a monitor branch. The standing wave detector which followed the directional coupler was used in conjunction with the variable attenuator for all standing wave measurements.

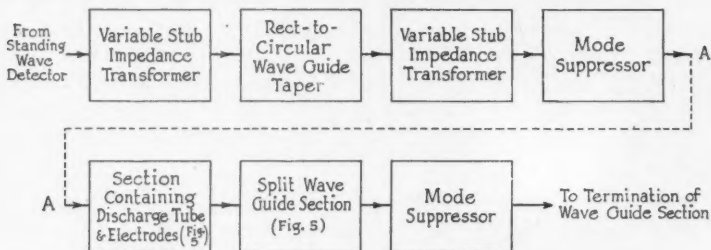


FIG. 4. Discharge tube section of wave guide.

The components of the next block in Fig. 2 containing the discharge tube are shown in Fig. 4. The size of the circular wave guide surrounding the discharge tube was chosen so that energy could be transmitted in the  $H_{11}$  mode only. The rectangular guide was transformed to the circular guide by a tapered section.

External electrodes were used to avoid as much as possible placing obstructions in the wave guide. These electrodes were insulated sections of wave guide placed at either end of the discharge tube as shown in Fig. 5. To avoid leakage of microwave energy at the spaces insulating the electrodes, circular chokes and flanges were used.

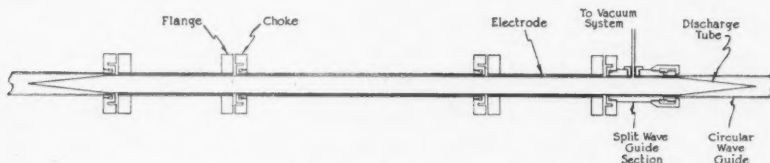


FIG. 5. Discharge tube and external electrodes showing split wave guide section.

A connection to the pumping system was brought out through a small opening in a section of split wave guide following the second electrode. Owing to imperfections in the circular wave guide, elliptical modes were produced. These were minimized as much as possible by rotating the individual sections of circular guide and the remaining effects were eliminated by means of mode suppressors placed at either end of the circular section containing the discharge tube.

For measurements using the standing wave method, the wave guide system was terminated by means of a solid plunger whose position could be varied. For measurements by the comparison method the wave guide was terminated in the detector system shown in Fig. 6.

The discharge tube as shown in Fig. 5 was made of 20 mm. O.D. Pyrex tubing with tapered ends to avoid reflection of microwave energy. The connection to the vacuum system was made through a small diameter side tube as mentioned above. The inside walls of the discharge tube were coated with a 5% solution of phosphoric acid before evacuation. This increased the concentration of atomic hydrogen.

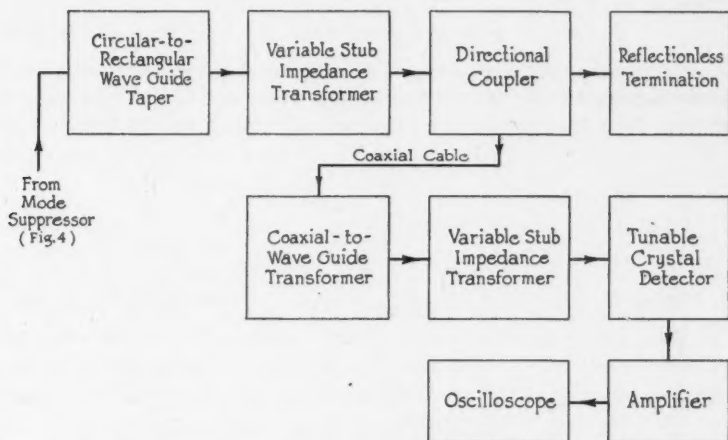


FIG. 6. Termination of wave guide system for comparison method of attenuation measurement.

The discharge tube was excited by a radio-frequency oscillator capable of delivering about 1.5 kw. at 3 mc. The voltage was stepped up in an air-cored transformer before being applied to the external electrodes. The radio-frequency current was measured with a thermocouple meter. Operating current was from 250 ma. to 350 ma. and the applied voltage was from 3000 to 4000 v.r.m.s.

The  $H_{\alpha}$  light output of the discharge tube was monitored with a red filter and a photonic cell. The pressure in the vacuum system ranging from 0.1 to 0.4 mm. of mercury was read on a thermocouple gauge. The hydrogen was produced by electrolysis and dried over phosphorus pentoxide before admission to the discharge tube.

With the system described above, the discharge in the tube extended uniformly throughout the section between the electrodes for guide sections up to one meter in length.

### Methods of Measurement

Two distinct methods were used to measure the attenuation in the plasma within the discharge tube, the standing wave method and the comparison method.

*Standing Wave Method*

This method is based upon a measurement of the standing waves produced by a short circuit placed at the end of the wave guide beyond the section whose attenuation is to be measured (5, 10). As the plunger is shifted the standing wave ratio will pass through maximum and minimum values. If they are denoted by  $r_{Max}$  and  $r_{Min}$  respectively then the attenuation is given by the formula

$$A = 10 \log_{10} \left( \frac{\sqrt{r_{Max} r_{Min}} + 1}{\sqrt{r_{Max} r_{Min}} - 1} \right) \text{ db.}$$

This method is accurate only for fairly small mismatches at the input to the attenuating section owing to the experimental difficulties in detecting small changes in large standing wave ratios. The voltage standing wave ratio  $r'$  due to the mismatch at the input is given by

$$r' = \sqrt{\frac{r_{Max}}{r_{Min}}}.$$

This formula is used to check that the match remains within certain limits.

The attenuation was first measured with the discharge off. This was done for a number of frequencies in each range. Then the measurements were repeated with the discharge tube operating. The net attenuation due to the plasma in the discharge could then be found.

*Comparison Method*

Attenuation was measured by comparing the power entering the attenuating section with the power leaving the attenuating section. This method required that the whole system be very well matched at all points.

*Anomalous Dispersion Method*

An attempt was made to see if the anomalous dispersion could be detected at the frequency where absorption was predicted. In the vicinity of an absorption frequency one might expect changes in the dielectric constant. The value of  $\lambda_g$  depends on the dielectric constant and the positions of the maxima and minima in the standing wave pattern depend on the value of  $\lambda_g$ . The effect of an anomalous dispersion on  $\lambda_g$  might be detected by plotting the positions of standing wave minima or maxima against frequency. It would show up as an irregularity on an otherwise smooth curve. With the apparatus arranged as for the standing wave method of attenuation measurement, the plunger was left fixed in position and the frequency changed. The positions of the maxima were found for each of a series of frequencies, with the discharge tube operating.

**Results***Standing Wave Method*

The curves of attenuation for the frequency ranges 9550 mc. to 10,200 mc. and 10,750 mc. to 11,100 mc. are shown in Figs. 7 and 8. Readings which were

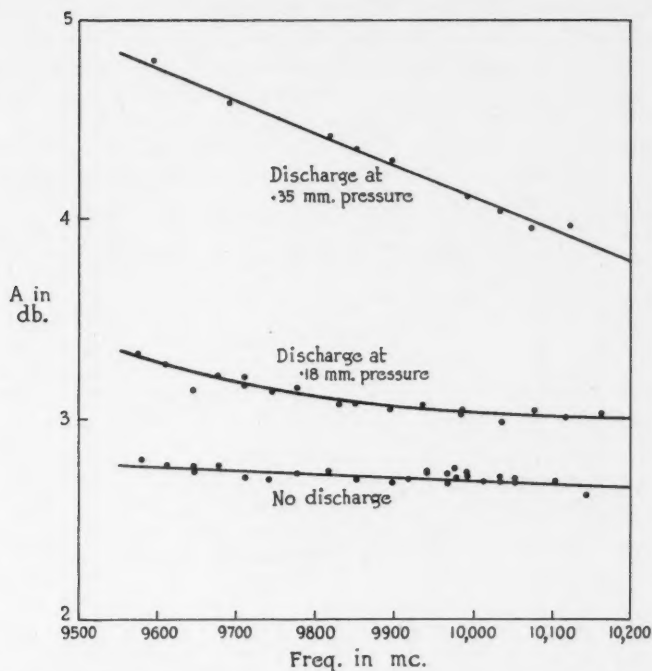


FIG. 7. Attenuation measurements for the frequency range 9950 mc. to 10,200 mc. with and without the discharge.

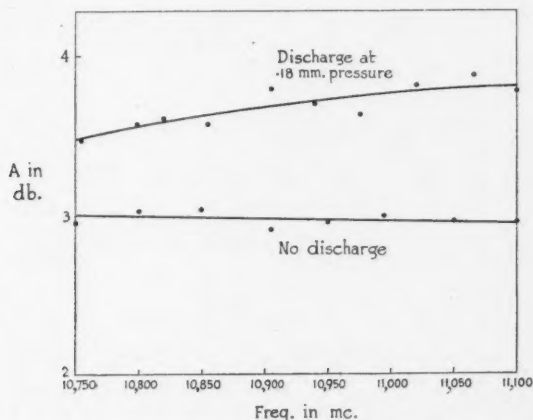


FIG. 8. Attenuation measurements for the frequency range 10,750 mc. to 11,100 mc. with and without the discharge.



repeated agreed generally to within 0.02 db. The net attenuation due to the plasma found from these is shown in Figs. 9 and 10. The deviations of the points from the experimental curves were used to calculate the probable error. This is indicated by the dotted lines. From these curves it can be concluded that for the frequency range 9550 mc. to 10,200 mc. there is no selective absorption greater than 0.06 db. or 1% which is twice the probable error. For the frequency range 10,200 mc. to 11,100 mc. there is no selective absorption greater than 0.14 db. or 3.3%.

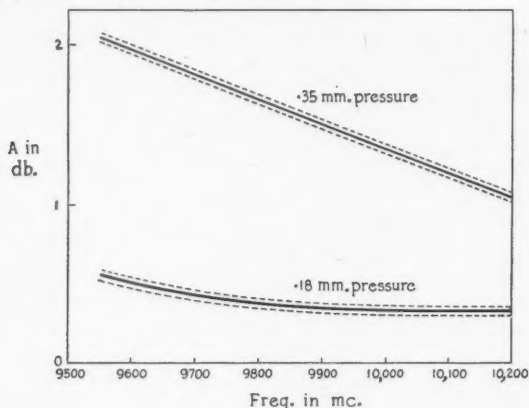


FIG. 9. Attenuation in the plasma for the frequency range 9550 mc. to 10,200 mc. by the standing wave method.

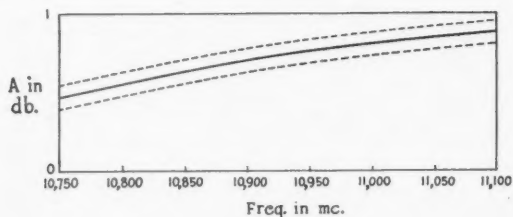


FIG. 10. Attenuation in the plasma for the frequency range 10,750 mc. to 11,100 mc. by the standing wave method.

#### Comparison Method

The attenuation measured by the comparison method for the lower frequency range is shown in Fig. 11 in which the dotted lines show the results of the standing wave method in the same range. The agreement between the two methods is good and the accuracy is about the same but the standing wave method is very much easier to apply since exact matching is not necessary.



An approximate calculation was made of the amount of background absorption that would arise from the free electrons in the discharge. This was based upon  $N$ , an estimate of the number of free electrons per cubic centimeter obtained from a value of dielectric constant taken from the measurements of

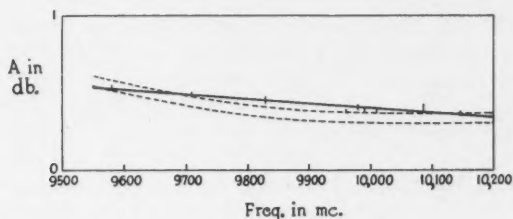


FIG. 11. Attenuation in the plasma for the frequency range 9950 mc. to 10,200 mc. by the comparison method. The limits for the attenuation by the standing wave method are shown by the dotted lines.

$\lambda_0$  used in the search for anomalous dispersion. A value for  $Z$ , the number of collisions made by an electron in one second, was obtained from reported measurements on hydrogen discharge tubes (1, 6). The absorption coefficient per centimeter (12) is then given by

$$\mu = 6.0 \times 10^{-24} \lambda^2 Z N,$$

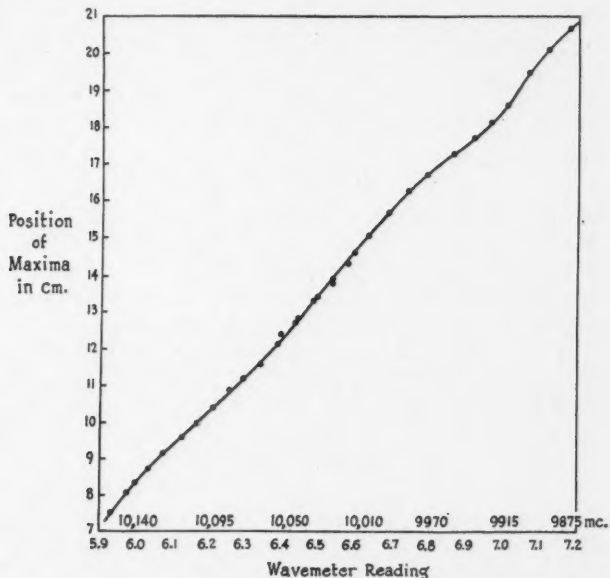


FIG. 12. Curve taken to investigate anomalous dispersion.

where  $\lambda$  is the wave length of the incident energy. This calculation showed that the background attenuation obtained may reasonably be accounted for by the absorption due to free electrons.

#### *Anomalous Dispersion Method*

The curve showing position of maxima in the standing wave pattern plotted against frequency is shown in Fig. 12. It did not reveal any irregularities that could be attributed to anomalous dispersion. Small periodic departures from the smooth curve are attributed to residual mismatch. The position of these could be changed by moving the plunger. A calculation of the deviation from the smooth curve to be expected from quantum mechanical dispersion theory indicates that there is only a very slightly better chance of observing the transition by this method than by attenuation measurement.

#### **Conclusion**

The estimate of the success of the experiment involved the population of hydrogen atoms in the  $2s\ ^2S_{1/2}$  state. The approximate value of the population as reported by Carst and Ladenburg (4) now appears to have been too large,

#### **Acknowledgments**

The writer wishes to thank Prof. J. M. Anderson and Prof. R. W. McKay for their constant help and encouragement. This investigation was made possible through two fellowships granted by the National Research Council. Grants for the purchase of apparatus were made by the Defence Research Board and the University Advisory Committee of Scientific Research. Some of the rectangular copper wave guide was contributed by Anaconda American Brass Ltd.

#### **References**

1. BANERGI, D. and GANGULI, R. Phil. Mag. Seventh Series: 494. 1932.
2. BETHE, H. A., BROWN, L. M., and STEHN, J. R. Phys. Rev. 77: 370. 1950.
3. BETZ, O. Ann. Phys. 15: 321. 1932.
4. CARST, A. and LADENBURG, R. Z. Phys. 48: 192. 1928.
5. EBERT, J. NDRC 14-439; PIB-43 April 5, 1945.
6. HAASE, TH. Ann. Phys. 23: 657. 1935.
7. KLUMB, H. Physik. Z. 32: 445. 1932.
8. LAMB, W. E. JR. and RETHERFORD, R. C. Phys. Rev. 72: 241. 1947.
9. LAMB, W. E. JR. and RETHERFORD, R. C. Phys. Rev. 79: 549. 1950.
10. MONTGOMERY, C. G. Techniques of microwave measurements. Vol. 11. M.I.T. Radiation Lab. Series. McGraw-Hill Book Company, Inc., New York. 1947.
11. RETHERFORD, R. C. and LAMB, W. E. JR. Phys. Rev. 75: 1325. 1949.
12. STEWART, J. Q. Phys. Rev. 22: 324. 1923.

## METEOROLOGICAL EFFECTS ON COSMIC RAY INTENSITY AND THE MESON SPECTRUM<sup>1</sup>

BY D. C. ROSE

### Abstract \*

Continuous recording of the intensity of the hard component of cosmic rays has been carried out at Ottawa (Geomagnetic Lat. 56.8) and at Resolute (Geomagnetic Lat. 83) in the Canadian Arctic for over a year. Two counter telescopes with different amounts of lead shielding are used at each station. The results have been analyzed for barometer effect in four series of observations each extending over three months. When averaged, they show a barometer coefficient of  $-1.75\%$  per cm. of mercury for mesons with momenta above 350 Mev./c and  $-2.13\%$  per cm. of mercury for those with momenta above 630 Mev./c.

A calculation has been made of the temperature and barometer effects. It was based on the variations in the probability of decay of mesons in the atmosphere, under varying atmospheric conditions. The calculations of the temperature effect do not yield results comparable with measurement; those of the barometer effect show that considerable information can be obtained about the meson spectrum from measurements of the barometer coefficients. The results favor a spectrum in agreement with parts of spectra measured by other authors. They suggest the possibility of a second maximum in the production spectrum of mesons.

### I. Introduction

The "barometer effect" and "temperature effect" on the intensity of cosmic rays at sea level have played an important role for many years (13) in studies of the nature of cosmic rays. The temperature effect in particular was shown by Blackett (2) to give proof of the radioactive decay of the meson. For some time both effects have been considered to be consistent with current knowledge of the production of mesons in the atmosphere and their decay and absorption as they proceed to sea level. A more quantitative explanation, however, based on this knowledge and actual atmospheric conditions seemed worth attempting.

A new calculation therefore has been made and measurements have been taken which were designed so that their results could be applied to the calculation. The calculation is based on the effect of changing atmospheric conditions on the probability of decay of mesons as they pass through the atmosphere. An actual mean atmosphere was used and alternative sea level spectral distributions were chosen to compare with measurements. This approach differs considerably from that of Janossy (8) who assumed an isothermal atmosphere and chose a simple mathematical expression to represent the spectrum, or from that of earlier analyses (for instance Rossi (16)) wherein the effects of absorption in the atmosphere and radioactive decay were treated separately.

### II. Experimental

#### A. Description of Apparatus

Continuous recordings of cosmic ray intensities have been taken at two stations, Ottawa (Geomagnetic Lat. 56.8°N) and Resolute (Lat. 74°41'N).

<sup>1</sup> Manuscript received September 8, 1950.

Contribution from the Division of Physics, National Research Laboratories, Ottawa, Canada. Issued as N.R.C. No. 2333.

Long.  $94^{\circ}55'W$ . Geomagnetic Lat.  $83^{\circ}N$ ) in the Canadian Arctic. Both stations are near enough sea level (about 170 and 55 ft. respectively) that no consideration need be given to differences in altitude. The Ottawa station has been recording almost continuously since October 1948 and the Resolute station since September 1949. Counter telescopes are used and, since September 1949, the equipment at the two stations has been identical. It consists of three counter trays arranged to form two vertical telescopes of two counter trays each, one tray being common to both telescopes. The trays each contain two counters 1 in. in diameter and about 16 in. active length. The trays are mounted one above another with 6 in. of lead in horizontal sheets between the top and center tray (Nos. 1 and 2) and  $8\frac{1}{2}$  in. between Nos. 2 and 3. Double coincidences were recorded between trays 1 and 2 and between 1 and 3. There are therefore two telescopes, one with 6 in. of lead, the other with  $14\frac{1}{2}$  inches of lead (plus a negligible amount of aluminum and brass) between trays. This arrangement was chosen to give a maximum amount of information with a minimum amount of equipment, as the space and power available at Resolute were very limited.

The bottom tray was placed at floor level near the ground with 1 in. of lead under it and 4 in. on each side. This shields it effectively against soft component. The center tray and top tray were not shielded on the sides, and the covering over the top tray and whole apparatus including the roof of the building was equivalent to 6 or 8 gm. per  $cm.^2$  of wood, which was neglected in comparison to the lead shielding between counters.

Previous to September 1, 1949, the arrangement of counters at Ottawa was somewhat different from that described above. For the first series (October 1948 to January 1949) two separate telescopes were used. Each had 4 in. of lead between counters and  $\frac{1}{2}$  in. above the top tray. There was at least 2 in. of lead on the sides and the whole was placed inside an old rifle range with concrete walls and ceiling 1 ft. thick. The second series (February to June 1949) was similar to the first except one telescope had 5 in. of lead between counters and the other had 13 in.

The results described here therefore come from four series of measurements as follows:

Series 1—Ottawa, October 1948 to January 1949 inclusive; shielding  $4\frac{1}{2}$  in. of lead and 1 ft. of concrete; heavy shielding on sides.

Series 2A—Ottawa, February to June 1949 inclusive; shielding  $5\frac{1}{2}$  in. of lead and 1 ft. of concrete; heavy shielding on sides.

Series 2B—Same as 2A but with  $13\frac{1}{2}$  in. of lead plus concrete.

Series 3A—Ottawa, September to December 1949 inclusive; 6 in. of lead between counters and a light roof.

Series 3B—Same as 3A but with  $14\frac{1}{2}$  in. of lead between counters; bottom counter shielded on sides.

Series 4A—Resolute, same period and arrangement as 3A.

Series 4B—Resolute, same period and arrangement as 3B.

The minimum momentum accepted by the shielding was estimated from the curves published by Montgomery (14).

Telescopes with only two counter trays and no side shielding do not give high discrimination against side showers. This is important because of the known high barometer effect for showers. However, calculations and tests showed that in the experimental arrangement used here the number of coincidences due to side showers was less than 3% and the error due to these, even though it is systematic, would not affect the conclusions. Therefore, no corrections were made for side showers.

The method of recording was developed especially for long periods of continuous operation and is very accurate. Multiple binary scalers were used and each time a scaler repeated its cycle it was marked on a multiple pen recorder on which time marks were included. The details of the circuits and methods of recording will be published separately.

#### *B. Methods of Analysis*

As the same records were used to study anomalies in intensity due to such phenomena as solar flares (15) the records were averaged over short intervals, usually four hours. To save computation and make best use of statistical accuracy of counting rates some selection was made in the data to be used.

For analyses with barometric records, periods of eight hours or more were chosen during which the barometric pressure was reasonably steady, that is, did not change by more than about 3 millibars during the period. This represented less than half the total time. The mean cosmic ray intensity during these periods was compared with the pressure by standard statistical methods. The selection of data from periods of steady pressure seems justified because points taken during rise or fall of the barometer will give values near the mean where there are a large number of points in any case. The selected data are distributed more uniformly over the range of pressure, and the amount of computation is greatly reduced. Occasionally shorter periods (less than eight hours) were included in order to take advantage of very low pressures which do not as a rule last for long periods, and in one series of measurements where 24 hr. averages had been worked out these were used directly, again selecting those where the barometer was reasonably steady during the period.

In the correlation with barometric pressure no temperature corrections were made. Forbush (7) has shown that a correction for ground temperature does not increase the reliability of the data. The objective of this measurement was to get a barometer coefficient that could be compared with the theoretical calculations of Section III. To do this the measured barometer coefficients should be independent of temperature. Though temperature changes throughout the atmosphere obviously affect the cosmic ray intensity at sea level, a straight correlation with pressure should give the true barometer coefficient if the relation between temperature and pressure is of a random nature.

There is a well known inverse correlation between pressure at any specific height above sea level and the mean temperature between that height and sea level. However, in the analyses in the next section the behavior of mesons is studied in an actual atmosphere specified in terms of pressure and density rather than in terms of height. A rough test was made to look for a correlation between ground pressure and temperature at any pressure level in the atmosphere. Data were obtained from the radiosonde meteorological station at Sault Ste. Marie, which is the nearest radiosonde station to Ottawa with similar weather. Using the periods of steady pressure selected for the cosmic ray measurements in Series I the excursions from the mean seasonal temperature at various pressure levels up to 200 mb. were plotted against ground pressure. The resulting plot showed by inspection such a random scattering of points that the correlation seemed negligible. The barometer coefficient obtained by straight correlation with ground pressure therefore is probably the best to compare with the calculation in Section III even though some seasonal temperature effects may not have been eliminated.

The analysis used here was planned for comparison with the calculations in Section III and not particularly for the correction of cosmic ray data. Therein it differs from that of Duperier (6) who finds a very good correlation between the intensity of the hard component at sea level and a combination of three variables, the barometric pressure at ground level, the height of the effective meson production layer (the 100 mb. layer), and the mean temperature at levels between 100 and 200 mb. in the atmosphere. Duperier's analysis would give a more precise way to correct cosmic ray data where information on the upper atmosphere is available.

### C. Results

The measured barometer coefficients are shown in Fig. 1 and listed in Table I with corresponding correlation coefficients. The shielding was such that the points are distributed about two groups, one of average momentum 351 Mev./c,

TABLE I

Series	Barometer coefficient %/cm. Hg	Correlation coefficient	Momentum limit, Mev./c.
3A	-1.23	-.44	305
4A	-2.07	-.66	305
1	-2.04	-.69	374
2A	-1.67	-.44	420
Mean	-1.75		351
3B	-1.88	-.62	604
4B	-2.35	-.53	604
2B	-2.17	-.43	682
Mean	-2.13		630

and the other 630 Mev./c. The means are shown at these two points in Fig. 1. The distribution of the points about the means gives an indication of the accuracy. This is not high, but the results suggest clearly that the magnitude of the barometer coefficient is increasing with momentum over the range measured. This feature is consistent in each series of observations where two thicknesses of absorber were used simultaneously, and will be seen in Section III to have an important bearing on the shape of the meson spectrum at low energies.

This upward slope toward low momenta is not entirely in agreement with other observers where different thicknesses of absorber were used. Most measurements recorded with two thicknesses of absorber were taken with ionization chambers. Though measurements of the barometer effect taken with ionization chambers and with counters should vary the same way with momentum, they are not quantitatively comparable. The counter telescope pointing vertically includes only a limited cone of particles and counts each one with equal emphasis. Ionization chambers have no directional selection and over-emphasize the particles that just penetrate the width of the chamber. Some values obtained with ionization chambers are:

Forbush (7)	-2.36 to -3.33%/cm. Hg	12 cm. lead
Compton and Turner (5)	-1.6%/cm. Hg	12 cm. lead
Messerschmidt (10)	-1.84%/cm. Hg	10 cm. lead
	-1.04%/cm. Hg	20 cm. lead

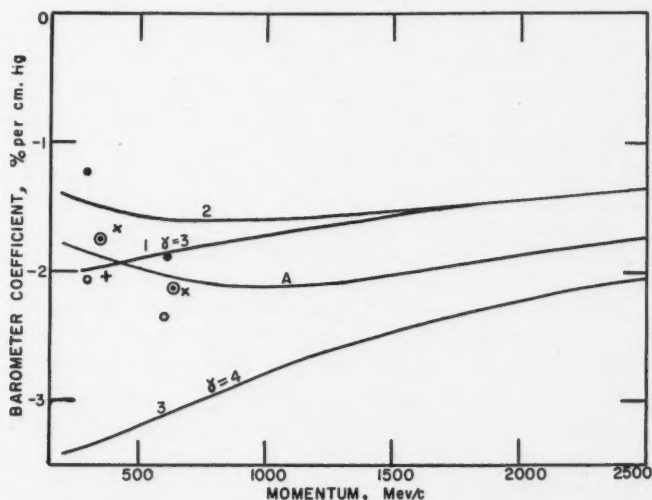


FIG. 1. The integral barometer coefficients. The points represent measured values and the curves computed values. Points in each series of measurements are marked alike.  $\odot$  represents the means of groups of points. Curve 1 corresponds to a spectrum for which  $\gamma = 3$ , Curve 2 to the Wilson spectrum, Curve 3 to a spectrum for which  $\gamma = 4$ , and Curve A was selected to fit the measured points.



Values with counter telescopes are:

Duperier (6)	-2.2%/cm. Hg	25 cm. lead
Barnothy and Forro (1)	-3.1%/cm. Hg	36 cm. lead
Kolhorster (9)	-1.5%/cm. Hg	140 gm./cm. <sup>2</sup> wood
Smith and Gast (12)	-3.4%/cm. Hg	20.5 cm. lead
(reported by	-1.5%/cm. Hg	30. 5 cm. lead
Millican and Loughridge)		

Duperier has pointed out the great variation of results obtained when a simple correlation is made between intensity and pressure; this was also noted here as the analysis of the results of Series 4A was made in monthly periods as well as for the whole period of four months. The monthly values of the barometer coefficients are -2.52, -1.68, -3.09, and -1.29 and of the correlation coefficient -.66, -.91, -.51 and -.85 respectively. If a simple correlation of this type is to be of value it obviously must be carried out over a long period.

It is not certain whether any significance should be attached to differences between measurements at Ottawa and Resolute. While the mean climate is very different from the point of view of comfort, it will not have much effect on the probability of meson decay in the atmosphere. The sea level intensity is essentially the same at Ottawa and Resolute, as both are above the "knee" in the latitude effect. Significant differences in barometer coefficients at lower latitudes might be expected.

### III. Theoretical Calculations

#### A. General Considerations

Barometer and temperature coefficients may be calculated from a knowledge of the sea level spectrum and the behavior of mesons in their passage through the atmosphere. Rossi (17) has given reasons for assuming that the flux of ionizing particles in the hard component (under 10 cm. of lead shielding) at sea level consists almost entirely of mesons. The small fraction of heavier particles and few electrons that may come from showers in the lead can be neglected. This has been accepted in the following calculations even though a small fraction of penetrating particles with large meteorological effects (such as are found for penetrating showers) would affect the results. The process of the formation of mesons (the decay of a  $\pi$  meson to a  $\mu$  meson) is also not considered relevant in view of the very short life time of the  $\pi$  meson.

It is assumed that mesons reaching sea level with a momentum  $P_G$  have come on the average from a pressure level  $p_m$  in the atmosphere, the level being measured by its pressure in grams per square centimeter. The probability of their decay between production level and sea level can be calculated from the well known radioactive decay equation, in the form

$$\frac{dN}{Ndl} = -\frac{\mu}{\tau P},$$



where  $N$  represents the number of particles at any point with momentum  $P$ ,  $\mu$  is the mass and  $\tau$  the mean life at rest, and  $dl$  is an element of length of path of the meson. For mesons moving vertically downwards  $dl$  may be written  $dp/\rho$ , where  $\rho$  is the density of the atmosphere. If one assumes that the momentum loss per unit mass of air traversed is constant over any range of momenta from production level to sea level (momenta below minimum ionization are excluded with the soft component)  $P$  may be written  $P_G + \alpha(p_G - p)$ , where  $P_G$  is the momentum at sea level and  $\alpha$  is the momentum loss per gram per square centimeter. The ratio of intensity at sea level to that at production level is

$$\frac{N_G}{N_m} = e^{\frac{-\mu}{\tau c} \int_{p_m}^{p_G} \frac{dp}{\rho \{P_G + \alpha(p_G - p)\}}}$$

The  $c$  in the denominator of the exponent will normalize all units so that mass is measured in units of  $\text{Mev.}/c^2$ , momentum in  $\text{Mev.}/c$ , pressure in grams per square centimeter, density in grams per cubic centimeter, and  $\tau$  in seconds. The path of the particle is assumed to be rectilinear, or so nearly rectilinear that scattering has a negligible effect on its range. The occasional collision where the energy loss is very large is also neglected.

A change in atmospheric conditions will result in a change in the original momentum of a meson which reaches sea level with a momentum  $P_G$ . A production spectrum of the inverse power law form is assumed and the intensity at sea level can then be represented by the equation

$$N_G = \frac{k}{E^\gamma} e^{\frac{-\mu}{\tau c} \int_{p_m}^{p_G} \frac{dp}{\rho \{P_G + \alpha(p_G - p)\}}}, \quad (1)$$

where  $k$  is a normalizing constant and  $E$  is the energy at production. This equation cannot be integrated directly unless some simple relation between pressure and density exists. It also shows the difficulty in calculating a separate barometer and temperature coefficient. This was done however by selecting a standard atmosphere, then a second atmosphere differing from the first in temperature only, and a third differing from the first in pressure only.

The standard atmosphere chosen was the mean (from radiosonde measurements at Sault Ste. Marie, Michigan) of the atmospheric conditions during periods of steady barometer selected in Series 1 for the analysis of cosmic ray results. The temperature-altered atmosphere was calculated from the standard atmosphere by varying the temperature by an amount  $\Delta T$  ( $10^\circ\text{C.}$  was chosen for  $\Delta T$ ) at each pressure level in the atmosphere. This is not a real atmosphere, as temperature changes never extend uniformly all the way up through the atmosphere.

The pressure-altered atmosphere was calculated by changing the pressure an amount  $\Delta p_G$  at sea level and a proportional amount  $\Delta p_G p / p_G$  at other levels. The density was adjusted so that the temperature at any height above sea level remained constant. This also may not represent a pressure change as found in

practice but if temperature changes throughout the atmosphere vary in a random way with the total weight of atmosphere this pressure-altered atmosphere compared with the standard should give a barometer coefficient comparable with the measurements described in Section II.

### B. The Temperature Coefficient

Equation (1) was integrated numerically for the three atmospheres, each with a series of values for  $P_G$ . The temperature coefficient is defined as  $\Delta I/I\Delta T$  and usually quoted in per cent per degree Celsius. If the value of the exponential part of the equation after integration is represented by  $S$  for the standard atmosphere and  $\theta$  for the temperature-altered atmosphere, the temperature coefficient may be written

$$\frac{\Delta I}{I\Delta T} = \frac{S - \left(\frac{E_S}{E_\theta}\right)^\gamma \theta}{S\Delta T}, \quad (2)$$

$E_S$  and  $E_\theta$  refer to the energies of production of mesons which reach sea level with momentum  $P_G$ . As the total mass of air through which the mesons pass will be the same for both the standard atmosphere and temperature-altered atmosphere  $E_S = E_\theta$ . Therefore, the "differential" temperature coefficient is independent of the production spectrum. Actual measuring apparatus usually accepts particles with all momenta above the minimum fixed by the shielding. Therefore, it is an "integral" coefficient that is required. This was obtained by a further numerical integration based on the calculated differential coefficients and the sea level spectrum. For the temperature effect the sea level spectrum of Wilson as presented by Rossi (17) was chosen. Fig. 2 shows the differential temperature coefficient as calculated from Equation (2) and the integral curve. The coefficients are negative, as would be expected. As mentioned above, the temperature-altered atmosphere does not represent actual conditions. Apart from repeating all the numerical integrations for every change in atmospheric conditions there is no way to compare calculations with measurements of temperature effects. Duprier (6) has shown a partial correlation between sea level

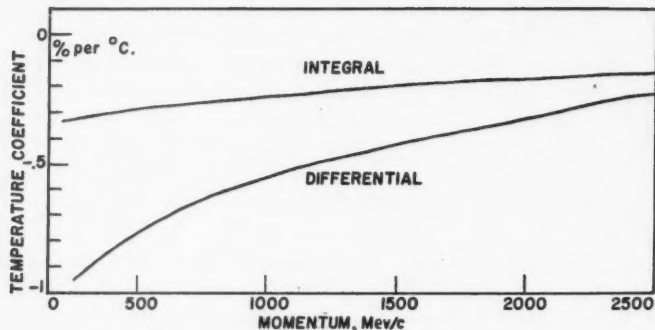


FIG. 2. The differential and integral temperature coefficients based on a uniform change in temperature throughout the atmosphere.

intensity and temperature at levels between 100 and 200 mb. in the atmosphere. A calculation could have been made for a temperature change at that level only, but it would give a small negative coefficient rather than the positive value found by Duperier.

### C. The Barometer Coefficient

If the exponential part of Equation (1) is again represented by  $S$  for the standard atmosphere and by  $R$  for the pressure-altered atmosphere, the barometer coefficient may be represented by the equation

$$\frac{\Delta I}{I \Delta p_G} = \frac{S - \left(\frac{E_S}{E_R}\right)^\gamma R}{S \Delta p_G} \quad (3)$$

In this case  $E_S$  is not equal to  $E_R$ . Therefore, the spectral term is important.

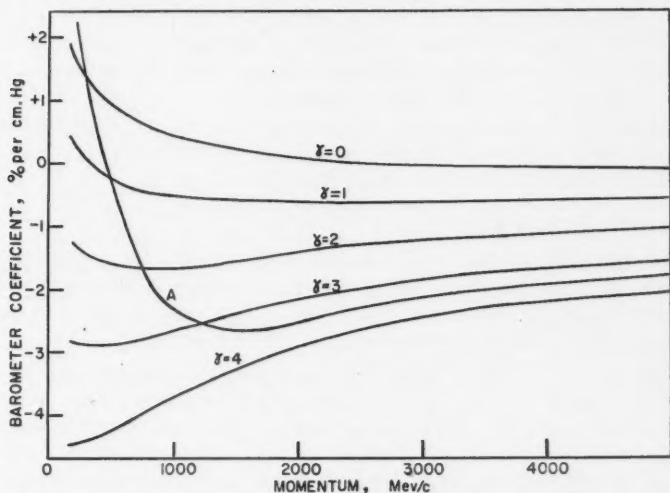


FIG. 3. The calculated differential barometer coefficients for different values of  $\gamma$ . Curve A represents a spectrum selected to fit the measured points in Fig. 1.

Fig. 3 shows the calculated differential barometer coefficients for  $\gamma = 0, 1, 2, 3, 4$ , and for a spectrum (marked A) which gives a good fit with the measured coefficients. As mentioned in the case of the temperature coefficient an integral coefficient is required for comparison with measurements. The integral barometer coefficients were calculated by further numerical integrations over selected sea level spectra using the differential coefficients calculated from Equation (3). The results are shown by the curves in Fig. 1.\* For Curve 1, the

\* The units used for pressure in the calculation of barometer coefficients were grams per square centimeter. The coefficients are usually quoted in % per centimeter of mercury. Therefore, this unit has been used in displaying results. Similarly pressure levels in the atmosphere are usually measured in millibars. Hence that unit is used in referring to production levels of mesons.

chosen sea level spectrum is that obtained when  $\gamma = 3$ . The calculations for Curve 2 were based on the sea level spectrum measured by Wilson (as published by Rossi (17)). Curve A is calculated from a spectrum chosen to give a good fit with the measured points and corresponds to Curve A in Fig. 3. For Curve 3,  $\gamma = 4$ .  $\gamma$  of course applies to the production energy spectrum while the final integration required to calculate the curves in Fig. 1 is based on the sea level momentum spectrum. The data from the integration of Equation (1) can be used to derive one spectrum from the other.

#### IV. Discussion

##### A. General Remarks

Interesting features in the results of these calculations are the values of the differential barometer coefficient for  $\gamma = 0$ , and the way in which this coefficient varies with  $\gamma$ . If the production spectrum showed the same intensity at all energies the value of the differential barometer coefficient would be positive at low momenta instead of negative. This can be explained by the fact that, for low values of  $P_G$ , the change in mean momentum which results from a change in barometric pressure overshadows the change in the height of the effective layer of formation. The sensitivity of the integral barometer coefficient to the slope of the production spectrum as represented by the value of  $\gamma$  is shown by the difference between Curves 1 and 3 of Fig. 1.

##### B. Accuracy of Calculations

The values used for the mass and mean life at rest for the meson were 215 times the electron mass and  $2.10 \times 10^{-6}$  sec. respectively. As the calculated barometer coefficients represent differences in two integrations of Equation (1), possible errors in these would make little difference in the results.

When the calculations were started it was assumed that it would be sufficiently accurate to treat  $\alpha$  as a constant having a value slightly above that for minimum ionization. A rough mean between 500 and 1000 Mev./c was chosen, making  $\alpha = 1.95$  Mev./c per gm. per cm.<sup>2</sup> Early results showed however that the part of the meson spectrum between 2000 and 10000 Mev./c. played a dominant part in fixing the general level of the integral barometer coefficient curve. The above value of  $\alpha$  was too low for that region. Therefore, a correction was made by recalculating some points using values of  $\alpha$  in line with published data for the mean momentum for the value of  $P_G$  concerned.

The value of  $p_m$ , the mean level of production, was also assumed at first to be constant and fixed at 100 mb. In calculating the production spectrum from the sea level spectrum, Sands (18) has pointed out that the mean level of production must vary with momentum, particularly at the low end of the spectrum. He assumed a production law in the atmosphere of the form  $\exp(-x/100)$  in grams per square centimeter and calculated the effective level of production for mesons of different range. This method was not used here, but the differential barometer coefficients were calculated for assumed production levels of 200 and 300 mb., as well as 100 mb., to establish the effect of varying heights

on the results. Finally a production height function was adopted wherein mesons with a sea level momentum of 200 Mev./c (the lowest considered in these calculations) were assumed to come from a mean level of 150 mb. The height of production was assumed to slope upwards to 100 mb. for mesons with a sea level momentum of 1000 Mev./c and to remain constant for those of higher momentum. This height function represents slightly higher levels than that used by Sands but the calculations show that, though the height function has considerable influence on the exact shape of the derived production spectrum, the differences would not affect the general conclusions that can be drawn from the measurements described here.

The derivation of Equation (1) is such that it applies only to mesons moving vertically downwards. The counter telescopes as used included quite a wide solid angle (in the case of the shortest as much as  $10^\circ$  by  $50^\circ$  half angles). The effect of this can be shown to be small by a rederivation of Equation (1) for mesons whose path makes an angle  $\phi$  with the vertical. To a first approximation the term  $\rho\{P_G + a(p_G - p)\}$  becomes

$$\rho \cos \phi \left\{ \frac{P_G}{\cos \phi} + \frac{a(p_G - p)}{\cos \phi} \right\}$$

and therefore does not change. The ratio  $E_S/E_R$  changes very little. The largest error occurs in replacing  $P_G$  by  $P_G/\cos \phi$ . This infers a linear relation between the range in lead, and momentum right down to low momenta. It also applies only to arrangements wherein the shielding is in horizontal sheets, which was the case in the measurements described here. With cylindrical or spherical symmetry in shielding, the directional effects would be more pronounced. They cannot however be very great because in the case of Series 4 an analysis was made of the recordings of counting rates from the bottom counter telescope which had  $14\frac{1}{2}$  in. of lead on top in a pile 3 in. wide but only enough on the sides to remove the soft component. The mean value of the barometer coefficient was  $-2.0\%$  per centimeter of mercury. A rough calculation at one value of  $P_G$  shows that, with the counter telescopes as used, the error due to solid angle would be in a direction that would tend to modify the conclusion (see Section V) about a second maximum in the production spectrum of mesons but is not great enough to allow its withdrawal. An exact computation including directional effects would involve further integrations and assumptions about differential spectrum at different angles.

The numerical integrations were carried out using trapezoids of a maximum width to give reasonable accuracy without excessive computation, and a certain amount of interpolation was used. Errors due to the methods used however could hardly represent more than about  $0.1\%$  per centimeter of mercury in the position of the curves in Fig. 1 and would not affect the conclusions.

### C. The Meson Spectrum

Comparing the points in Fig. 1 with Curve 1, for which  $\gamma = 3$ , it is seen that this curve passes about midway between the means of the two groups of measured points. The points, however, indicate a downward or negative slope

with increasing momentum, while Curve 1 slopes upward. The accuracy is such that the significance of this downward slope is questionable but the conclusions that result from accepting it are interesting and have some support in other experiments.

A simple power law spectrum will not give an integral barometer coefficient curve with this negative slope at low momenta. Rossi in 1948 reviewed measurements of the sea level meson spectrum and showed both a differential momentum and range spectrum (Figs. 4 and 6 of ref. (17)). He gave reasons which indicate that the measured points at low momenta underestimate the intensity and showed a solid curve representing the most likely sea level spectrum. Translating this to a production spectrum using the present calculations, a spectrum is obtained which gives an almost constant value of  $\gamma$ , a little less than 3 at low momenta and rising to about 3 at the higher momenta values. This is in agreement with similar calculations made by Sands (18) who gives an average value of  $\gamma = 2.5$  for the corresponding part of his spectrum.\*

As the measured points suggested a slope that is not in agreement with a simple power law production other spectra were tried. Curve 2 in Fig. 1 is based on a smooth curve drawn through Wilson's measured points as shown by Rossi (Fig. 4 of ref. (17)). This gives the desired slope at low momenta but in general level it is well above the measured points. Curve A was based on a spectrum which, at momenta below 3000 Mev./c (at production levels), is identical to that derived from Wilson's measurements. However above 3000 Mev./c it has a slope corresponding to  $\gamma = 3.5$ . This curve gives a reasonably good fit with the measured points, and the increased slope at high momenta is in agreement with a recent measurement of the sea level spectrum by Caro, Parry, and Rathgeber (4). When transposed to production levels their curve would indicate a value of  $\gamma$  close to 3.5 above 3000 Mev./c, but at lower momenta it is more in accord with Rossi's sea level spectrum.

The production spectra corresponding to Curves 1, 2, and A are shown in Fig. 4. Spectrum A suggests a maximum in the intensity at about 2000 Mev./c. The intensity at much lower momenta must be much higher than the value at this point to account for the increase in total intensity with height in the atmosphere and to be consistent with measurements at high altitudes (3, 11). Therefore, the suggested maximum at 2000 Mev./c must be a second maximum in the production spectrum. The present results are not considered sufficiently significant to offer more than a suggestion of such a second maximum but there is some additional evidence in its favor. The measurements by Miller, Henderson, Potter, Todd, and Wotring (11) at an altitude of 3.4 km. show the expected maximum at low momenta, and in their curve for positive particles under 5 cm. of lead there is the suggestion of a second maximum slightly below 1000 Mev./c. These authors do not consider this maximum significant but a

\* Sea level measurements do not give any information about the very low momentum end of the meson production spectrum because, unless the mesons have enough energy to reach sea level from a height where an appreciable number are produced, the contribution to the sea level intensity is negligible. In the present calculations the lowest sea level momentum considered (200 Mev./c) represents a momentum of about 1900 Mev./c at a mean production level of 150 mb.



reduction of spectrum *A* to the expected spectrum at 3.4 km. shows a maximum very roughly in agreement with a curve through the observed points of Miller *et al.* The broken curve in Fig. 4 has therefore been drawn as a qualitative representation of a production spectrum that might be expected at momenta values below those included in spectrum *A*.

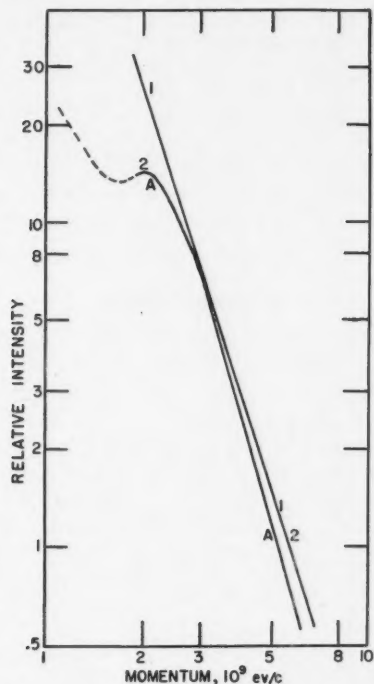


FIG. 4. The production momentum spectra of mesons. Curve 1 corresponds to a constant value of  $\gamma = 3$ , Curve 2 to the Wilson spectrum, and Curve A to the spectrum suggested by measurements of the barometer coefficient.

### V. Summary of Conclusions

The simple theory derived here gives a new physical explanation of the meteorological changes in the sea level intensity of the hard component of cosmic rays. This is based on current knowledge of the production of mesons in the atmosphere and their loss of energy and probability of decay in passing through the atmosphere.

Calculations on the "temperature" effect are necessarily based on hypothetical changes in the atmosphere and, therefore, do not give results that can be compared with measurements. They indicate, however, a general agreement with the expected behavior.

Calculations on the "barometer" effect have been made which can be compared with measurements. These show that the slope of the meson spectrum at production levels in the atmosphere has a dominant influence on the barometer coefficient. The measured results therefore indicate some features of the production spectrum that are in agreement with parts of spectra measured by other observers. At momenta below 1000 Mev./c there is good agreement with the measurements on the sea level spectra by Wilson, but at higher momenta the results show better agreement with the measurements of Caro, Parry, and Rathgeber.

Though the accuracy is not great the production spectrum which best fits the barometer coefficient measurements suggests that a maximum may exist at about 2000 Mev./c, which must be a second maximum in the total production spectrum. (The first is at much lower momenta.) This second maximum is also suggested in a recent measurement of the spectrum at 3.4 km. by Miller, Henderson, Potter, Todd, and Wotring.

### Acknowledgment

Meteorological data both for Ottawa and Resolute were supplied by the Meteorological Division of the Department of Transport of the Government of Canada. The station at Resolute is operated jointly by that Department and the United States Weather Bureau. The facilities supplied at Resolute are those of the Radio Division of the Department of Transport. The help of these departments is appreciated. The author also wishes to thank Mr. John Galt for operation of the equipment at Resolute, Miss E. Ford for assistance in analysis of records and in computing, Mr. R. Bailey, who collaborated in developing the methods used for continuous recording, and Dr. T. E. Morris for assistance and advice in regard to the theoretical aspects of the work.

### References

1. BARNOTHY, J. and FORRO, M. *Z. Physik*, 100: 742. 1936.
2. BLACKETT, P. M. S. *Phys. Rev.* 54: 973. 1938.
3. CAMERINI, U., FOWLER, P. H., LOCK, W. O., and MUIRHEAD, H. *Phil. Mag.* 41: 413. 1950.
4. CARO, D. E., PARRY, J. K., and RATHGEBER, H. D. *Nature*, 165: 688. 1950.
5. COMPTON, A. H. and TURNER, R. N. *Phys. Rev.* 52: 799. 1937.
6. DUPERIER, A. *Proc. Phys. Soc. (London)*, 62: 684. 1949.
7. FORBUSH, S. E. *Terr. Mag.* 42: 1. 1937.
8. JANOSSY, L. *Cosmic rays*. Oxford University Press, pp. 194, 195. 1948.
9. KOLHORSTER, W. and MATTHES, S. *Physik. Z.* 40: 142. 1939.
10. MESSERSCHMIDT, W. *Z. Physik*, 78: 668. 1932.
11. MILLER, C. E., HENDERSON, J. E., POTTER, D. S., TODD, J., and WOTRING, A. W. *Phys. Rev.* 79: 459. 1950.
12. MILLICAN, F. M. and LOUGHRIDGE, D. H. *Phys. Rev.* 74: 66. 1948.
13. MONTGOMERY, D. J. X. *Cosmic ray physics*. Princeton Univ. Press, Princeton, N. J. 1949. Survey of history of cosmic ray studies, p. 3.
14. MONTGOMERY, D. J. X. *Cosmic ray physics*. Princeton Univ. Press, Princeton, N.J. 1949. Appendix E, p. 349.
15. ROSE, D. C. *Phys. Rev.* 78: 181. 1950.
16. ROSSI, B. *Revs. Modern Phys.* 11: 296. 1939.
17. ROSSI, B. *Revs. Modern Phys.* 20: 537. 1948.
18. SANDS, M. *Phys. Rev.* 77: 180. 1950.



## PHOTOELECTRIC METEOR OBSERVATIONS<sup>1</sup>

BY BARBARA M. MCKINLEY AND D. W. R. MCKINLEY

### Abstract

The photoelectric meteor detector consists of 19 type 931-A photomultiplier tubes arranged to cover the entire sky. Signals from the photocells are repeatedly sampled in time sequence and displayed on a cathode ray tube. Photoelectric meteor signals, radar meteor echoes, and a marker light operated by visual observers are photographed by a continuous-film camera.

Preliminary tests indicated that the average sensitivity of the photoelectric detector to meteors was about one visual magnitude inferior to that of the human eye. Approximate meteor positions and qualitative light intensities could be obtained from the photoelectric record. Timing comparisons between the photoelectric and the radar records could be made to 0.05 sec. Methods of improving the sensitivity and other operational characteristics are discussed.

### Introduction

Since the summer of 1947 the National Research Council and the Dominion Observatory have been engaged in a joint program of meteor observing, employing radar and radio equipment, visual observers, and both direct and spectrographic cameras for meteor photography (1, 2, 3). More complete details of the projects are available in these earlier papers. During the observing periods the visual observers scan the sky and plot on maps the visual meteor paths, while at the same time a range-time record of meteor echoes is obtained from the radar system. When a visual observer sees a meteor he presses a button which flashes a marker light on the radar display. This marker on the radar film has a potential timing accuracy of 0.1 sec. but, owing to the reaction times of the observers, the mean relative timing accuracy is of the order of 1/2 to 1 sec., and the individual error can be considerably greater. Satisfactory correlation for most purposes is achieved by this technique to the extent that definite coincidences between the brighter meteors and the radar echoes can be well established, and can be further confirmed by comparing the visually plotted meteor positions with the positions obtained from three-station triangulation of the radar echo ranges (4).

However, there is evidence that the radar echo path length is shorter than the visual path in general, and that the radar path segment may tend to occur towards the latter portion of the plotted visual path. Before definite conclusions can be drawn it would be desirable to time the onset of the meteor luminosity relative to the radar echo with an accuracy of at least 0.1 sec. and preferably 0.01 sec. The use of photocells to detect the meteor light has been suggested. If the photocells were to prove satisfactory in this respect it was expected that they might be valuable in other phases of the work, for example, to determine the general luminosity curve of the meteor, in particular to time

<sup>1</sup> Manuscript received November 3, 1950.

Contribution from the Radio and Electrical Engineering Division, National Research Laboratories, Ottawa, Canada. Issued as N.R.C. No. 2340.

the appearance of bursts, or flares, and to give a rough plot of the meteor position and even of the meteor path in the sky.

The photocell system to be described here has been moderately successful in meeting the general specifications. During the trial periods of observation several modifications have been suggested for improving some features of the design, and these will be incorporated in future operations. However, as the project has been temporarily suspended, it was thought desirable to present an interim report outlining the progress to date.

### Apparatus

Each photocell unit consists of a 931-A photomultiplier tube with its associated battery power supply. Rectangular apertures have been cut in each photocell box to admit sky light over approximately  $30^\circ$  in azimuth and  $36^\circ$  in elevation. To cover the entire sky 19 of these photocell units were arranged on a circular table as shown in Fig. 1. The amplifiers and gating units can be seen in the cabinet supporting the photocell table.

The block diagram, Fig. 2, illustrates the general principles of the system. In essence, the information obtained by the photocell units is sampled in time sequence by the electronic circuits in such a manner that it can readily be correlated with the radar record. The initiating trigger pulse from the radar transmitter passes directly to the range sweep circuit. Identical linear sweeps, 260 km. long, are applied horizontally to two cathode ray tubes located side by side. The tubes are photographed by a camera in which 35 mm. film moves in a vertical plane continuously past the open lens at 4 in. per min. Seconds pulses appear on each sweep to facilitate the precise timing of the phenomena appearing on the two C.R.T.'s. Twenty-kilometer range markers are impressed on the sweeps as well, which serve the conventional purpose on the radar display, but on the photocell display they are used merely as gate markers to identify the outputs of the photocell units.

The trigger pulse from the radar transmitter is applied to amplifier unit No. 1 through an electronic delay of 40 km. ( $267 \mu$  sec.) because the range interval from 0 to 40 km. is reserved for the first row of seconds pulses. This delayed trigger then opens No. 1 electronic gate circuit for an interval of 10 km. ( $67 \mu$  sec.), allowing the light signal from No. 1 photocell unit to pass to the photocell display C.R.T. As soon as the gate in No. 1 unit has closed, a trigger pulse is sent to No. 2 unit to open the gate in this unit for 10 km., and so on to the 19th unit. In practice, an additional delay is inserted just prior to the 19th unit to avoid interfering with the second row of seconds pulses appearing between 220 and 240 km. on the range sweep. The gated outputs of all the photocell and amplifier units are then combined and applied as intensity-modulation to the photocell C.R.T. display. Thus, the output from a particular photocell will appear only in the interval on the range trace selected for it by the gating system. The signal from a given photocell is

sampled for  $67 \mu$  sec. every  $1/120$ th of a second (the transmitter pulse repetition frequency is approximately 120 c.p.s.) but successive sweeps overlap on the film so that the light intensity record appears continuous. The practical limit of time resolution is about 0.05 sec. with this recording technique.

Fig. 3 shows some selected records of the radar, visual, and photocell observations. The radar record is the upper one in each photograph, the black horizontal lines being the 20 km. range markers and the white dots the second



FIG. 1. The photoelectric meteor detector. Nineteen photocells, covering the entire sky, are arranged on the circular table. The cabinet contains the amplifier and gate units.



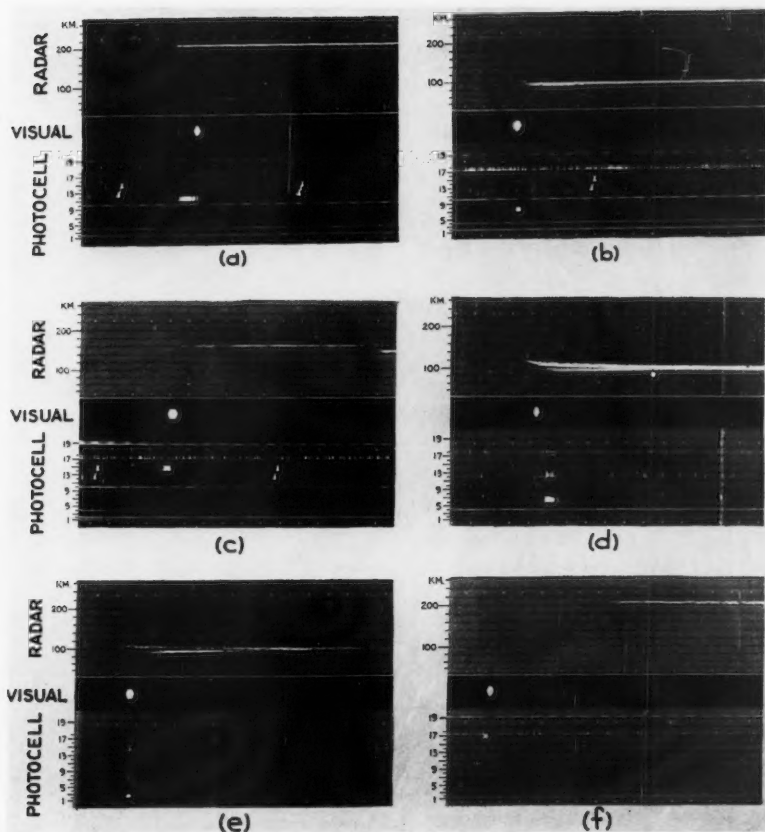


FIG. 3. Selected photographs showing coincidences between photocell, radar and visual observations.



only connections between the outdoor photocell assembly and the display located indoors are two coaxial cables, one to supply the trigger pulse to the gating circuits and the other to transmit the combined signal outputs to the remote display.

### Observations

The photocell system was tested intermittently during the autumn of 1949, and the first operational run was made during the observations of the Geminid shower, December 12-14, 1949. Three radar stations and one continuous-wave Doppler station were in operation. During the hours of darkness, direct meteor cameras and spectrographs were used and a crew of three to four experienced observers plotted visual meteors under Dr. Millman's direction. Examination of the radar-photocell film records revealed an appreciable number of apparent time coincidences between radar meteor echoes and the photocell signals. However, the present discussion will be confined chiefly to those meteors for which a coincident visual observation was available, because the plotted position and path of the meteor and its estimated visual magnitude are necessary in analyzing the value of the photocell observing technique. Twenty-two triple coincidences between radar, visual, and photocell observations were selected and are summarized in Table I. Four meteors for which no radar echo was recorded have also been included.

The sky coverage of the photocell system is shown in Fig. 4. The zenith is at the center and the outer boundary is approximately on the horizon. The correlation between the visually plotted paths and the photocell records is reasonably good if allowance is made for the observational errors. The average error of the visual plotting is of the order of  $3^\circ$  in both azimuth and elevation but an individual plot may have a considerably greater error. The boundaries of the individual photocell sectors are not sharp but have a wide penumbra, and may furthermore be in error by a few degrees.

The grouping of the majority of the meteors in the western half of the sky is not accidental, nor does it imply that the eastern photocells were operating inefficiently. As a general rule the average meteor will be detected by the radar system only when its elongation from the radiant,  $\alpha$ , is near  $90^\circ$ , though a bright meteor may often be detected at any elongation. It may be shown (1) that this condition tends to limit the radar observations to those meteors occurring in a zone across the sky opposite to the radiant. Between the hours 1930 E.S.T. and 0100 E.S.T. the true bearing of the Geminid radiant lay in the eastern sector. Thus, most of the triple coincidences between radar, photocell, and visual meteors should occur in the western part of the sky, since most of the observed meteors were Geminids.

The first column of Table II gives the mean visual magnitude of the meteor seen by the photocell system, and the second column lists the mean visual magnitudes of all visual meteors recorded during the selected observing periods.



TABLE I

Meteor No.	Photocell time E.S.T.	Radar time, sec.	Visual time, sec.	Geminid or non-Geminid	Visual mag.	Visual elongation from radiant ( $\alpha$ )	Detected by photocell No.'s	Photocell chart No.'s of Visual position plot	Fig. No.
Dec. 12, 1949									
1	19 <sup>h</sup> 37 <sup>m</sup> 35 <sup>s</sup> .2	36 <sup>s</sup> .0	35	G	2.5	65°-78°	6	1	
2	20 07 00.2		00	G	2	70-78	6	1, 6	
3	20 16 16.0	14.6	15	G	1	108-120	12	6, 12	
4	20 24 27.4	31.8	32	N	2		6	5, 9	
5	20 38 15.6	15.5	16	G	1	70-86	7	1, 7	
6	20 42 22.1		23	N	1		17	3, 17	
7	20 52 59.5	58.5	(53 <sup>m</sup> )00 <sup>s</sup>	G	1	47-54	9	9	3(a)
8	20 58 43.0	43.0	44	G	0	85-99	11	10, 11	
9	21 36 19.2		20	N	3		9	9	
10	22 23 49.8	49.5	49	G	0.5	62-81	7	7	3(b)
11	22 35 27.1	27.7	27	G	2	49-57	5	5	
12	22 39 07.0		07	G	0	49-60	16	2, 16, 15	
13	22 41 43.9	44.1	45	N	2		7	7	3(c)
14	22 51 54.8	55.3	57	G	-1	70-89	14	7, 14	
15	22 54 19.5	20.5	20	G	-1	83-90	14	14	
Dec. 13, 1949									
16	19 28 42.0	45.0	42	G	-2	37-51	4	4, 3	3(d)
17	19 30 20.8	19.5	20	G	-3	60-92	6, 12	1, 6	
18	20 12 43.3	43.1	52	G	-3	76-93	6	6, 7	
19	20 27 02.1	02.3	03	G	-1.5	84-104	10	10	
20	21 01 21.0	22.2	22	G	-2	30-42	9	8, 9	
Dec. 14-15, 1949									
21	21 06 31.6	31.0	31	G	-1	44-66	2, 14	3, 2	3(e)
22	23 26 07.8	09.0	06	G	-0.5	81-98	14	14	
23	23 48 20.0	26.5	20	G	-0.5	27-32	16	17, 16	3(f)
24	00 48 32.3	38.0	33	G	0	58-67	8	19, 8	
25	00 58 49.0	53.5	50	G	0.5	25-34	16	2, 16	
26	01 09 40.9	40.6	41	N	-0.5		7	7	

TABLE II

Observing period	Mean magnitude of photocell meteors	Mean magnitude of all visual meteors	Differential magnitude
Dec. 12, 1949 1937-2255 E.S.T.	1.1	2.3	1.2
Dec. 13, 1949 1928-2102 E.S.T.	-2.3	1.5	3.8
Dec. 13-14, 1949 2106-0110 E.S.T.	-0.3	1.9	2.2
All periods	0.0	2.1	2.1



The sensitivity of the photocell system during the December 12th period appears to have been about 1 magnitude less than that of the eye. The data are weighted in favor of the visual observations because all of these have been averaged, including the faintest meteors, but the photocell data include only the brighter ones for which identification was positive. The performance of the photocells has dropped considerably on the next two nights, partly owing

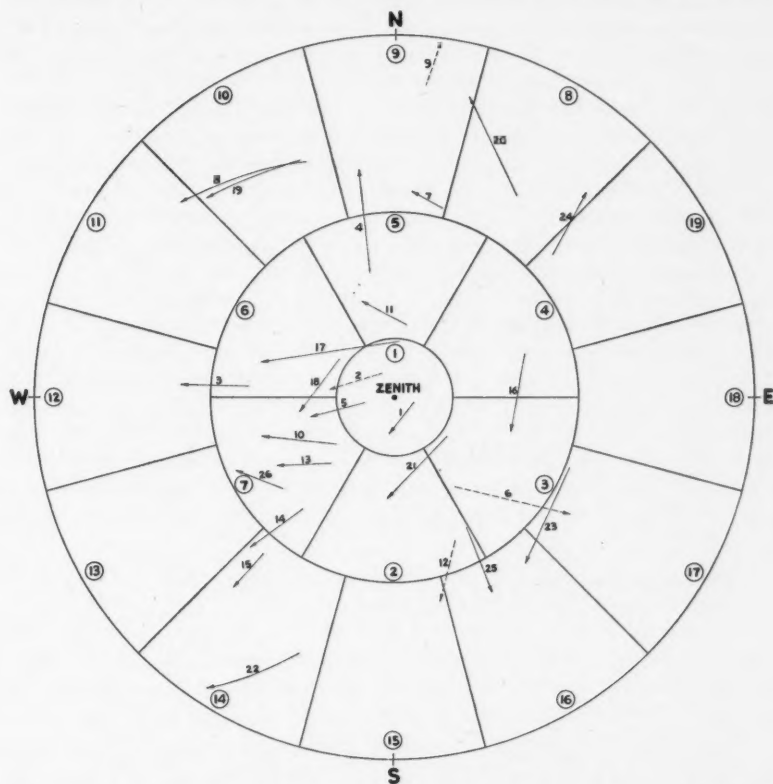


FIG. 4. Photocell coverage chart. This is a stereographic projection; the radii of the inner, middle, and outer circles are respectively  $18^\circ$ ,  $54^\circ$ , and  $90^\circ$ . Photocell coverage areas are indicated by circled numbers. Solid arrows—plots of photocell-visual-radar meteors. Dotted arrows—plots of photocell-visual meteors.

to poorer observing conditions as indicated by a similar, though smaller depreciation of the visual magnitudes. The photocell battery voltages deteriorated with time and the cold weather and were below normal on the last two nights, which would account for the poorer relative performance of the photocell system.

While the sensitivity limit of the photocells appeared to be about the second magnitude a large number of visual meteors in the range zero to second magnitude were not definitely recorded by the photocells. On the other hand the photocells did record a smaller number of probable meteors which were not visually observed, although coincident radar echoes were sometimes noticed. A similar effect has been remarked in the correlation between radar echoes and visual meteors when the fainter magnitudes are considered. The radar-visual relationship is not yet fully understood; often a bright visual meteor yields a weak meteor echo and vice versa. The principles of production and detection of a radio echo from the ionized gas column left by the meteor differ considerably from the production and detection of visible light, but the main differences between the photocell and the eye lie in relative sensitivity and spectral response. The spectral response curve of the 931-A photocell has a maximum at 4000 Å and is down by 50% at 3200 Å and 5400 Å, which suggests that these photocells may discriminate against the slow meteors of red or orange color. The sensitivity of the photocell as used in this application is limited by the variations in starlight, light of the night sky, aurora, and other ambient light, and not by inherent noise in the photocells or amplifiers. The noise level output of the photocell drops in proportion to the decreasing size of the aperture, and fainter meteor magnitudes could be detected against the star background simply by reducing the aperture. Adding more photocells with smaller apertures to the system would not only improve the sensitivity but would also increase the accuracy of position plotting, but there is an economic limit to this procedure (the amplifier and gate units alone contained 140 vacuum tubes, exclusive of the number in the C.R.T. display unit). Alternatively, one could employ the same number of photocells to cover a smaller portion of the sky.

Owing to an instrumental defect in the gate circuits, which has since been rectified, the occurrence of a strong light signal in one of the photocell channels caused the sensitivity of several of the adjacent channels to be depressed momentarily, or, in some instances, to introduce fainter spurious signals in other channels. More of the meteors listed in Table I might have been recorded by two or more photocells were it not for this effect.

A few detailed comments follow on some of the meteors listed in Table I, and on the photographs of Fig. 3. Reference should be made to Table I and to Fig. 4.

#### *Meteors No. 1 and 4.*

The visual plots for these meteors lie adjacent to the chart areas where they were seen by the photocells. The visual plots may have been in error by a few degrees, or the coverage of Photocell No. 6 may have differed appreciably from the nominal outline shown in Fig. 4. The time discrepancies in the case of Meteor No. 4 leave some room for doubt, though it is not unusual for the radar echo to occur seconds after the passage of the meteor, and the visual observers were occasionally late in marking.

*Meteor No. 8. (Fig. 3a)*

The light signal from Photocell No. 11 was coincident with the radar echo and endured for 1.2 sec., with indication of flares toward the end.

*Meteor No. 9.*

This was so low in the horizon that the radar echo, if there were one, would have occurred at a greater range than the maximum of 260 km. appearing on the record. The photocell signal was strong enough to suggest that the visual observer may have underestimated the meteor brilliance.

*Meteor No. 10. (Fig. 3b)*

The signal from Photocell No. 7 has lasted 0.3 sec. The noise level of Photocell No. 17 has been set too high.

*Meteor No. 15. (Fig. 3c)*

The radar echo occurred about 1 sec. later than photocell signal.

*Meteor No. 17. (Fig. 3d)*

The photocells did not register till the meteor approached  $\alpha = 90^\circ$ , appreciably later than the visual observation or the initial appearance of the radar echo.

*Meteor No. 18.*

A remark on the recorder's sheet indicates that the recorded visual time was several seconds late.

*Meteor No. 21. (Fig. 3e)*

The photocells have detected the luminosity at a later part of the meteor path than have the visual observers. This is confirmed by the position of the meteor plot in Fig. 4. Signals in other gates are spurious.

*Meteor No. 23. (Fig. 3f)*

The radar echo was delayed 6.5 sec. after the visual and photocell times. This is characteristic of the echoes from bright meteors near the radiant ( $\alpha = 27^\circ$ – $32^\circ$  for this meteor), which are often several seconds late in appearance, and may show multiple echoes (e characteristic (1)), and long duration; in this case the echo lasted for 110 sec.

*Meteor No. 25.*

Another example of a delay in the appearance of the radar echo when the observed meteor path is close to the radiant.

It will be remarked from Table I and the Chart, Fig. 4, that Meteors Nos. 2, 3, 5, 6, 8, 14, 17, 20, 21, 23, 24, and 25 all appear to have registered on the photocells toward the end of the visual path, or even beyond the plotted paths. The data for Meteor Nos. 16 and 18 suggest that the photocell detected these

meteors earlier than the visual observers. In the majority of cases the evidence indicates that the meteor luminosity increases toward the end of the visual path.

### Conclusions

At this stage in the development of the photoelectric meteor detector no attempt will be made to interpret the observations exhaustively because of imperfections in the instrumentation. Several minor defects were found in the electrical circuits, some of which have since been remedied. The sky coverage of each photocell was known only approximately. The addition of a long cone shield in front of each aperture would not only aid in locating the field of view more accurately but would greatly reduce the penumbra at the edges of the field, caused by the present position of the aperture a couple of inches away from the photocell surface. During the strong visual showers it would be advantageous to regroup the photocell units to cover the sky area in the neighborhood of  $90^\circ$  from the radiant, where more of the radar meteors occur. By narrowing the apertures both the sensitivity of the photocells and the accuracy of position plotting would be proportionally improved.

The present photocell system, operating under favorable circumstances, appears to be capable of detecting first magnitude meteors on the average, with a sensitivity limit about the second or third magnitude. The precision of time measurement is of the order of 0.05 sec. and could be improved if required. The over-all nonlinear response of the system, from the photocells through the amplifiers and gates to the display C.R.T., precludes the quantitative measurement of the rise and fall of the meteor luminosity, though variations in luminosity can be detected.

The value of the photocell system as an aid to the visual and radar observations has been demonstrated. It is not unreasonable to expect that further refinements in the instrumentation may put the photocell detector on a par with the human observer in respect to sensitivity and position plotting, with the advantage of providing a completely automatic permanent record. Direct photography will yield more accurate and detailed information about the meteor than the photocells can offer, but the time co-ordinate is lacking, and the sensitivity of the existing meteor cameras is less than that of the present photocell system. The Super-Schmidt meteor cameras now under development are expected to be capable of photographing third magnitude meteors. Even if the accurate timing feature only were utilized the photoelectric meteor detector might well prove a valuable aid to the operation of the Super-Schmidt cameras, because the exact time of apparition of the meteor is required for a complete reduction of the direct photographs.

### Acknowledgments

Mr. B. E. Bourne was responsible for the design of the amplifier and gate circuits, which were constructed by Mr. J. D. Stewart and Mr. W. T. Foster. Mr. S. M. Panagapko made the photocell units and assisted in the test program.

Helpful advice from Dr. Peter M. Millman, of the Dominion Observatory, has been freely available, and the indispensable co-operation of his staff, especially Miss M. McKee, in making and reducing the visual observations, is gratefully acknowledged.

### References

1. McKINLEY, D. W. R. and MILLMAN, Peter M. Proc. Inst. Radio Engrs. 37:364. 1949.
2. McKINLEY, D. W. R. and MILLMAN, PETER M. Can. J. Research, A, 27:53. 1949.
3. MILLMAN, PETER M. and McKINLEY, D. W. R. J. Roy. Astron. Soc. Can. 42:121. 1949.
4. MILLMAN, PETER M. and McKINLEY, D. W. R. Sky and Telescope, 8:114. 1949.

## STUDY OF IONIC CRYSTALS UNDER ELECTRON BOMBARDMENT<sup>1</sup>

BY D. E. MCLENNAN<sup>2</sup>

### Abstract

Electron bombardment experiments have been carried out on small crystals of the alkali halides within the electron microscope. Crystals of two size ranges were bombarded at high intensity, and evidence of a generalized photographic effect within the ionic group of solids is presented. The first group of crystal specimens ranged in size from 0.2 to 0.002 cm., the bombardment causing the formation of F-centers and entrapped metal colloids in the crystal lattice. Ionization pulses were observed to occur in the region of the specimen during bombardment. The second group ranged in size from 10 to 0.01  $\mu$ , observations on the effects of bombardment being carried out with electron diffraction techniques. A process has been suggested to explain the phenomenon of ionic crystals which appear to lose their centers under high electron beam intensity in the electron microscope.

### Introduction

The electron beam employed in electron microscopes must be of relatively high energy (order of 40 kv. or greater) to penetrate a useful thickness of solid specimen material. It is not surprising, then, that such beams at high intensity (order of 1 amp. per sq. cm.) have been observed to affect the specimen material. Specimen changes appear to be based on one or both of the methods by which electrons may interact with solids: (1) heating, and (2) electronic excitation. Examples in which the former interaction predominates are quite simply cited since melting or sublimation occurs. In the latter case, however, changes may be caused in crystal structure or even in chemical composition. Watson (7) (1948) has discussed specimen changes based on variations in structure of iron oxide, tungsten oxide, and tetra-copper calcium oxychloride. Hamm and VanNorman (5) (1948) have reported variations in structure in two metallo-organic pigments. The effect of temperature on these changes is discussed by both authors. Burton, Sennett, and Ellis (1) (1947) have reported an interesting form of specimen change in the alkali halides. In this case clear patches are seen to form within the crystal after the beam intensity has been increased beyond some critical value. The clear patches ultimately spread throughout the crystal, leaving behind only a thin wall to outline its initial position (see Fig. 1). Depending upon the alkali halide, one can often observe motion of material both as crystallites and as globules inside the crystal during its 'evaporation'. Interest in this specimen change has prompted the work reported in this paper.

### Ionic Crystals and Color Centers

Ionic crystals, of which the alkali halides are the best examples, are so named because their atomic components appear to exist in the crystal lattice as ions

<sup>1</sup> Manuscript received August 18, 1950.

Contribution from the Department of Physics, University of Toronto, Toronto, Ont.

<sup>2</sup> At present employed with the Defence Research Board, Valcartier, Que.

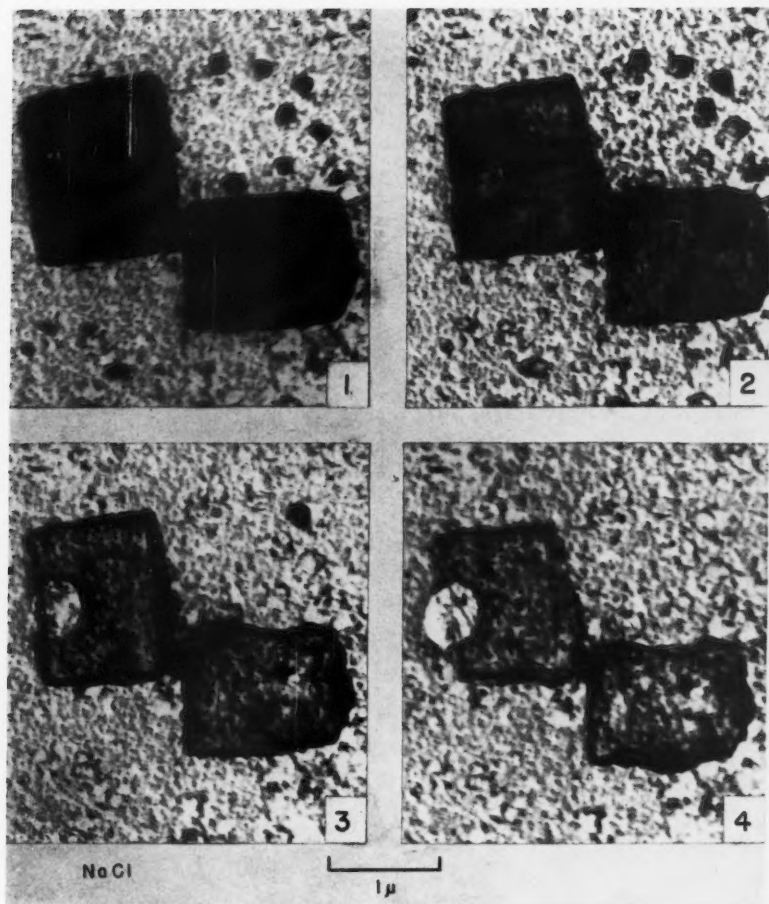
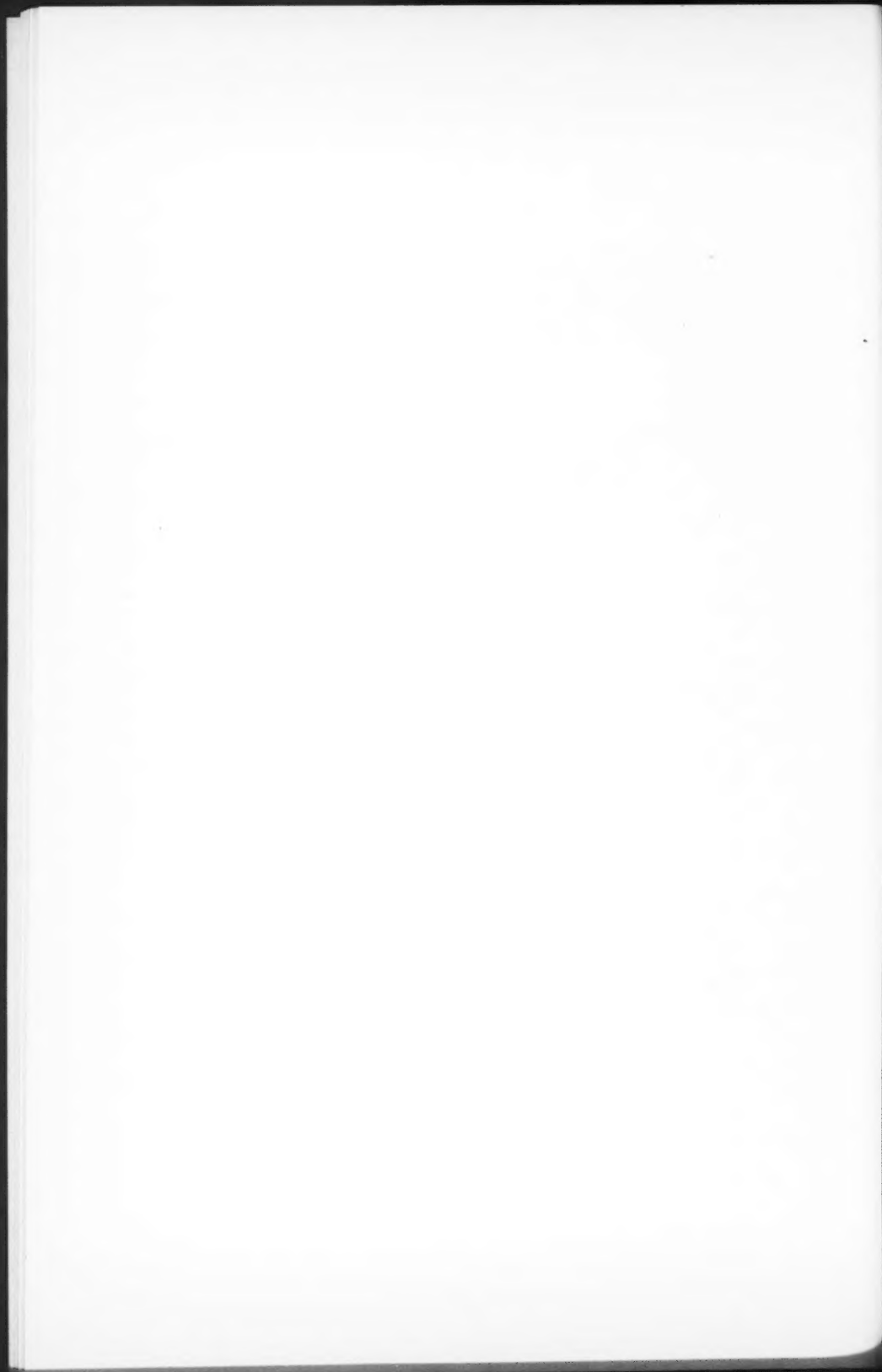


FIG. 1. Electron micrographs showing the effects of electron bombardment of NaCl crystals.





rather than as molecules. An important characteristic of these materials arises from the fact that any crystal defect due to a missing lattice point (Schottky defect) leads to holes that bear a net charge. These positively and negatively charged holes must exist in equal numbers in an electrically neutral crystal and give rise to the characteristic ionic conductivity and to the phenomenon of color-centers in the alkali halides (Mott and Gurney) (6). Defects appear to exist in all crystals, the ratio of defects to lattice points at room temperature in the best annealed crystals being about  $10^{-4}$ . Color or F-centers were investigated quite extensively by R. W. Pohl and his coworkers at Göttingen, Germany, in the 1920's. They found that color-centers could be produced by irradiation of the crystal with ultraviolet, X-rays, or cathode rays, and also by heating the crystal to about 600°C. in an atmosphere of the alkali metal. The absorption band giving rise to the color in crystals of the alkali halides so treated is due to the transitions of electrons trapped at missing negative lattice points, that is, Schottky defects of the positive hole type. In the case of color-centers formed by irradiation of the crystal (KCl) with X-rays, Estermann, Leivo, and Stern (2) (1949) have shown that the density of the crystal decreases in proportion to the number of color-centers formed. This indicates that the defects giving rise to color-centers are formed largely by the radiation. In the case of crystals heated in the metal vapor, Pohl and coworkers have shown that an excess of the metal in proportion to the number of color-centers exists in the colored crystals. They have also investigated alkali halides colored by the presence of excess metal existing as a colloid within the crystal lattice (Gyulai) (3, 4). In this case the color is not the same as that due to color-centers nor does it appear to be due to electronic transitions. The color seems to depend, rather, on the size of the colloidal particles. The color-centers for sodium chloride are, for example, yellow, while the color imparted by the colloid is blue-purple. Both forms of coloration may be produced by heating the crystal in the metal vapor. The color-centers are formed first and are "frozen-in" if the crystal is quenched from the high temperature at which they are formed. As the cooling rate is decreased the probability of forming the colloid appears to increase rapidly.

### Experimental Investigation

Electron bombardment experiments were carried out on crystals of sodium chloride and potassium chloride in two different ranges of size, hereinafter called macro and micro. Crystals in the size range 0.2 to 0.002 cm. were chosen as the macrospecimens since they could be observed during bombardment under low magnification in the electron microscope and, as well, examined after bombardment under the light microscope at 100X. The crystals were formed from water solution of the salt on specimen meshes prepared from 100 mesh per inch copper screen, which was carefully cleaned by electrolytic polishing. The microcrystals ranged in size from 10 to  $0.01\mu$  and the crystals were formed on the conventional Formvar-covered nickel or stainless steel electron microscope specimen meshes by vacuum evaporation of the salt.

Investigation of the microspecimens was carried out before and after bombardment by employing electron diffraction techniques. The electron microscope was used throughout the bombarding experiments since a relatively high intensity (order of  $1/3$  amp. per sq. cm.) may be obtained at an electron energy of 40 to 50 kv.

### *Bombardment of Macrocystals*

A special specimen holder was developed for the University of Toronto model 1944 electron microscope, to contain the specimen mesh and one or two (as desired) insulated electrodes. The electrodes were connected to an external voltage source through a high resistance (2 Megohms). Any ionization caused by the bombardment in the region of the specimen could then be detected as a voltage pulse by connecting an oscilloscope across the high resistance.

As a preliminary to electron bombardment experiments, cleaned specimen meshes both plain and insulated with a thin Formvar film were bombarded and attempts were made to observe ionization. These blank experiments gave no indication of voltage pulses on the oscilloscope; however, an indication of the production of secondary electrons was obtained by sweeping the fine electron beam across one of the mesh wires. The steepness of the pulse that appeared depended on the sweeping rate. The pulse was obtained with the single electrode at 250 v. positive with respect to the specimen mesh. Zero voltage on the electrode showed a very slight indication of secondary electron collection while 250 v. negative showed none whatever.

With the intense electron beam concentrated on a crystal of sodium chloride, pulses of positive sign were obtained with negative electrode voltages and pulses of negative sign with positive electrode voltages. No pulses were obtained with the collector electrode at the same potential as the specimen mesh. Calculation of the ion currents required to produce the pulse amplitudes observed showed them to be of the order of  $2 \mu\text{a}$ . It should be noted, however, that the pulse amplitude was seen to depend markedly on crystal size, larger crystals (0.2 to 0.02 cm.) giving larger pulses. In general an induction period of from 5 to 10 sec. was required from the instant of playing the concentrated beam on to a crystal until pulses were formed. The pulses appeared to occur randomly and looked like the ionization "noise" obtained in gas discharge tubes (e.g. VR 105, 150, etc.). The same sort of phenomenon was observed with potassium chloride crystals, but the pulses were in general about one-fifth as large in magnitude. The use of the electron microscope at low power facilitated knowing whether or not the beam was impinging on a crystal. Pulses were never obtained with the beam not playing on a crystal nor were they observed until a certain critical beam intensity was surpassed. It was not possible to measure this critical intensity since the variable was the beam cross section rather than the total current. Attempts were made to collect the ions produced during bombardment, on a specimen mesh placed on the collector electrode. After bombardment the collector mesh was examined by the methods of electron

diffraction without removing specimen and collector to the air. The results were inconclusive since in several instances only fine crystallites of sodium chloride were detected.

Examination of the specimen mesh under the light microscope after electron bombardment showed that the crystals of sodium chloride were highly colored. Crystals which had been irradiated at low intensity (considerably less than 0.1 amp. per sq. cm.) were yellow and amber. However, those upon which the intense beam (at 0.1 amp. per sq. cm. or greater) had impinged showed considerable damage and were a deep blue-purple in color. The latter crystals were the ones which also had given ionization pulses under bombardment. Further examination of the bombarded specimens over a period of one year has shown that the purple coloration remained permanent while the yellow color faded within a week to 10 days. Bombarded specimens of potassium chloride showed crystals colored both blue and magenta. The former faded within a week while the latter have remained stable so far for a year.

The unstable yellow coloration in bombarded sodium chloride appeared to be due to the presence of F-centers while the blue-purple color was assumed to be caused by the presence of a sodium colloid within the crystal. As a check on this assumption, two simple experiments were carried out on purple NaCl crystals: (1) a purple crystal was dissolved in a drop of water under the light microscope, and (2) another purple crystal was sealed up in a damp atmosphere of chlorine for a period of six weeks with occasional heating to about 200°C. In the first experiment bubbling was observed until all of the blue coloration disappeared; in the second, examination of the crystal after six weeks showed some reduction in color and the formation of a new clear crystalline overlayer. This was deemed fairly conclusive evidence of the presence of free sodium.

#### *Bombardment of Microcrystal Specimens*

The Formvar-covered specimen mesh with its layer of microcrystals was mounted in the specially designed specimen holder and placed in the electron microscope. Bombardment of an area of the specimen defined by a single mesh opening (order of 0.010 cm. square) was carried out at high intensity after which an electron diffraction pattern was taken of the bombarded material. Specimens of lithium, sodium and potassium chlorides were examined in this manner both before and after electron bombardment. In all cases "extra" rings appeared in the diffraction pattern of the bombarded salt. As a further check, electron diffraction pictures were taken of the same salt with the alkali metal evaporated on it. The  $d/n$  values for the "extra" rings produced both by electron bombardment and by the evaporated metal were calculated assuming the  $d/n$  values of the pure salt from X-ray measurements. In general the "extra" lines in both patterns may be accounted for by the presence of the alkali metal, its oxide, hydroxide or carbonate. Tables I and II are a typical solution of the patterns for bombarded lithium chloride and lithium chloride with evaporated lithium metal. The oxides and carbonate appear to be formed

inside the microscope even at the relatively high vacuum which exists there ( $10^{-4}$  to  $10^{-5}$  mm. of mercury). Fig. 2 sector (a) shows the diffraction pattern of lithium chloride itself, sector (b) that caused by electron bombardment, and sector (c) that due to the evaporation of metallic lithium on to the salt as a substrate. Evaporation of the metal was carried out inside the electron microscope and the diffraction patterns were taken without removing the specimen to the air.

The results for sodium and potassium chlorides were similar, the "extra" rings being caused by the presence of the free metal, its oxides, hydroxide or carbonate. As well as these three salts, four other ionic salts were investigated.

TABLE I  
LiCl BOMBARDED

Ring No.	$2r$	$\log 2r$	$d/n$	$\log d/n$	$\log K$	Crystal plane
1	10.08	1.0033	4.13	0.6157	(1.6190)	$\text{Li}_2\text{CO}_3$ : 4.16*
2	12.95	1.1123	3.21	.5067	(1.6190)	—
3	14.04	1.1473	2.963	.4718	1.6191	LiCl 111**
4	14.95	1.1747	2.78	.4438	(1.6185)	$\text{Li}_2\text{CO}_3$ : 2.80
5	16.18	1.2089	2.566	.4092	1.6181	LiOH: 2.75
6			2.47			LiCl 200
7	21.15	1.3253	1.96	.2932	(1.6185)	$\text{Li}_2\text{CO}_3$ : 2.47
8	22.89	1.3598	1.815	.2589	1.6187	Li 111
9	25.87	1.4128	1.61	.2057	(1.6185)	LiCl 220
10	26.84	1.4288	1.548	.1896	1.6184	$\text{Li}_2\text{CO}_3$ : 1.61
11	28.04	1.4478	1.481	.1707	1.6185	LiCl 311
12	29.35	1.4676	1.42	.1509	(1.6185)	LiCl 222
13	33.40	1.5237	1.244	.0948	(1.6185)	Li 211
14	35.32	1.5480	1.177	.0709	1.6189	Li 220
15	36.15	1.5581	1.147	.0598	1.6179	LiCl 331
						LiCl 420

TABLE II  
LiCl WITH EVAPORATED LITHIUM

Ring No.	$2r$	$\log 2r$	$d/n$	$\log d/n$	$\log K$	Crystal plane
1	13.35	1.1255	2.96	0.4717	1.5972	LiCl 111
2	14.85	1.1718	2.66	.4250	(1.5968)	LiOH : 2.67
3	15.39	1.1872	2.566	.4092	1.5964	LiCl 200
4	15.98	1.2036	2.47	.3926	(1.5962)	$\text{Li}_2\text{CO}_3$ : 2.47
5	21.74	1.3373	1.815	.2589	1.5962	Li 110
6	24.21	1.3840	1.63	.2115	(1.5955)	LiCl 220
7	28.38	1.4530	1.39	.1415	(1.5945)	$\text{Li}_2\text{O}$ 220
8	34.20	1.5340	1.147	.0595	1.5935	$\text{Li}_2\text{CO}_3$ : 1.61
9	37.24	1.5710	1.047	.0200	1.5910	$\text{Li}_2\text{O}$ 331
						Li 211
						LiCl 420
						LiCl 422

$\log 2r + \log d/n = \log K$ :—based on the Bragg law  
where:  $2r$  = measured ring diameter,  $d/n$  = crystal plane spacing,  
 $K = 2\lambda$ , the instrument constant.

\*  $\text{Li}_2\text{CO}_3$ : 4.16 means the crystal plane in  $\text{Li}_2\text{CO}_3$  of spacing 4.16 Å.

\*\* LiCl : 111 means the 111 plane of LiCl.

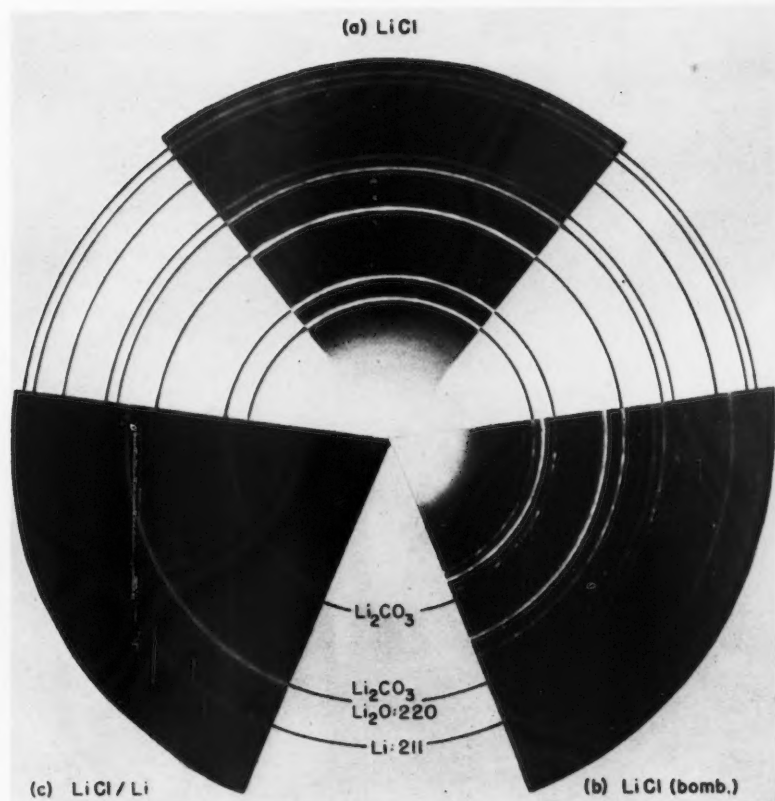
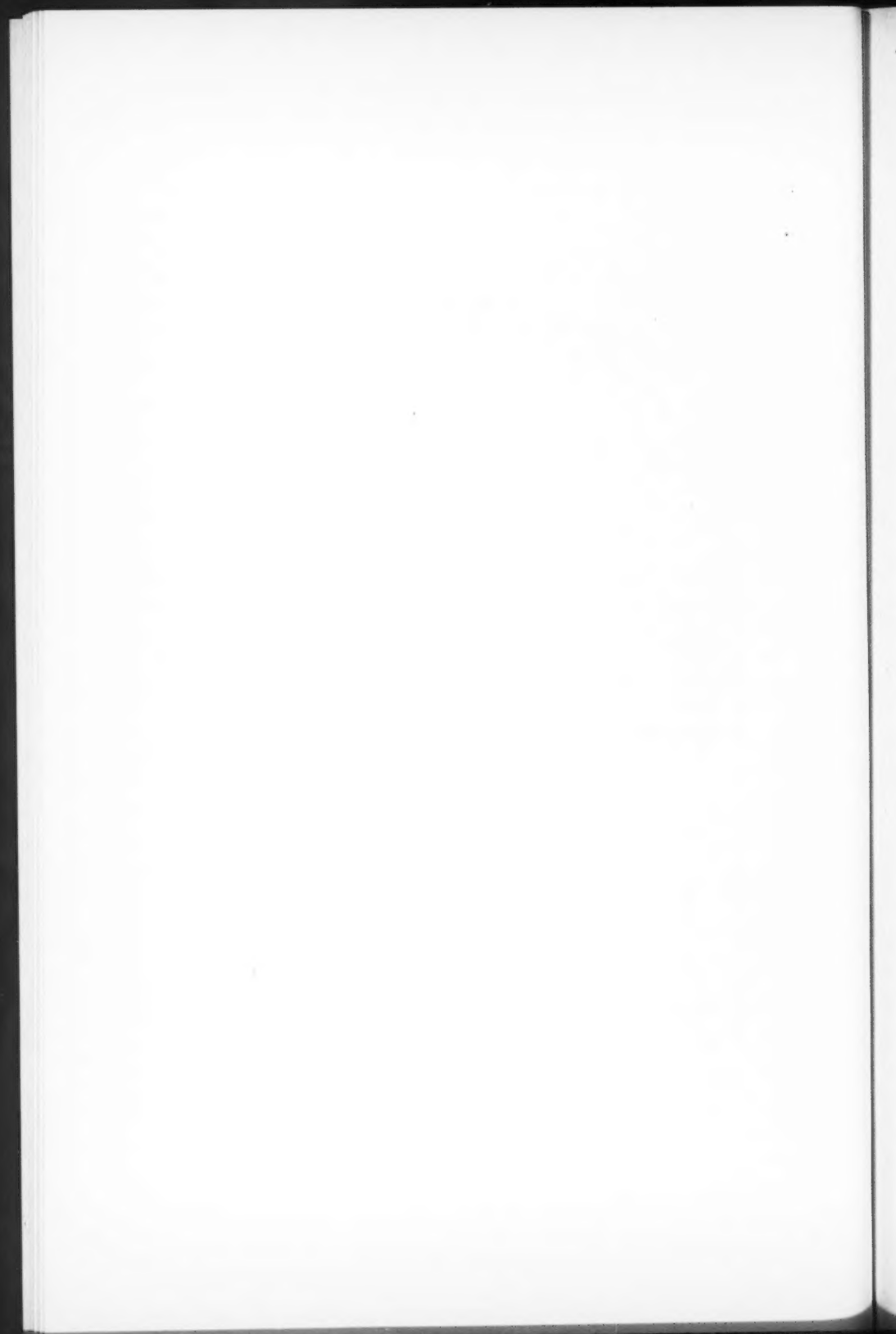


FIG. 2. Electron diffraction patterns (a) normal LiCl,  
 (b) bombarded LiCl showing "extra" rings,  
 (c) LiCl with evaporated Li indicating some of the same "extra" rings.



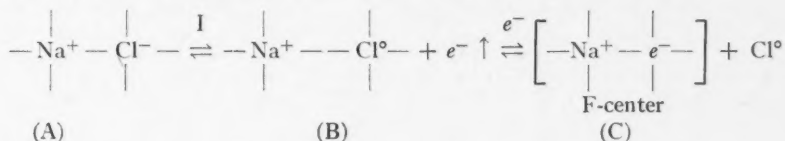


These were caesium chloride, sodium bromide, thallium chloride, and calcium fluoride, all of which showed "extra" rings caused by the bombardment. Full solutions for the rings were obtained in the last three cases only, since the data for the caesium oxides and carbonates were not available. Again the presence of the metal or its oxidation products could account satisfactorily for the extra rings.

### Discussion

It appears from this work that something comparable to the photographic process is occurring in all of the ionic materials investigated, the "print-out effect" in the silver halides appearing to be part of a more general phenomenon characteristic of ionic crystals. For this reason the process may be termed a "generalized photographic effect".

The following process is now suggested as an explanation of the specimen change observed to occur in the alkali halides under electron bombardment. First of all the formation of color-centers appears to be an equilibrium process. This was observed by Estermann, Leivo, and Stern (2) (1949) when they pointed out that X-ray irradiation of KCl for periods longer than 8½ hr. failed to show any increase in the number of color-centers. We may then write an equilibrium equation to describe the formation of a color-center:



(A) represents an ionic bond between sodium and chlorine ions in the sodium chloride lattice; the presence of a radiation I (in this case, the electron beam) will ionize one of the lattice points. The excited lattice point may then capture the most loosely bound electron in the Na-Cl configuration. This is the valence electron of sodium which has moved into the valence band of Cl<sup>0</sup> to form Cl<sup>-</sup>, and which accounts for the ionic binding. (B) is an intermediate configuration in which a sodium ion and a neutral chlorine atom are left with very little binding between them. The chlorine atom is then assumed to move off interstitially under the temperature vibrations of the lattice. The sodium ions surrounding a vacant negative ion lattice point (Schottky defect) cause a positive hole which may then trap a free electron to form an F-center (C). The presence of free chlorine in the lattice may cause this process to go the other way and re-form a normal lattice. If the intensity of the bombarding beam is increased, the equilibrium moves to the right; any localized increase in the amount of free chlorine will cause the equilibrium to move to the left again, thus reducing the number of F-centers. As the number of F-centers is increased by increasing I, the lattice will become more and more unstable until it collapses. However, an increase in the amount of free chlorine and in the temperature of the lattice from electron bombardment will cause the

chlorine to escape to the outside. There is thus a tendency to have more free chlorine at the outside of the crystal than at the center; it is logical then that when collapse does begin it should begin at the center. This catastrophic degradation of the crystal is proposed as the reason for the specimen change observed by Burton, Sennett, and Ellis (1), for the blue-purple macrocrystals and for the "extra" rings in the diffraction patterns of bombarded microcrystalline specimens.

Since the catastrophic degradation seems to occur only after a critical intensity has been surpassed, it would be interesting to see whether an intense beam of soft X-rays could be made to degrade the alkali halides in a similar fashion.

### Acknowledgments

The author would like to acknowledge his helpful discussions with Dr. G. D. Scott under whose direction this work was conducted; also thanks are due Dr. R. S. Sennett for his permission to use the micrographs in Fig. 1. The writer is indebted to the Research Council of Ontario for scholarships held at the University of Toronto during the tenure of which most of this work was carried out.

### References

1. BURTON, E. F., SENNETT, R. S., and ELLIS, S. G. *Nature*, 160: 565. 1947.
2. ESTERMANN, I., LEIVO, W. J., and STERN, O. *Phys. Rev.* 75 (2): 627. 1949.
3. GYULAI, Z. *Z. Physik*, 35: 411. 1926.
4. GYULAI, Z. *Z. Physik*, 37: 890. 1926.
5. HAMM, F. A. and VANNORMAN, E. *J. Applied Phys.* 19: 1097. 1948.
6. MOTT, N. F. and GURNEY, R. W. *Electronic processes in ionic crystals*. Oxford University Press. 1940.
7. WATSON, J. H. L. *J. Applied Phys.* 19: 713. 1948.

# ENERGY SPECTRUM OF NEUTRONS FROM A THORIUM ACTIVE DEPOSIT - BERYLLIUM SOURCE<sup>1</sup>

BY D. A. BROMLEY<sup>2</sup>

## Abstract

The energy spectrum of the neutrons emitted when beryllium is bombarded with alpha particles from Th (C + C') has been determined by measuring the ranges and directions of recoil of protons produced in a cloud chamber by the neutrons. The maximum energy of the neutrons was found to be about 15.5 Mev., within experimental error of the calculated maximum, 14.4 Mev. Many neutrons were found with energy of about 2.15 Mev. and the structure in the remainder of the spectrum can be attributed to the existence of energy levels in C<sup>12</sup> at about 7.1 and 4.5 Mev. The angular distribution of the protons scattered by the neutrons from this source was isotropic to within experimental error.

## Introduction

No data have been found on the energy distribution of the neutrons from a thorium (C + C') - beryllium source. We have determined this distribution by measuring, in a cloud chamber, the energy transferred to the proton in the neutron-proton scattering interaction.

We have investigated the angular distribution of the recoil protons and have found it to be isotropic for the neutron energies found here. This is in agreement with the distributions found by many other investigators (1, 3, 4, 8).

## Apparatus

The cloud chamber used was of the rubber diaphragm, "constant pressure" type, 10 in. in diameter and 3 in. in depth. This chamber has been described in detail by Lillie (6). Stereoscopic photographs were taken with two Kodak 35, 35 mm. cameras rigidly mounted above the chamber in an aluminum casting. Illumination was provided by discharging a 100  $\mu$ f. condenser charged to 2000 v., through two G.E. FT-126 mercury vapor discharge lamps mounted on opposite sides of the chamber.

The operation of the complete cloud chamber unit was controlled by a series of thyatron delay circuits in cascade and was completely automatic. This control scheme was chosen in preference to the motor-driven cam system because of its greater flexibility.

The reprojection unit used in studying the track photographs has been described elsewhere (2). The track images were reprojected through their re-

<sup>1</sup> Manuscript received August 25, 1950.

Contribution from the Department of Physics, Queen's University, Kingston, Ontario. Based on a thesis submitted to the Faculty of Applied Science, Queen's University, in partial fulfillment of the requirements for the M.Sc. degree.

<sup>2</sup> Holder of Shell Oil Fellowship and National Research Council of Canada Scholarship. Present address: Physics Department, University of Rochester, Rochester, New York.

spective camera lenses. When the two images of a track were brought into coincidence on a screen all distortion due to asymmetry in the cameras or their mounting was automatically avoided.

The neutron source used is shown in Fig. 1. This source was so designed that it could be placed entirely within the cloud chamber. The aluminum disk carrying the active deposit *F* is 6 mm. in diameter and the beryllium sheet *E* has an areal density of 0.932 gm. per cm<sup>2</sup>.

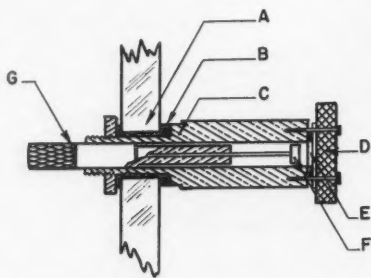


FIG. 1. This shows the neutron source with the glass walls of the cloud chamber *A*, the rubber gasket for sealing the chamber *B*, the brass cylindrical sleeve *C*, the 6 mm. lead sheet *D*, the beryllium metal sheet *E*, the aluminum disk carrying the thorium active deposit *F*, and the removable plug which holds the source in position *G*.

The 6 mm. lead sheet *D* served to reduce the beta and gamma background in the chamber due to source activity. This lead affected the energy of less than 5% of the neutrons passing through it with energies greater than about 2 Mev. since the mean value for the total cross section of these neutrons in lead is about 5.5 barns (5) corresponding to a mean free path of about 10 cm. The source was mounted inside the glass chamber wall as shown and was so constructed that the aluminum disk could be removed for reactivation without disturbing the gas mixture in the chamber. This construction also prevented the gas mixture from coming into contact with the thorium ( $C + C'$ ), thus preventing contamination of the chamber.

### Experimental Method

The thorium preparation used in obtaining the thorium active deposit sources was an intimate mixture of radiothorium and ferric oxide carrier. This mixture was placed in a brass cylinder with an insulating cover such that the aluminum disk could be suspended in the space above the radiothorium and maintained at a 400 v. negative potential relative to it. Strong alpha-active sources were obtained in this way with even half-hour exposures. On comparison with a standard radium source the activity of a typical deposit has been estimated at 4 millicuries. The sources were removed from the charging device at least one-half hour before use. Hence the alpha particles were those from  $Th (C + C')$ .

It was not possible to operate the chamber which was available for this work at pressures greater than atmospheric. Since the stopping power of hydrogen is in the ratio of 0.2: 1 to that of air it was decided to use a 5: 1 mixture of nitrogen and oxygen at atmospheric pressure as the noncondensable gas in order to stop higher energy particles within the chamber and to make the conditions for good tracks less critical. This mixture simulates standard air.

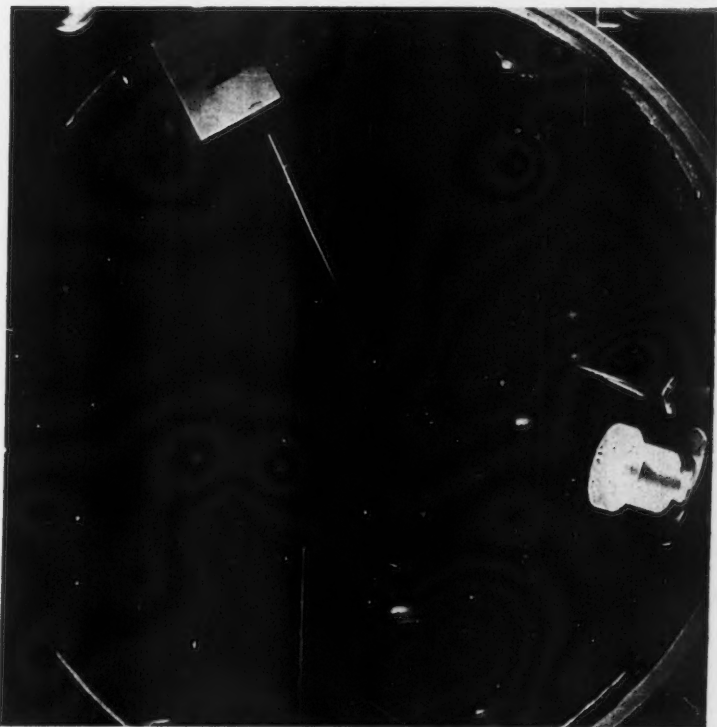


FIG. 2. This shows a typical proton recoil. The neutron source is shown in position on the chamber wall at the lower right. The "2" is the serial number assigned to, and photographed with, this exposure.

This gas mixture was then saturated with a 50% ethyl alcohol, 25% water, and 25% acetone mixture, with the result that the number of hydrogen atoms available in the chamber was between 40 and 60% of the number when using pure hydrogen.

Over 1000 stereoscopic exposures were taken on Ansco Ultra Speed Pan film and were given standard processing in Kodak D-11 developer and Edwal Rapid Fixer. Fig. 2 shows a typical proton track.

Before and after each series of photographs a polonium source was inserted in the chamber and the alpha tracks photographed for use in reducing the observed proton ranges to ranges in standard air. If we assume that the stopping power of the gas mixture relative to air is constant at all points along the range and if the apparent range  $R_a$  of an alpha particle is measured under conditions identical with those during the measurement of the apparent proton range  $L_a$  then we may write  $L_0 = L_a \times R_0/R_a$ , where  $R_0$  is the known range of the alpha particle in standard air and  $L_0$  is the reduced value of  $L_a$  referred to standard air.

In using the reprojection system to make measurements on the track photographs (2) the track images were projected into the object space corresponding to the chamber volume and onto a plane, white, circular screen. This screen was magnetically clamped in such a way that it was free to rotate about any diameter passing through its center while this center could be moved to any point in the object space. In making measurements on the proton tracks, the track images were brought into coincidence on the screen surface; the screen was moved bodily until this track lay on a diameter and the screen support was locked rigidly to the base plate of the unit by energizing the base magnet. The screen proper was then rotated about this diameter until the images of the neutron source were brought into coincidence and then was locked in place by energizing the support magnet.

Proton ranges were measured with a mean error of less than 1 mm. and the angles between the track and a line joining the beginning of the track to the center of the neutron source were measured to the nearest degree. Since this source had finite dimensions it was necessary to reject all tracks starting within 3 cm. of the source in order to reduce the probable errors in angle. From the geometry of the system, using an average distance of 10 cm. from the source to the beginning of the track, the mean expected error in the angle of recoil is less than two degrees. All tracks which struck the chamber walls were rejected in the energy measurements but not in the measurement of angle if the clear length was greater than 5 cm.

When the angles and ranges of tracks indicated a neutron energy far in excess of any to be expected from the source (25 Mev.) the tracks were rejected. These were doubtless due to neutrons from the source which had previously been scattered by the material of the chamber. The number of such tracks was less than 8% of the total number measured.

The measured proton ranges were converted to the reduced range referred to standard air by making measurements of the ranges of polonium alpha tracks photographed before and after each series of proton track exposures and using the conversion relation noted previously; the corresponding energies were obtained from the range-energy curves given by Livingston and Bethe (7).

Conservation of energy and momentum leads to the well known expressions  $E_p = E_n \cos^2 \phi$  and  $dE_n = 2E_n \tan \phi d\phi$  where  $E_p$  is the proton recoil energy,

$E_n$  the incident neutron energy and  $\phi$  the angle of recoil measured between the proton track and the initial direction of the neutron. Using this relation the neutron energies corresponding to each proton track were calculated. The energy distribution obtained in this way must be corrected for the variation of the neutron-proton scattering cross section with energy in order to obtain the true energy spectrum. These corrections were obtained from the smooth curve given by Goldsmith, Ibser, and Feld (5), which gives the measured variation of the total scattering cross section with energy. Fig. 3 is the final corrected spectrum based on measurements on 750 recoil protons.

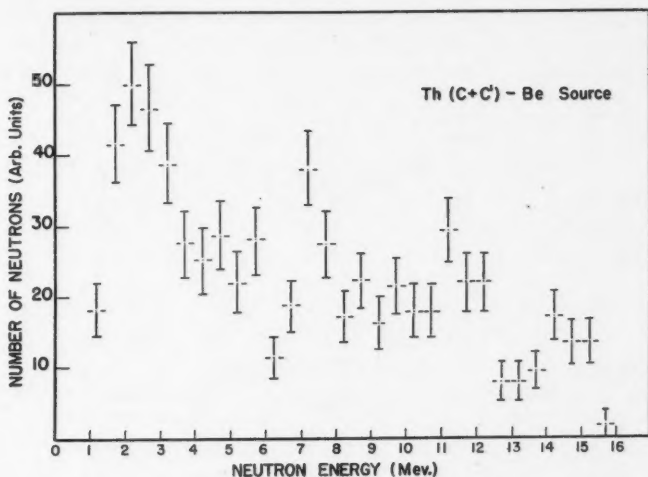


FIG. 3. Energy distribution of neutrons from a  $\text{Th } (C + C')$ -Be source plotted in 0.5 Mev. intervals.

The angular data obtained in the energy measurements were used to check the angular distribution of the recoil protons. Since this distribution has been studied by many investigators it was considered of interest to compare our results with those obtained previously.

Let us represent the element of solid angle and the angle of recoil by  $dw_1$  and  $\theta$  in the center of mass system of co-ordinates and by  $dw_2$  and  $\phi$  in the laboratory system. In the center of mass system the number of protons recoiling through unit solid angle  $w_1$  at an angle of recoil  $\theta$  may be represented by a function of this angle,  $f(\theta)$ .

$$\frac{dN}{dw_1} = f(\theta). \quad \text{From simple trigonometry } \theta = 2\phi \text{ and}$$

$$\frac{dw_1}{dw_2} = \frac{\sin \theta d\theta}{\sin \phi d\phi} = 4 \cos \theta. \quad \text{Hence } \frac{dN}{dw_2} = 4f(2\phi) \cos \phi$$



$$\begin{aligned} \text{Since } dw_2 &= 2\pi \sin\phi \, d\phi & \frac{dN}{d\phi} &= 8\pi f(2\phi) \sin\phi \cos\phi \\ & & &= g(\phi) \sin\phi \cos\phi. \end{aligned}$$

By definition if the angular distribution is isotropic  $f(\theta)$  is constant or

$\frac{dN}{d\phi} = K \sin\phi \cos\phi$ , where  $K$  is constant. This shows that a plot of  $\Delta N/\Delta\phi$  against  $\phi$  should have a flat maximum at  $\phi = 45^\circ$  and should drop to zero at  $\phi = 0^\circ$  and  $90^\circ$ .

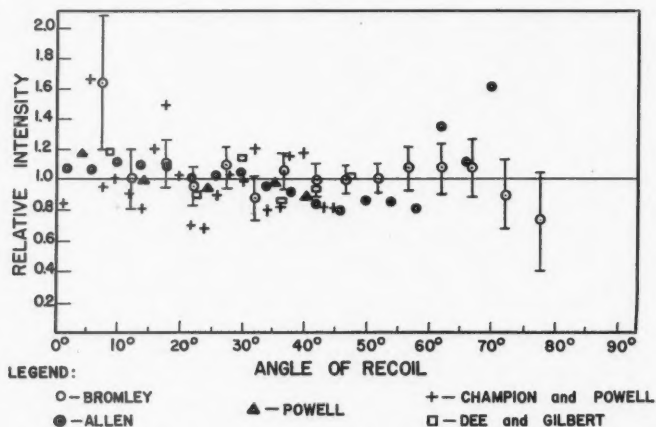


FIG. 4. Ratio of experimental to isotropic distribution. (Powell's results are as quoted in Rosenfeld (8).)

The ratio of the observed number of tracks in each five degree interval to the number calculated for an isotropic distribution was computed and plotted against the mean angle in the interval. The result is shown in Fig. 4 together with the results of four other investigations, (1), (3), (4), (8), whose data have been reduced to this form for comparative presentation.

### Discussion of Results

As noted previously, the only alpha particles are those from Th ( $C + C'$ ) at 6.0537 and 8.7759 Mev. We neglect the very rare long range alphas from the thorium  $C'$ .

These alpha particles penetrate varying distances into the beryllium crystal structure before initiating a neutron producing reaction. Furthermore, the angle of neutron emission is unknown and the amount of momentum carried off by the product nuclei varies over a wide range. For these reasons we should expect to find, especially in a source in which the alpha emitter and beryllium are intimately mixed, that the neutron energy groups would combine to give

a continuous spectrum. With the source in use here the incident alphas are more nearly monodirectional at impact, whence we should expect that the more intense groups, or in this case, combinations of two groups, might appear superimposed on a continuous spectrum. The spectrum obtained (Fig. 3) shows these features. The only maxima which we are statistically justified in considering are those corresponding to neutron energies of about 14.5, 11.5, 7.3, and 2.15 Mev.

The major neutron producing reaction in this source is  ${}^4\text{Be}^9(\alpha, n){}^6\text{C}^{12}$ . Tollestrup, Fowler, and Lauritsen (9) give 5.708 Mev. as the  $Q$  value. These authors also give a  $Q$  value of  $-1.67$  Mev. for the reactions  ${}^4\text{Be}^9(\gamma, n){}^2\text{He}^4$ ;  ${}^4\text{Be}^9(n, 2n){}^2\text{He}^4$ ;  ${}^4\text{Be}^9(\alpha, n){}^3\text{He}^4$ , which are also energetically possible in this source. The cross sections for these reactions are low and in this type of source the  $(n, 2n)$  reaction in particular is unimportant since the beryllium in which the neutrons are produced is in the form of a thin sheet.

The calculated maximum energy for a source of this type is 14.49 Mev. for the 8.78 Mev. alphas and 11.76 Mev. for the 6.05 Mev. alphas.

The angular distribution of recoil protons indicated  $45^\circ$  as the most probable angle of recoil and we have previously given the mean expected error in the angle as less than two degrees. This gives  $dE_n = 0.069 E_n$ , where  $E_n$  is the neutron energy. In  $E_n = 15.5$  Mev.,  $dE_n = 1.1$  Mev., hence the observed maximum energy of about 15.5 Mev. is within the experimental error of the calculated value.

We do not consider that the statistics are sufficiently good to warrant calculation of the neutron distributions for transitions to the excited states of  $\text{C}^{12}$  as was done in detail by Whitmore and Baker (10). We note, however, that the maxima at 11.5 and 14.5 can be explained by considering that they are due to transitions to the ground state of  $\text{C}^{12}$  in which the full alpha energy has been transferred to the neutron. By similar reasoning we can consider that the maximum at 7.3 Mev. is due to the superposition of two groups, one corresponding to transitions to the 7.1 Mev. excited level of  $\text{C}^{12}$  and resulting from the 8.78 Mev. alphas and the other corresponding to transitions to the level at about 4.5 Mev. resulting from the 6.05 Mev. alphas since we have  $14.49 - 7.3 \approx 7.2$  Mev. and  $11.76 - 7.3 \approx 4.5$  Mev.

The relatively large number of high energy neutrons found here is considered due to the particular type of source used in which the mean angle of neutron emission with respect to the direction of the incident alphas is much smaller than in a source consisting of a mixture of the alpha emitter and beryllium.

The large number of neutrons in the 2-3 Mev. range can be considered as part of the previously mentioned continuous distribution. The sharp decrease below 2 Mev. is considered due to experimental cutoff. For neutron energies below 2 Mev. only the recoil protons making small angles with the neutron momentum would have sufficient energy to be detected owing to the relatively high background in the chamber.

The statistics here are not sufficient to enable us to give any definite evidence as to the existence or nonexistence of the previously found energy levels in the  $C^{12}$  nucleus at about 7.1, 4.5, and 2.5 Mev. Whitmore and Baker (10) have summarized the latest available data on these levels.

As seen from Fig. 3 the angular distribution of the recoil protons is isotropic to within the precision of this work. This precision is not great enough to indicate any small deviations from isotropy, if they exist. The experimental excess in the number of tracks at low angles can be explained by noting that for these small angles of recoil a greater fraction of the neutron energy is transferred to the protons. The probability of detection is thus increased. For large angles the energy transferred is small and the probability of detection above the chamber background is decreased, thus explaining the experimental deficit in the number of tracks at large angles. Many investigators have studied this distribution and have found no conclusive evidence for any departure from isotropy in the energy range considered here.

### Acknowledgments

The author wishes to acknowledge his indebtedness to Dr. J. A. Gray for suggesting the problem and for his advice and interest in the work. He would also thank Mr. R. D. Bradfield for his advice and for the excellent workmanship on parts of the apparatus.

Finally, he would thank the Shell Oil Company of Canada and the National Research Council of Canada for financial assistance.

### References

1. ALLEN, J. R. M.A. Thesis. Queen's University. 1949.
2. BROMLEY, D. A. and BRADFIELD, R. D. *Rev. Sci. Instruments*, 21: 190. 1950.
3. CHAMPION, F. C. and POWELL, W. *Proc. Roy. Soc. (London)*, A, 183: 64. 1944.
4. DEE, P. I. and GILBERT, C. W. *Proc. Roy. Soc. (London)*, A, 142: 1. 1933.
5. GOLDSMITH, H. H., IBSEY, H. W., and FELD, B. T. *Revs. Modern Phys.* 19: 259. 1947.
6. LILLIE, A. B. M.Sc. Thesis. Queen's University. 1947.
7. LIVINGSTON, M. S. and BETHE, H. A. *Revs. Modern Phys.* 9: 268. 1937.
8. ROSENFELD, L. *Nuclear forces*. Interscience Publishers, Inc., New York. 1948. p. 126.
9. TOLLESTRUP, A. V., FOWLER, W. A., and LAURITSEN, C. C. *Phys. Rev.* 78: 372. 1950.
10. WHITMORE, B. G. and BAKER, W. B. *Phys. Rev.* 78: 799. 1950.

## PULSER FOR CYCLOTRON OSCILLATOR<sup>1</sup>

BY W. H. HENRY AND J. D. KEYS<sup>2</sup>

### Abstract

A pulser for the R.F. oscillator of the McGill synchrocyclotron is described. This pulser is triggered at a selected precise frequency and controls the oscillator for selected pulses or for predetermined exact periods of continuous operation.

### Introduction

In the direct exposure of photographic plates or in studies of very short activities it is frequently necessary to operate the cyclotron for short periods. In order that such periods be reproduced with accuracy a pulser has been built for controlling the R.F. oscillator of the McGill synchrocyclotron. Previous pulsers reported have either used a mechanical device to produce the triggering pulse (3), or have shut off the oscillator for a certain period of each f-m cycle by grid blocking (1). In the operation of the McGill pulser the oscillator is normally not oscillating, and is accurately triggered on at the desired frequency of the f-m cycle by the absorption of power from a low power oscillator by the dead tank circuit.

### Description of Apparatus

The frequency modulated voltage for the McGill cyclotron dee is provided by a class C grounded grid oscillator employing an 880 triode (2). Since the plate of the oscillator tube requires continuous water cooling, the tube is connected with the plate at d-c. ground and the filaments at high negative potential. In class C operation the grid of the tube is, on the average, several hundred volts negative with respect to the cathode. The d-c. supply is capable of delivering up to 10 kv. and thus the grid may be as low as 11 kv. below ground.

The operation of the oscillator is such that the actual duty cycle comprises only one-sixth of the total f-m cycle. In view of this it was considered advisable to arrange the pulser in such a way that the oscillator is normally not oscillating, and is permitted to oscillate only during the period of the duty cycle.

With this end in view, tests were made to determine the best method of blocking the oscillator by means of a sufficiently large negative voltage applied to the grid, at the same time keeping in mind that any switch inserted in this grid circuit must present the proper impedance to the tube when it is operating over the duty cycle. It was found that two 304TH triodes, connected in parallel and in series with a 500  $\Omega$  resistor, fulfilled the latter condition. A 2 kv. power supply was inserted across the 304TH combination with connections made in such a way that when the 304TH's are nonconducting the grid of the oscil-

<sup>1</sup> Manuscript received September 20, 1950.

Contribution from the Radiation Laboratory, McGill University, Montreal, Que.

<sup>2</sup> Holder of a Studentship under National Research Council of Canada.

lator tube is biased negative by this amount. Under these conditions the 880 tube will not oscillate. The 304TH combination then forms an effective switch since they can be made nonconducting and be switched on during the duty cycle. This circuit is shown in Fig. 1.

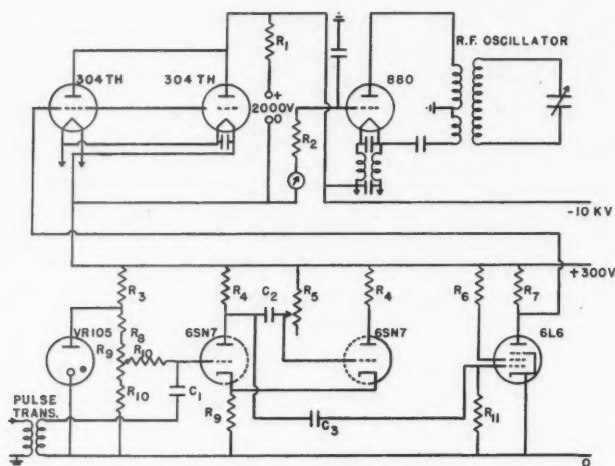


FIG. 1.

$R_1 = 250\ k$   
 $R_2 = 500\ \Omega$   
 $R_3 = 13\ k$   
 $R_4 = 22\ k$   
 $R_5 = 2\ Meg.$   
 $R_6 = 2680\ \Omega$

$R_7 = 2200\ \Omega$   
 $R_8 = 47\ k$   
 $R_9 = 10\ k$   
 $R_{10} = 27\ k$   
 $R_{11} = 390\ k$

$C_1 = 0.01\ mf.$   
 $C_2 = 0.002\ mf.$   
 $C_3 = 0.1\ mf.$

The 304TH's are biased to cutoff by current flowing through the plate resistor of the 6L6. The voltage for this tube and its control unit is provided by a 300 v. power supply whose positive side is connected to the negative terminal of the 2 kv. supply. The unbiased grid of the 6L6 is capacitance-coupled to the plate of the normally nonconducting tube of a uni-vibrator. Thus, when the uni-vibrator is in its stable state, the grid of the 6L6 is at the same potential as the cathode and hence the tube conducts strongly, providing sufficient bias in its load resistor to keep the 304TH's cutoff. However, when the uni-vibrator is triggered into its unstable state, a large negative square pulse appears on the grid of the 6L6 and it ceases to conduct, causing its plate to rise to the potential of the 300 v. supply, and hence removing the grid bias on the 304TH's. Under these conditions the 304TH's are capable of conducting and the R.F. oscillator proceeds to oscillate. The duration of the oscillation is controlled by the length of the square pulse appearing at the grid of the 6L6, which in turn is governed by the circuit constants of the uni-vibrator. These may be adjusted to give any length of pulse desired.

The grid of the uni-vibrator is at a potential of approximately 11,000 v. below ground, and since the triggering pulse must come from the ground level, the most suitable arrangement is a pulse transformer capable of withstanding this voltage.

The duty cycle of the oscillator extends from 25.2 Mc. to 21.9 Mc. whereas the frequency modulation cycle is from 27.9 to 20.9 Mc. From the point of view of other circuits, such as the timing pulser for the ion source, which must be pulsed at the start of the duty cycle, it is desirable to have the oscillator operating slightly before 25.2 Mc.

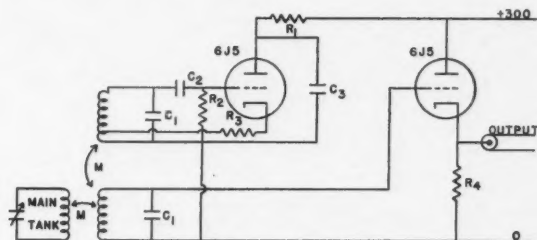


FIG. 2.

$R_1 = 22\ k$	$C_1 = 15\text{--}75\ \text{mmf.}$
$R_2 = 47\ k$	$C_2 = 25\ \text{mmf.}$
$R_3 = 300\ \Omega$	$C_3 = 0.01\ \text{mf.}$
$R_4 = 100\ k$	

In order to obtain a triggering pulse for the pulser the circuit shown in Fig. 2 is employed. A local low power oscillator (6J5) is coupled with a tuned circuit acting as a detector, which is coupled in turn to the main tank circuit. Both the local oscillator and detector are tuned to 27 Mc. Each time the main tank sweeps through this frequency, it absorbs energy and the amount absorbed depends upon the coupling. The drop in level of the detector is fed into a cathode follower which feeds the pulse to the delay and gating unit shown in Fig. 3.

The pulse obtained from the detector occurs at 27.0 Mc. and it is necessary to delay this pulse until the frequency of the main tank circuit reaches 25.4 Mc. This pulse, amplified by the 6SJ7, triggers the 2050 thyratron, whose output triggers a uni-vibrator and the square pulse obtained is differentiated to give a delayed positive pulse, which fires the second 2050 thyratron. The pulse from this thyratron can be fed directly into the pulse transformer, thus triggering the main pulser. The length of the square output pulse from the uni-vibrator is adjusted so that the delay in the appearance of the positive pulse is sufficient to allow the main tank circuit to reach 25.4 Mc. Since this time depends directly on the speed of the rotary condenser, the delay must be variable over fairly wide limits to accommodate the speeds which may be employed.

A considerable amount of energy is absorbed by the detector when the main oscillator is on. To prevent this from affecting the control circuits the 6SJ7 is gated. The output pulse from the first 2050 triggers a second uni-vibrator. The negative output pulse from this uni-vibrator is applied to the grid of a normally conducting 6SJ7. The voltage drop in the cathode resistor of this tube normally provides the screen voltage for the 6SJ7 amplifier. However, when the 6SJ7 is cut off, the screen of the 6SJ7 amplifier drops to zero and the tube ceases to conduct. In this manner any disturbance attempting to cause spurious triggers for the main oscillator is blocked.

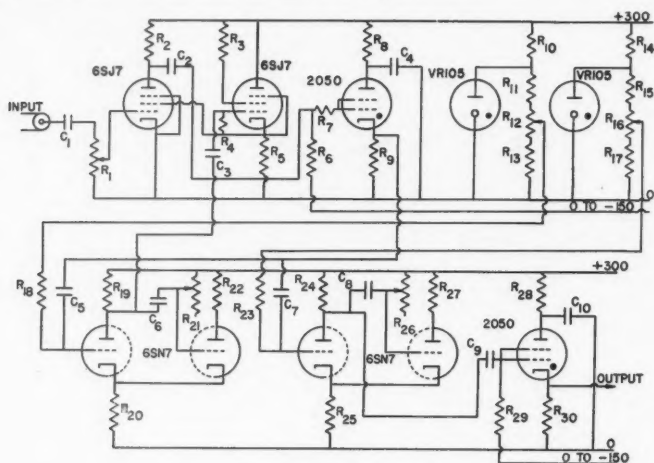


FIG. 3.

$R_1 = 750\ k$	$R_{16} = 10\ k$	$C_1 = 410\ \text{mmf.}$
$R_2 = 22\ k\ (2\ w)$	$R_{17} = 27\ k$	$C_2 = 150\ \text{mmf.}$
$R_3 = 100\ k$	$R_{18} = 27\ k$	$C_3 = 1\ \text{mf.}$
$R_4 = 100\ k$	$R_{19} = 22\ k$	$C_4 = 0.001\ \text{mf.}$
$R_5 = 22\ k\ (2\ w)$	$R_{20} = 10\ k\ (2\ w)$	$C_5 = 0.001\ \text{mf.}$
$R_6 = 1\ \text{Meg.}$	$R_{21} = 5\ \text{Meg.}$	$C_6 = 0.0125\ \text{mf.}$
$R_7 = 10\ k$	$R_{22} = 22\ k\ (2\ w)$	$C_7 = 0.001\ \text{mf.}$
$R_8 = 390\ k$	$R_{23} = 27\ k$	$C_8 = 0.06\ \text{mf.}$
$R_9 = 1\ k$	$R_{24} = 22\ k$	$C_9 = 410\ \text{mmf.}$
$R_{10} = 15\ k\ (10\ w)$	$R_{25} = 10\ k\ (2\ w)$	$C_{10} = 0.001\ \text{mf.}$
$R_{11} = 47\ k$	$R_{26} = 2.5\ \text{Meg.}$	
$R_{12} = 10\ k$	$R_{27} = 22\ k\ (2\ w)$	
$R_{13} = 27\ k$	$R_{28} = 390\ k$	
$R_{14} = 15\ k\ (10\ w)$	$R_{29} = 1.5\ \text{Meg.}$	
$R_{15} = 47\ k$	$R_{30} = 1\ k$	

Owing to slight unevenness in the teeth of the rotary condenser, it is not possible to tune the local oscillator to the exact top end of the modulation cycle. Hence the main oscillator tank circuit sweeps through the frequency of the local oscillator twice in each cycle, two pulses appearing at the input of the 6SJ7 amplifier. The first pulse passes through and triggers the first 2050 thyatron, and this in turn triggers the gate which blocks the second pulse, as well as 'hash' from the main oscillator.



Since it has been found necessary in some cases (i.e., nuclear plates) to expose for very short periods, the circuit shown in Fig. 4 can be inserted between the delay unit and the pulse transformer. The output pulse from the delay unit thyatron is applied to the grid of a second thyatron, which shares its cathode resistor with a 6F6. The bias on this thyatron is adjusted so that, with the 6F6 conducting hard providing additional bias in the cathode of the 2050, the tube does not fire on pulses from the delay unit. However, when the 6F6 is made nonconducting this additional bias is removed and the thyatron fires on the desired pulses. This condition is achieved by allowing a condenser previously charged to 300 v. to discharge itself through the grid resistor of the 6F6, thus cutting it off. The duration of the cutoff is determined by the time constant of this condenser and grid resistor. The latter is variable to provide for passage of pulses for times from zero up to one second.

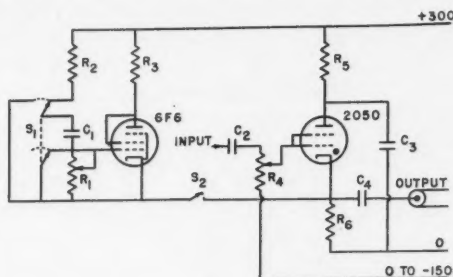


FIG. 4.

$R_1 = 3 \text{ Meg.}$   
 $R_2 = 40 \text{ k}$   
 $R_3 = 3 \text{ k}$   
 $R_4 = 1 \text{ Meg.}$   
 $R_5 = 390 \text{ k}$   
 $R_6 = 400 \text{ } \Omega$

$C_1 = 0.1 \text{ mf.}$   
 $C_2 = 0.01 \text{ mf.}$   
 $C_3 = 0.01 \text{ mf.}$   
 $C_4 = 0.01 \text{ mf.}$   
 $S_1 = \text{D.P.D.T.}$   
 $S_2 = \text{S.P.S.T.}$

The flexibility of the control units is such that any manner of triggering may be accomplished by inserting suitable circuits in place of the circuit of Fig. 4. In addition to this, all the controls for these circuits can be operated at the control desk of the cyclotron.

### Acknowledgment

The authors wish to express their thanks to Dr. J. S. Foster for his continued interest. Thanks are also due to Dr. R. W. Jackson and members of the Radiation Laboratory for many helpful discussions.

### References

1. BURKIG, J. W., HUBBARD, E. L., and MACKENZIE, K. R. *Rev. Sci. Instruments*, 20: 135. 1949.
2. TELFORD, W. M. Thesis, McGill University, Montreal, 31 Aug. 1949.
3. UNIVERSITY OF CALIFORNIA, RADIATION LABORATORY. Private communication.

## THE CALIBRATION OF PLATINUM RESISTANCE THERMOMETERS IN THE TEMPERATURE RANGE 11° TO 90°K<sup>1</sup>

BY J. M. LOS<sup>2</sup> AND J. A. MORRISON

### Abstract

A set of six platinum resistance thermometers of a form suitable for low temperature calorimetry has been made and calibrated in the region 11° to 90°K. by intercomparison with a similar thermometer which had been calibrated at the National Bureau of Standards. Above 90°K. calibration has been made on the International Temperature Scale.

Using the intercomparison data, it has been possible to derive a method whereby for these thermometers the scale for the region 20° to 90°K. may be found to within 0.002°C. by means of fixed points. The method applies a 'Z function' of the type used at the National Bureau of Standards (13), plus a corrective term which depends upon the resistance of the thermometer at the boiling point of hydrogen and upon the normal constants which are determined for the International Temperature Scale above 90°K.

### Introduction

As a preliminary step in the construction of a low temperature calorimeter assembly, it was necessary to make and to calibrate a set of platinum resistance thermometers. In view of the fact that the measurement of the temperature has an important bearing on the precision claimed for the calorimetry, it seemed desirable to describe the thermometers and the manner in which they were calibrated. In addition, factors have been found which pertain to the general problem of the establishment of a temperature scale in the region below the boiling point of oxygen.

The problem of establishing a temperature scale for the region below 90°K. is of course well recognized (4). At the National Bureau of Standards a provisional scale has been established (7) in terms of a gas thermometer, with a view to seeking first of all uniformity of temperature scales for the various laboratories doing low temperature work. That this much might be accomplished, a series of thermometers has been made by the Leeds and Northrup Company, and calibrated at the National Bureau of Standards. One of these, #718154, was purchased by the National Research Council and serves as the standard for the calibration of working thermometers used in this laboratory.

The objective of further work on this temperature scale is the establishment of a scale which agrees closely with the thermodynamic scale and which may be realized in terms of the resistance of platinum thermometers through the use of fixed points and a suitable interpolation formula. A scale established in this way could serve as an extension of the present International Temperature Scale (12). Perhaps the greatest difficulty has been to obtain a suitable inter-

<sup>1</sup> Manuscript received in original form July 20, 1950, and, as revised, September 11, 1950. Contribution from the Division of Chemistry, National Research Laboratories, Ottawa, Canada. Issued as N.R.C. No. 2339.

<sup>2</sup> National Research Laboratories Postdoctorate Research Fellow. Present address: Department of Chemistry, University of New Brunswick, Fredericton, N.B.

polarization formula. An empirical 'Z function' of the type first proposed by Cragoe (13)

$$Z = \frac{R_T - R_{54.363}}{R_{90.190} - R_{54.363}}$$

has been tested out at the National Bureau of Standards. The same tabulated relation between  $Z$  and  $T$  is used for all thermometers. Such a function may be used for the region between the triple point of oxygen (54.363°K.) and the boiling point of oxygen (90.190°K.) with considerable success, but a similar function,

$$Z = \frac{R_T - R_{20.273}}{R_{90.190} - R_{20.273}},$$

where the boiling point of equilibrium hydrogen is taken as 20.273°K., may give deviations as large as 0.05° from the real temperature. More recently, Hoge (6) has suggested another method in which a linear combination of two different  $R$ - $T$  functions is used. On the basis of the present work, it has been possible to derive a method which uses a single 'Z function' and a corrective term which is dependent only upon a knowledge of the resistance of the uncalibrated thermometer at certain fixed points. While the method operates very satisfactorily in the present instance, the thermometers here described have characteristics which are not too different, hence it would seem desirable for the method to be tried with thermometers made in other laboratories.

## Experimental

### *Description of the Thermometers*

The six resistance thermometers were made following the method of Meyers (9), the two designated as T-4 and T-5 being made first some nine months before the other four, which were taken from a set of 11 made at the one time. All the thermometers were made from the same batch of wire obtained from the Sigmund Cohn Company of New York. The dimensions of the mica crosses were made such that the thermometers fitted closely inside platinum thimbles 70 mm. long, 5 mm. diameter, and 0.2 mm. wall thickness. After being annealed to a constant ice point resistance by heating to temperatures above 450°C. in air, and after the steam and sulphur points had been determined, the thermometers were sealed off with a soft glass cap, the four leads (two current and two potential) being sealed through the cap. Before sealing, the thermometers were filled with an amount of dry helium corresponding to about 1/3 atm. pressure at room temperature.

The Leeds and Northrup thermometer # 718154, hereafter designated as T-S, had been made in a similar way but of somewhat smaller dimensions, the platinum thimble being approximately 47 mm. long, and 5 mm. diameter.

### *Determination of the Fixed Points of the International Temperature Scale*

For the determination of the fixed points at the boiling points of water and of sulphur, hypsometers of the type described by Beattie (1, 2) were used. The

atmospheric pressure was determined with a mercury manometer of conventional design, the heights of the mercury columns being compared with a calibrated steel scale mounted at the arms of the manometer. Appropriate corrections were made for capillary depression of the mercury, and the pressures were reduced to the height of a mercury column at 0°C. and standard gravity at the level of the resistance thermometer coil. From a large number of measurements, it appeared that the accuracy of pressure determination was 0.03 to 0.04 mm.

The ice point and oxygen point determinations were made in the conventional manner, the oxygen point apparatus being essentially that described by Scott (11).

Resistances were determined with a White double potentiometer. For the fixed point determinations, a steady current of about 1.2 ma. was passed through the thermometer circuit. The sensitivity of the measuring system was such that a change of 0.00001 ohm could be detected. For most of the thermometer intercomparisons which are described below, a steady current of 2 ma. was used. The current was raised to 5 ma. for some of the intercomparisons below 30°K.

TABLE I  
INTERNATIONAL TEMPERATURE SCALE CONSTANTS  
FOR THE RESISTANCE THERMOMETERS

Thermometer	$R_0$ abs. ohms	$\alpha \times 10^2$	Average deviation $\Delta\alpha \times 10^3$	$\delta$	Average deviation $\Delta\delta \times 10^4$	$\beta$	Average deviation $\Delta\beta \times 10^5$
T-S†	25.5110 <sub>1</sub>	0.392592		1.49179		0.11018	
T-1	24.5095 <sub>8</sub>	0.392591	8(13)	1.4914	2(4)	0.11079	8(3)
T-2	24.5800 <sub>6</sub>	0.392598	6(4)	1.4921	1(4)	0.11029	7(5)
T-3	24.3173 <sub>3</sub>	0.392575	5(5)	1.4908	1(6)	0.11118	4(4)
T-4	24.3107 <sub>3</sub>	0.392555	5(7)	1.4930	2(4)	0.11046	3(5)
T-5	24.2503 <sub>5</sub>	0.392550	7(14)	1.4923	2(5)	0.11079	*
T-6	24.4901 <sub>2</sub>	0.392577	7(9)	1.4919	0(3)	0.11073	5(3)

† Unrounded values determined at the National Bureau of Standards.

\* On the basis of later intercomparisons  $\beta$  adjusted the equivalent of 0.008° to this value.

In Table I are given the values of the constants of the thermometers in the Callender-VanDusen equation

$$t = \frac{R - R_0}{\alpha R_0} + \delta \left( \frac{t}{100} \right) \left( \frac{t}{100} - 1 \right) + \beta \left( \frac{t}{100} \right)^3 \left( \frac{t}{100} - 1 \right).$$

In columns 4, 6, and 8 are given the average deviations in the determinations of  $\alpha$ ,  $\delta$ , and  $\beta$  respectively. The numbers in brackets indicate the number of individual measurements which were averaged.

*Intercomparison of the Resistance Thermometers in the Region below 90°K.*

For the intercomparison, the thermometers were set into re-entrant wells in a copper block with Woods metal. Four wells were provided so the thermo-

meters were compared with T-S three at a time. The copper block was hung within the adiabatic shield of a low temperature calorimeter assembly which has been described elsewhere (10).

Altogether, some 30 comparisons of each thermometer with T-S were made in the temperature range 11° to 90°K. By keeping the difference in temperature between the block and the adiabatic shield as small as possible, practically all of the intercomparisons were performed without the temperature of the block changing. In any one set of intercomparisons, the measurement of the resistance of T-S was usually made alternately with the measurement of the resistance of each of the other three thermometers.

The adiabatic shield had been provided with a vapor pressure thermometer bulb, and this was used to check the indication of T-S at the boiling point of equilibrium hydrogen. The bulb was partially filled with about 1 gm. of  $\text{Nd}_2\text{O}_3$  which was prepared in the manner described by Taylor and, Diamond (14) and which served as the catalyst for converting the hydrogen to the equilibrium mixture. About 0.04 mole of pure hydrogen was condensed into the bulb and after a period of about three hours the steady value of the pressure and the resistance of T-S were determined simultaneously. The indication of the sensitive thermocouple between the block and the adiabatic shield was also recorded. The temperature of the vapor pressure thermometer was calculated from the formula of Woolley *et al.* (15) for "20.4°K. equilibrium hydrogen".

$$\log_{10} P = 4.64392 - \frac{44.3450}{T} + 0.02093T.$$

It was found that the indications of the thermometer T-S and the vapor pressure thermometer agreed to 0.008°. The vapor pressure thermometer bulb being situated on the adiabatic shield was really not ideal for the experiment, so the agreement is considered to be very satisfactory.

From the intercomparison data a calibration table for each thermometer, T-1 to T-6, was obtained by use of a method suggested by Hoge (5). For the smoothing of the data the resistance of an uncalibrated thermometer was expressed as a function of the resistance of T-S, i.e.,  $R_{\text{calc.}} = AR_{\text{T-S}} + B$ . The difference  $\Delta R' = R_{\text{obs}} - R_{\text{calc.}}$  was plotted against  $R_{\text{T-S}}$  with  $\Delta R'$  being made zero at about 26° and 86°K. The scatter of the points so plotted from the smooth curves was in general less than 0.00005 ohm. On the same graph was made a plot of  $\frac{dR_{\text{T-S}}}{dT}$  against  $R_{\text{T-S}}$ . It was now possible to make a resistance-

temperature table for each thermometer directly, with intervals of  $R$  such as to permit linear interpolation. For each value of  $R$  a preliminary value of the temperature was obtained through  $R_{\text{T-S}} = \frac{R-B}{A}$  and the calibration table of

T-S. The correction,  $\Delta T$ , to get the final temperature was determined from

$$\Delta T = - \frac{\Delta R'}{\frac{AdR_{\text{T-S}}}{dT}}.$$

The scale so derived was joined smoothly with the International Temperature Scale at the oxygen boiling point by adjusting the value of  $\beta$  for each thermometer so that the value of  $\Delta R' = R_{(\text{Internat.})} - R_{\text{calc.}}$  at 90.19°K. fell on the smooth curve of the  $\Delta R'$  against  $R_{T-S}$  plot. Such an adjustment is permissible because the intercomparisons may be performed more precisely than the determination of the oxygen point for the International Temperature Scale. For five of the thermometers the value  $\beta$  was changed by the equivalent of 0.001° or less. For T-5, an adjustment equivalent to 0.008° was required, indicating that a systematic error had been made in the oxygen point determination for that thermometer. However, in view of the consistency of the behavior of the other thermometers, it did not seem worthwhile to redetermine the oxygen fixed point for T-5.

While the scales are so joined smoothly at 90.19°K., continuity of the derivative of resistance with temperature does not follow necessarily. The derivative can be discontinuous owing to a deviation of the International Temperature Scale from the thermodynamic scale above the boiling point of oxygen.

*A Method of Determining the Scale for the  
Region 20° to 90° K. by means of Fixed Points*

The proposal of Cragoe (13) to use the function  $Z = \frac{R - R_{54.363}}{R_{90.190} - R_{54.363}}$  was tried with the thermometers used in the present work.\*

The resistances of the thermometers at the oxygen triple point (54.363°K.) were taken from the intercomparison data and not determined directly. Table II shows the maximum error arising from the determination of the temperature using this  $Z$  function rather than the intercomparison data.

TABLE II  
MAXIMUM ERROR INVOLVED IN USING  $Z$  FUNCTION IN  
THE RANGE 54.363° TO 90.190°K.

Thermometer	( $\Delta T$ ) max. in degrees
T-S	0.0002
T-1	0.0005
T-2	0.0007
T-3	0.0003
T-4	0.0011
T-5	0.0010
T-6	0.0005

The small value of the errors shown in the table suggests that these thermometers have similar characteristics to the one on which the table was based.

An attempt was now made to determine the temperature scale for the region from the boiling point of equilibrium hydrogen (20.273°K.) to the boiling point

\* A copy of the appropriate table relating the function  $Z$  to the temperature was placed at our disposal by the National Bureau of Standards.

of oxygen (90.190°K.) using a single  $Z$  function. A new  $Z$  table was calculated (Table III) with the function  $Z = \frac{R - R_{20.273}}{R_{90.190} - R_{20.273}}$  based upon T-S. The value of  $R_{20.273}$  was taken from the National Bureau of Standards calibration. For the thermometers T-1 to T-6 a plot was made of  $\Delta R$  against  $T$  for three degree intervals where  $\Delta R = R_{\text{table}} - R_{\text{intercomparison}}$  and a smooth curve drawn through the points. These curves are shown as solid lines in Fig. 1 where

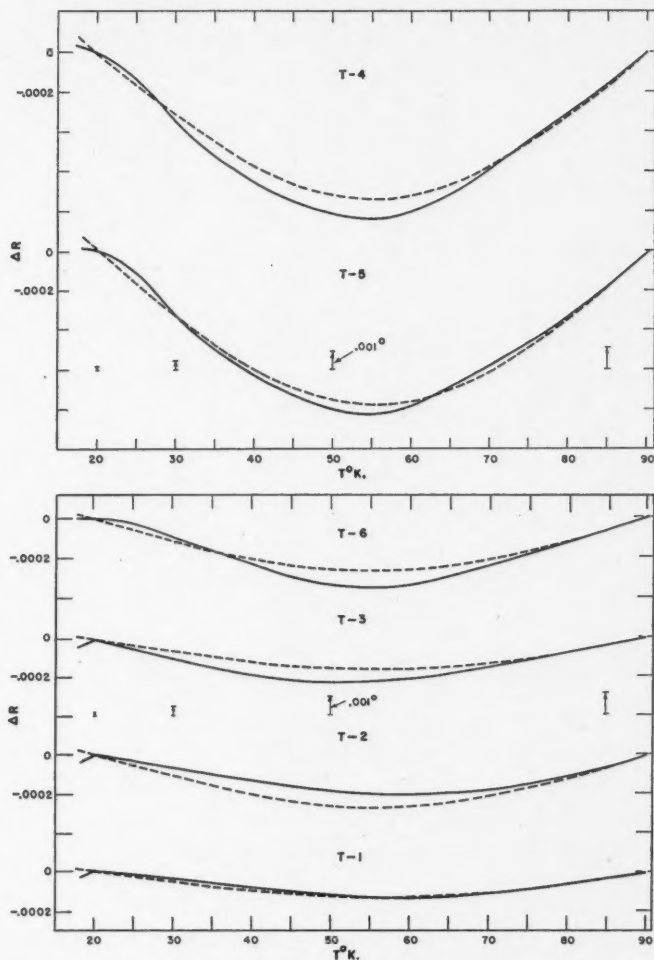


FIG. 1. The relationship between  $\Delta R$  and temperature for the six thermometers.  
 —  $\Delta R$  determined from the intercomparison data.  
 - - -  $\Delta R$  calculated from Equation (IV).



it is seen that for T-4 and T-5 a deviation as large as  $0.009^\circ$  is found at about  $55^\circ\text{K}$ .

A means was now sought to obtain a general formula to express the observed discrepancies in terms of the thermometer constants shown in Table I. Empi-

TABLE III  
Z-TEMPERATURE RELATIONSHIP FOR THE FUNCTION

$$Z = \frac{R - R_{20.277}}{R_{90.190} - R_{20.273}} \text{ BASED UPON T-S}$$

T°K.	Z	T°K.	Z
18	-0.006126	56	0.392516
19	-0.003680	57	0.409139
20	-0.000845	58	0.425902
21	+0.002406	59	0.442802
22	+0.006093	60	0.459827
23	+0.010240	61	0.476970
24	0.014857	62	0.494224
25	0.019962	63	0.511577
26	0.025562	64	0.529021
27	0.031667	65	0.546548
28	0.038276	66	0.564146
29	0.045396	67	0.581809
30	0.053023	68	0.599525
31	0.061159	69	0.617290
32	0.069797	70	0.635098
33	0.078929	71	0.652945
34	0.088547	72	0.670027
35	0.098640	73	0.688743
36	0.109193	74	0.706691
37	0.120192	75	0.724668
38	0.131620	76	0.742671
39	0.143461	77	0.760700
40	0.155700	78	0.778754
41	0.168316	79	0.796831
42	0.181295	80	0.814927
43	0.194621	81	0.833043
44	0.208278	82	0.851174
45	0.222252	83	0.869323
46	0.236526	84	0.887483
47	0.251087	85	0.905653
48	0.265916	86	0.923833
49	0.281003	87	0.942018
50	0.296330	88	0.960201
51	0.311880	89	0.978376
52	0.327642	90	0.996548
53	0.343600	91	1.014708
54	0.359738	92	1.032856
55	0.376046	93	1.050988

rically it was found that the curves could be approximated most simply by a sine function

$$\Delta R = a \sin (bT + c) \quad (1)$$

The quantities  $a$ ,  $b$ , and  $c$  were determined from the following conditions

$$(a) \Delta R = 0 \text{ at } T = 20.273^\circ\text{K.}$$

$$(b) \Delta R = 0 \text{ at } T = 90.190^\circ\text{K.}$$

$$(c) \frac{d\Delta R}{dT} = 0.01816486 (R_{90.190} - R_{20.273}) - \alpha R_0 (1 + 0.046594\delta + 0.345453\beta) \quad \text{at } 90.190^\circ\text{K.}, \quad (II)$$

where  $R_0$ ,  $\alpha$ ,  $\delta$ , and  $\beta$  are the constants of the Callender-VanDusen equation.

Equation (II) is derived on the assumption that at  $90.190^\circ\text{K.}$   $\frac{d\Delta R}{dT}$  is equal to the slope obtainable from  $\Delta R = R_{Z \text{ table}} - R_{\text{Internat.}}$

The factor 0.01816486 was found from the requirement that

$$\frac{d\Delta R_{T-S}}{dT} = 0 \text{ at } 90.190^\circ\text{K.}$$

From the above, Equation (I) becomes

$$\Delta R = -22.26 \{ 0.01816486 (R_{90.190} - R_{20.273}) - \alpha R_0 (1 + 0.046594\delta + 0.345453\beta) \} \sin (2.5745T - 52.19), \quad (III)$$

where the phase  $(2.5745T - 52.19)$  is expressed in angular degrees. Using Equation (III) the solid curves shown in Fig. 1 could be approximated quite reasonably, the largest deviation being one of  $0.003^\circ$  for thermometer T-3.

Closer examination of the data showed that except for T-6, the slopes of the  $\Delta R$  versus  $T$  curves at  $90.190^\circ\text{K.}$  departed significantly from those derivable from the Callender-VanDusen equation. Blaisdell and Kaye (3) have pointed out that part of the internal inconsistency of the International Temperature Scale can be due to differences in  $\delta$  for various thermometers. Further, from work of Hoge and Brickwedde (8) it appears that the indications of platinum resistance thermometers are generally too low between  $-182.97^\circ$  and  $0^\circ\text{C.}$  for large values of  $\delta$ . One might expect then that the observed differences in slope at the oxygen point would be dependent upon  $\delta$ . It was found that the differences could be reduced considerably by replacing  $\delta$  in Equation (III) by  $\delta + 1.4 (\delta - 1.4918)$ . Substitution gives then

$$\Delta R = -22.26 \{ 0.01816486 (R_{90.190} - R_{20.273}) - \alpha R_0 (0.902688 + 0.111826\delta + 0.345453\beta) \} \sin (2.5745T - 52.19). \quad (IV)$$

The plots of  $\Delta R$  versus  $T$  for each thermometer as determined from (IV) are shown as dotted curves in Fig. 1. The deviations of the calculated curves from those derived from the intercomparison data are nowhere larger than  $0.0001$  ohm, or in terms of a temperature deviation nowhere larger than  $0.002^\circ$ .

To summarize, it is proposed that the use of the Z table (Table III), with appropriate corrections to  $R$  evaluated by Equation (IV), may provide a convenient means of accurately establishing the temperature scale for platinum

resistance thermometers in the region  $20^{\circ}$  to  $90^{\circ}\text{K}$ . The addition of but one fixed point (at the boiling point of hydrogen) to those now required for the International Temperature Scale is necessary. The generality of the method can only be evaluated after it has been tested with thermometers of characteristics somewhat different from those used in this investigation. It is suggested that the scale in the region below  $20^{\circ}\text{K}$ . may be established most conveniently by direct comparison of the platinum resistance thermometer with a hydrogen vapor pressure thermometer. The vapor pressure thermometer would be required in any case for the determination of the fixed point at the boiling point of hydrogen.

### Acknowledgment

We wish to thank Dr. H. J. Hoge of the National Bureau of Standards for helpful suggestions, and for sending us the manuscript of a paper related to this work in advance of publication. Our thanks are due to Mr. G. Clement of the Central Workshops for handling so capably the making of the resistance thermometers.

### References

1. BEATTIE, J. A., BENEDICT, M., and BLAISDELL, B. E. Proc. Am. Acad. Arts Sci. 71: 327. 1937.
2. BEATTIE, J. A. and BLAISDELL, B. E. Proc. Am. Acad. Arts Sci. 71: 361. 1937.
3. BLAISDELL, B. E. and KAYE, J. *In* Temperature, its measurement and control in science and industry. 1941. Reinhold Publishing Corporation, New York. p. 127.
4. HOGE, H. J. *In* Temperature, its measurement and control in science and industry. 1941. Reinhold Publishing Corporation, New York. p. 141.
5. HOGE, H. J. Private communication.
6. HOGE, H. J. Rev. Sci. Instruments, 21: 815. 1950.
7. HOGE, H. J. and BRICKWEDDE, F. G. J. Research Nat. Bur. Standards, 22: 351. 1939.
8. HOGE, H. J. and BRICKWEDDE, F. G. J. Research Nat. Bur. Standards, 28: 217. 1942.
9. MEYERS, C. H. J. Research Nat. Bur. Standards, 9: 807. 1932.
10. MORRISON, J. A. and LOS, J. M. Faraday Soc. Discussions (No. 8): 321. 1950.
11. SCOTT, R. B. J. Research Nat. Bur. Standards, 25: 459. 1940.
12. STIMSON, H. F. J. Research Nat. Bur. Standards, 42: 209. 1949.
13. STULL, D. R. Chem. Eng. News, 27: 2772. 1949.
14. TAYLOR, H. S. and DIAMOND, H. J. Am. Chem. Soc. 57: 1251. 1935.
15. WOOLLEY, H. W., SCOTT, R. B., and BRICKWEDDE, F. G. J. Research Nat. Bur. Standards, 41: 379. 1948.

# THE RAMAN SPECTRUM OF FLUORINE<sup>1</sup>

BY D. ANDRYCHUK

## Abstract

The rotational and vibrational Raman spectra of gaseous fluorine at 1 atm. pressure were obtained. From these spectra the constants of the molecule in the electronic ground state were determined to be:

$$B_0 = 0.8828 \text{ cm.}^{-1}$$

$$r_0 = 1.417 \pm 0.001 \text{ \AA}$$

and

$$\Delta G_{\frac{1}{2}} = 891.8 \pm 0.4 \text{ cm.}^{-1}$$

The intensity alternation in the rotational spectrum shows that the nuclear spin of fluorine is  $\frac{1}{2} \frac{h}{2\pi}$  and that the  $F^{19}$  nuclei follow Fermi statistics.

## A. Introduction

Spectroscopic data for the determination of the molecular constants of fluorine in the electronic ground state are incomplete. The molecule does not exhibit an infrared absorption spectrum since it has no dipole moment (9). The emission spectrum observed by Gale and Monk (6) as well as by Aars (1) in an electric discharge through fluorine yields data about the electronically excited states  $^1\Pi$  and  $^1\Sigma$ . For these states the internuclear distance  $r_e$  was found to be 1.282 Å and 1.475 Å respectively, and the corresponding vibrational frequency  $\omega_e$  to be 1139.8  $\text{cm.}^{-1}$  and 977.4  $\text{cm.}^{-1}$ . Wartenberg, Sprenger, and Taylor (15) showed that the absorption spectrum of fluorine in the visible and near ultraviolet regions, unlike the absorption spectra of chlorine, bromine, and iodine, is entirely continuous and does not therefore lead to any information about the vibrational and rotational constants of fluorine in the ground state.

An approximate value of 1.435 Å for the internuclear distance in the ground state of fluorine was obtained by Rogers, Schomaker, and Stevenson (14) by means of the electron diffraction method. Using an earlier electron diffraction value of 1.46 Å obtained by Brockway (4) and applying Badger's rule (3) Murphy and Vance (12) estimated the vibrational frequency  $\omega_0$  of fluorine to be  $856 \pm 17 \text{ cm.}^{-1}$ .

The only direct spectroscopic method of determining these quantities would appear to be either a study of the Raman spectrum or a study of the absorption or emission spectrum in the far ultraviolet. Neither of these methods has been successfully applied until now. An unsuccessful attempt to observe the Raman spectrum has been described by Garner and Yost (7). Considerable improvements in light sources and in the speeds of photographic emulsions made it seem worth while to make a renewed attempt to observe the Raman spectrum of gaseous fluorine. As already mentioned in a preliminary note (2) the vibra-

<sup>1</sup> Manuscript received September 25, 1950.

Contribution from the Division of Physics, National Research Laboratories, Ottawa, Canada. Issued as N.R.C. No. 2338.

tional Raman spectrum of fluorine was indeed found and recently the rotational spectrum has been obtained and resolved. The present paper gives a more detailed report on this work.

### B. Experimental Procedure

The Raman tube was patterned after the design developed by Crawford and Welsh (5) at the University of Toronto. Fused quartz tubing was employed, since according to Leech (10) quartz is especially resistant to dry fluorine free from hydrogen fluoride. The Raman tube was  $1\frac{1}{2}$  in. in diameter and 39 in. long, and consisted of three sections as shown in Fig. 1. The front section *AB*, 8 in.

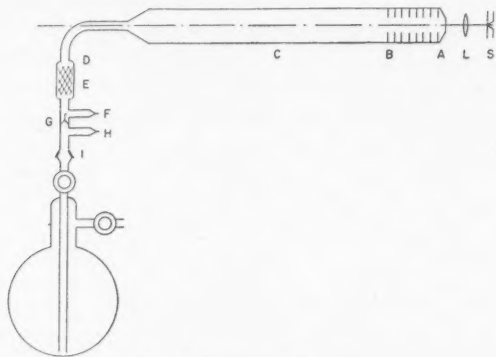


FIG. 1. A diagram of the apparatus.

long and painted black on the outside contained copper diaphragms which shielded the window of the Raman tube from direct light. These diaphragms were matched optically to the spectrograph by means of the lens *L*. The center section *BC* was the irradiated portion and was 14 in. long. The third section *CD*, 17 in. long and painted black on the outside, was the horn end of the Raman tube. A cell *E* containing dust free sodium fluoride pellets was fused to the horn end of the tube.

The tube was baked under vacuum to remove moisture from the walls and then sealed off from the vacuum systems at *F*. A three liter Florence flask containing the dry fluorine was attached to the Raman tube by means of the ground glass joint at *I*. The fluorine was stated to be 97% pure. The space *IG* was evacuated first, then sealed off at *H*. In order to fill the Raman tube with fluorine, the break-off seal at *G* was broken and the two stopcocks were opened. Any hydrogen fluoride which may have been present was removed from the fluorine as it passed over the sodium fluoride pellets at *E*. When the tube was filled the stopcocks were closed.

The ground glass joint and the stopcocks were made air tight with the aid of a fluoro-carbon grease. This method of handling the fluorine in the Raman tube prevented the clouding of the tube for as long as one week.

The light source consisted of two water-cooled mercury arc lamps of the type developed by Crawford and Welsh at the University of Toronto (5). A description of these lamps is given by Rank and Kagarise (13). The lamps were operated with a power input of 3 kw. Magnesium oxide coated reflectors were used with the lamps, since Menzies and Skinner (11) have shown that the use of this type of reflector greatly increased the light intensity.

A Zeiss three prism spectrograph was employed. An achromatic doublet lens having a focal length of 50.8 cm. and an aperture of  $F/10$  was adapted as the camera lens. The linear dispersion was  $58 \text{ cm.}^{-1}/\text{mm.}$  at  $4047 \text{ \AA}$ . The rotation and vibration spectra were photographed on Eastman Kodak 103a-0 plates. Two plates were obtained using a spectral slit width of  $1.2 \text{ cm.}^{-1}$  and an exposure of 24 hr. A third plate was obtained using a spectral slit width of  $0.8 \text{ cm.}^{-1}$  and an exposure of 48 hr.

The spectrum of an iron arc was photographed in juxtaposition with each Raman spectrum. The positions of the Raman lines and the calibration lines were read on a Hilger comparator to one thousandth of a millimeter.

For each plate the deviations of the comparison lines from a linear relationship between line position and wave number were plotted and the wave numbers of the rotational lines were determined with the aid of this correction curve. The values for the displacements from the exciting line given in Table I are the means of eight readings on each of three plates. Only the displacements of the alternate strong lines arising from the  $4047 \text{ \AA}$  mercury line were measured. The wave number shift of the vibrational Raman line was obtained from excitation by both the  $4047$  and the  $4358 \text{ \AA}$  mercury lines.

At the time that these exposures were taken, no arrangement had been made to place intensity calibration marks on the plates. However, after the measurements of the positions of the lines had been made it was felt that the weak lines in the rotational spectrum were sufficiently resolved and intense to justify an attempt at measuring their intensity relative to the strong lines. Therefore a step weakener was made and calibrated electronically at  $4047 \text{ \AA}$  with the aid of a monochromator. The step weakener was placed at the slit of the spectrograph and illuminated uniformly by means of a ground glass screen and a lamp. A 103a-0 plate of the same batch as used for the Raman spectrum was then exposed in the spectrograph for 24 hr. The calibration so obtained was used to determine the relative intensities of the rotational lines on the two plates. The densities of the spectra were measured on a Moll microphotometer adapted with a photo-multiplier cell and a Brown recorder.

### C. Results and Discussion

One of the rotational Raman spectra of  $F_2$  obtained in the way described above is reproduced in Fig. 2(a).

The following method was used to assign the correct  $J$  values to the rotational lines. The approximate formula given (see Herzberg (9)) for the rotational lines is

$$\Delta\nu = \pm 4B (J + 3/2).$$

The separation between successive lines is  $4B$ . In the present case the position of only every other line was measured so that the separation between the successive lines given in Column 2, Table I is  $8B$ . The observed value for this separation is approximately  $7.0 \text{ cm.}^{-1}$ . On the other hand the separation of

TABLE I  
DISPLACEMENTS AND INTENSITIES OF ROTATIONAL RAMAN LINES OF  $F_2$

$J$	$\Delta\nu$ (vac) observed ( $\text{cm.}^{-1}$ )	$\Delta\nu$ (vac) calculated ( $\text{cm.}^{-1}$ )	Relative intensity	Intensity ratio
23	86.36	86.11	5	2.5
22			3	
21	78.98	79.14	7	2.5
20			3	
19	72.13	72.15	7	2.4
18			3	
17	65.16	65.15	10	3.5
16			3	
15	58.17	58.14	11	2.6
14			6	
13	51.06	51.12	13	2.5
12			5	
11	44.10	44.09	12	3.3
10			3	
9	36.93	37.04	10	2.5
8			6	
7	28.89	30.00	12	2.1
5	-22.57	-22.95		
6				
7	-29.88	-30.00	35	2.2
8			16	
9	-36.93	-37.04	31	2.8
10			9	
11	-44.00	-44.09	19	3.4
12			4	
13	-51.07	-51.12	15	4.4
14			3	
15	-58.16	-58.14	16	4.3
16			5	
17	-65.18	-65.15	11	2.3
18			5	
19	-72.09	-72.15	10	2.8
20			3	
21	-79.12	-79.14	8	2.8
22			3	
23	-86.27	-86.11	7	2.9
24			2	
25	-93.35	-93.07	5	2.3
26				
27	-100.19	-100.00		
28				
29	-106.70	-106.92		
				Mean = 2.8

a Stokes line from the corresponding anti-Stokes line is  $2\Delta\nu = 8B(J + 3/2)$ . Therefore with the approximate  $8B$  value just determined the  $J$  value of any pair of corresponding lines can be determined. For example, from the two lines at  $\Delta\nu = +44.10$  and  $\Delta\nu = -44.00$  one obtains  $J + 3/2 = 88.10/7.0$



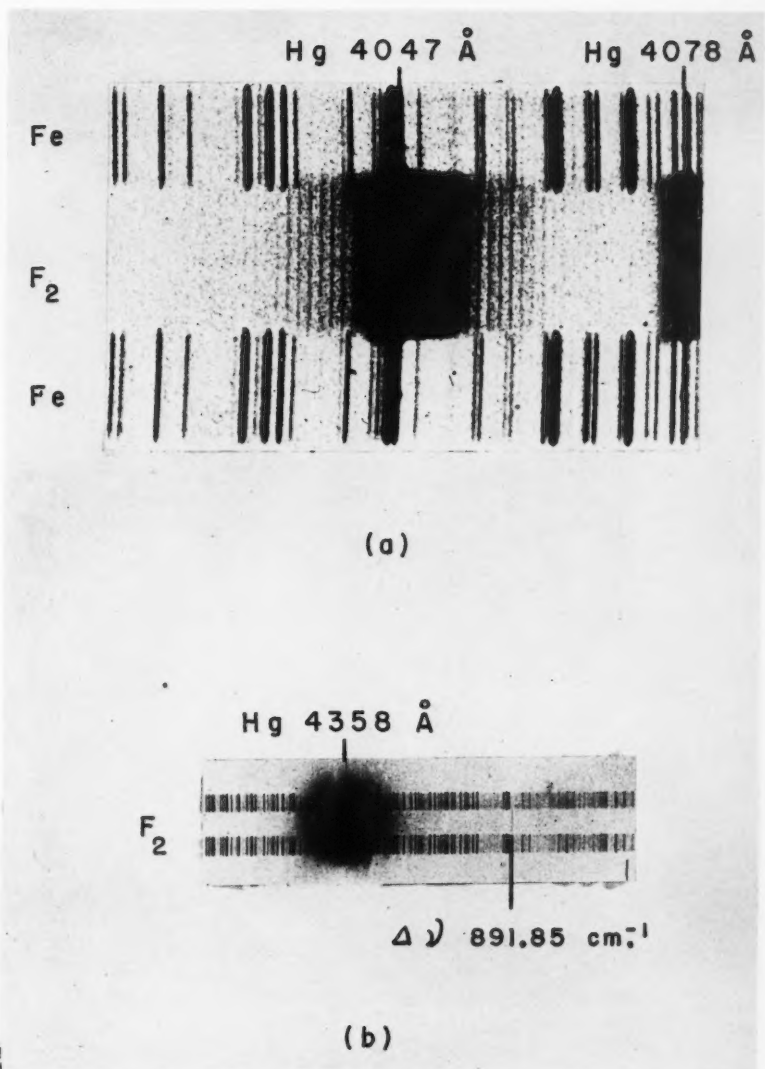
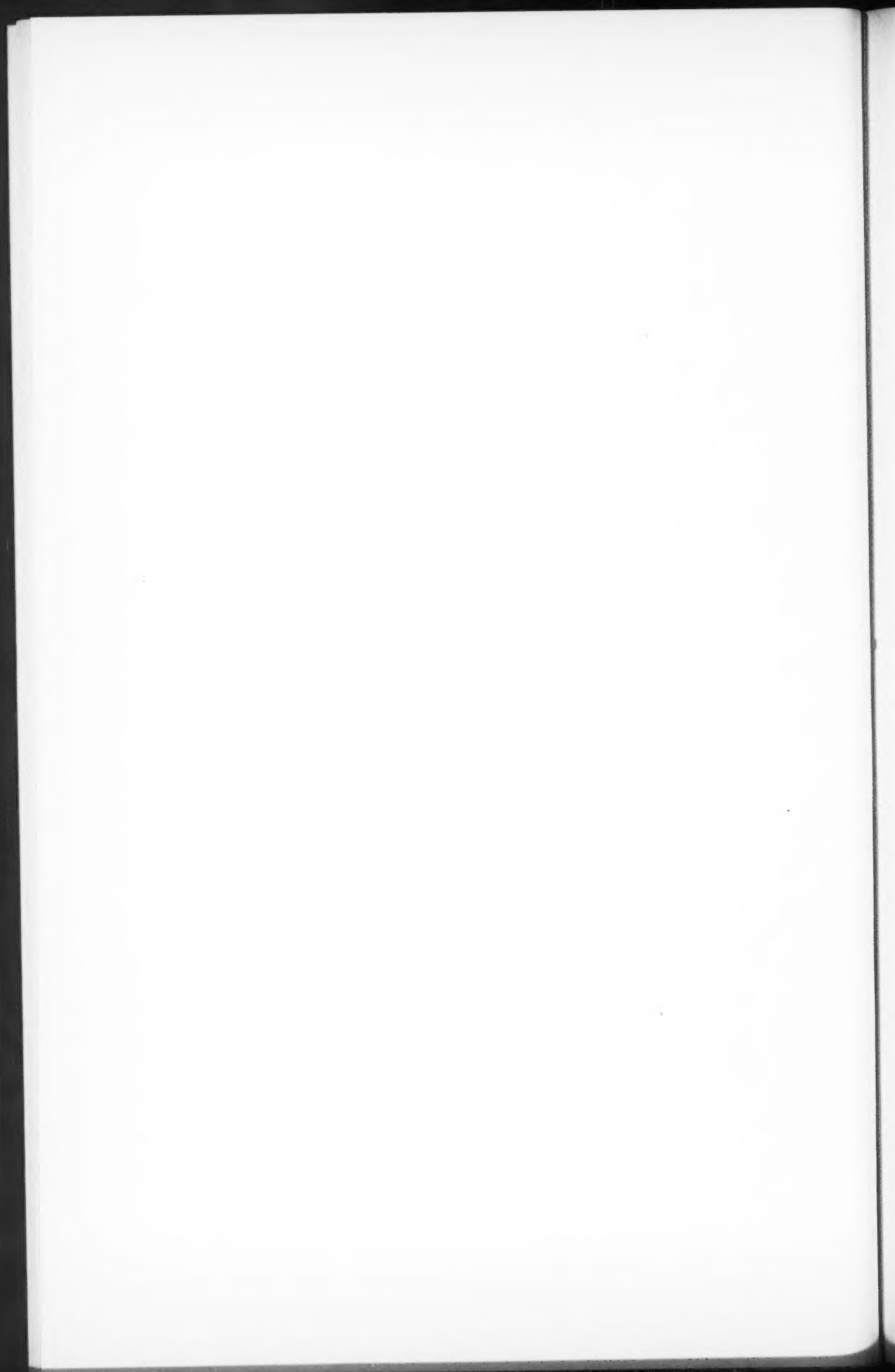


FIG. 2. *A print of the Raman spectrum of fluorine.*  
 (a) *The rotational spectrum arising from the Hg 4047 Å line.*  
 (b) *The vibrational line at 4535.7 Å arising from the Hg 4358 Å line.*



= 12.6, that is,  $J = 11$ . In this way the numbering of all the other lines is given (see Table I).

If the correction due to centrifugal stretching is included the formula for the displacements of the rotational Raman lines becomes (see, e.g., Herzberg (9))

$$\Delta\nu = \pm [(4B_0 - 6D_0)(J + 3/2) - 8D_0(J + 3/2)^3], \quad (1)$$

where approximately 
$$D_0 = \frac{4B_0^3}{\omega_0^2}. \quad (2)$$

Dividing Equation (1) by  $J + 3/2$  gives

$$\frac{\Delta\nu}{J + 3/2} = \pm [(4B_0 - 6D_0) - 8D_0(J + 3/2)^2]. \quad (3)$$

Therefore, plotting  $\frac{\Delta\nu}{J + 3/2}$  against  $(J + 3/2)^2$  should give a straight line whose slope is  $-8D_0$ . The experimental values of  $\frac{\Delta\nu}{J + 3/2}$  are plotted against  $(J + 3/2)^2$  in Fig. 3. Each value of  $\Delta\nu$  used is a mean of the displacements of the Stokes and the anti-Stokes lines of the same  $J$  value (Table I).

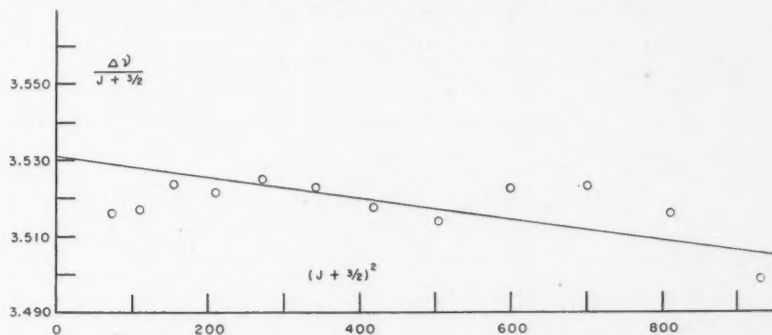


FIG. 3. A plot of  $\frac{\Delta\nu}{J + 3/2}$  against  $(J + 3/2)^2$ . The  $\Delta\nu$  used is a mean of the Stokes and the anti-Stokes lines given in Table I. The slope of the line was made equal to  $-8D = \frac{-8(4B^3)}{\omega^2}$ .

It is seen that the accuracy of the measurements is not sufficient to determine the slope of the straight line with any accuracy. It appeared preferable to employ the theoretical value of  $D_0$  from Equation (2) using preliminary values for  $B_0$  and  $\omega_0$  and determine that straight line of slope  $-8D_0 = -0.000027 \text{ cm.}^{-1}$  which fits best the experimental points. This line is shown in Fig. 3. The equation of this line is

$$\frac{\Delta\nu}{J + 3/2} = 3.5310 - 0.000027 (J + 3/2)^2 \quad (5)$$

The values of  $\Delta\nu$  calculated by this equation are given in Table I, Column 3.

According to Equation (3) the intercept of this line with the ordinate axis gives  $4B_0 - 6D_0$ . Since  $6D_0 = 0.000020$  this yields

$$B_0 = 0.8828 \pm 0.0010 \text{ cm.}^{-1}$$

Using the fundamental constants adopted by Herzberg (9) and  $\mu = 9.50227$  one finds

$$r_0 = 1.417_7 \pm 0.001_5 \text{ \AA.}$$

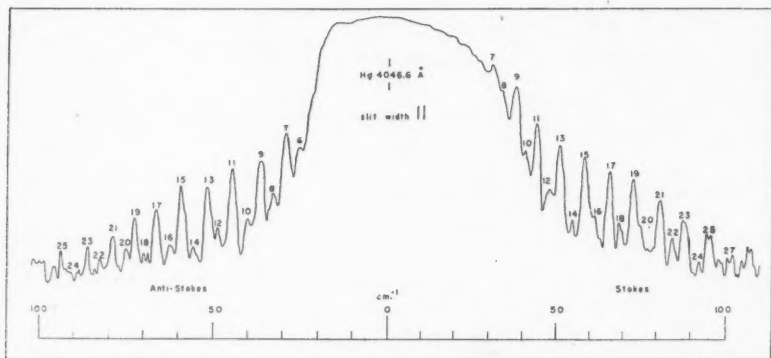


FIG. 4. A microphotometer trace of the rotational Raman lines of fluorine. The numbers on the maxima are  $J$  values.

Fig. 4 shows a microphotometer trace of the rotational Raman spectrum of fluorine. The relative values of the intensities of the lines are given in Table I, Column 4, and the ratio of the intensity of a line of odd  $J$  to the mean of the intensities of two neighboring lines of even  $J$  is given in Column 5. Owing to the rough nature of the intensity measurements the observed intensity ratio varies from 2.1 to 4.4 with a mean of 2.8. This value is in satisfactory agreement with the theoretical value of 3.0 for nuclei of spin  $\frac{1}{2} \frac{h}{2\pi}$ . Gale and Monk

(6) as well as Aars (1) obtained values for the intensity ratio which varied from 3 : 1 to 5.5 : 1. Since they were observing the emission spectrum of fluorine, perturbations between the different excited electronic states may have been present. Nevertheless since 3 : 1 is the theoretical maximum value of this ratio, they accepted the value for the nuclear spin as  $\frac{1}{2} \frac{h}{2\pi}$ . Recently Gilliam, Edwards, and Gordy (8) observed by means of microwave spectroscopy that the nuclear spin of  $F^{19}$  is  $\frac{1}{2} \frac{h}{2\pi}$ . The evidence from the Raman spectrum is in agreement with this result.

However, until now the statistics of the  $F^{19}$  nuclei had not been determined. From the fact that the odd numbered Raman lines are the strong ones and on the assumption (which can hardly be doubted) that the ground state of the  $F_2$

molecule is a  $^1\Sigma_g^+$  state it must be concluded that the  $F^{19}$  nuclei follow Fermi statistics. This experimental result is in agreement with the general rule that nuclei of odd mass number follow Fermi statistics.

A spectrogram showing the vibrational Raman line is reproduced in Fig. 2(b). In the present experimental arrangement the linear dispersion on the plate was  $4\frac{1}{2}$  times higher than in the arrangement used when the line was first observed (2). This resulted in much higher accuracy. The value of the displacement of the vibrational line is now found to be

$$\Delta\nu = 891.8_s \pm 0.4 \text{ cm.}^{-1}$$

and compares well with the value

$$\Delta\nu = 892.1 \pm 2 \text{ cm.}^{-1}$$

previously reported (2). The first vibrational quantum of  $F_2$  in its ground state is therefore

$$\Delta G_1 = 891.8_s \pm 0.4 \text{ cm.}^{-1}$$

Since Murphy and Vance (12) applied Badger's rule (3) to estimate the vibrational frequency, it is interesting to ascertain how well the rule holds when the new values for the internuclear distance and vibrational frequency are used. The rule is expressed by

$$k_e(r_e - d)^3 = 1.86 \times 10^5,$$

where  $k_e$  = equilibrium force constant in dynes per centimeter,

$r_e$  = equilibrium internuclear distance in Å,

$$d = 0.68 \text{ Å.}$$

Since the values for these two constants at equilibrium are not available at present, the values used are those obtained in the present experiment; that is

$$r_0 = 1.418 \text{ Å}$$

$$k_0 = 5.8883 \times 10^{-2} \mu \omega^2 \text{ dynes/cm.}$$

$$= 4.45 \times 10^5 \text{ dynes/cm.}$$

Substituting and solving for  $d$  gives  $d = 0.670 \text{ Å}$ , which agrees quite well with  $0.68 \text{ Å}$ , the value for  $d$  required by the rule.

### Acknowledgments

It is with pleasure I express my thanks to Dr. G. Herzberg for proposing the problem and for helpful suggestions. I also wish to thank Mr. J. W. Dale for providing the fluorine, and the technical staff of the Optics Section for their co-operation.

### References

1. AARS, J. Z. Physik. 79: 122. 1932.
2. ANDRYCHUK, D. J. Chem. Phys. 18: 233. 1950.
3. BADGER, R. M. J. Chem. Phys. 2: 128. 1934; 3: 710. 1935.
4. BROCKWAY, L. O. J. Am. Chem. Soc. 60: 1348. 1938.

5. CRAWFORD, M. F. and WELSH, H. L. Paper delivered by Prof. H. L. Welsh at the Montreal meeting of the Am. Phys. Soc. in 1947.
6. GALE, H. G. and MONK, G. S. *Astrophys. J.* 69: 77. 1929.
7. GARNER, C. S. and YOST, D. M. *J. Am. Chem. Soc.* 59: 2738. 1938.
8. GILLIAM, O. R., EDWARDS, H. D., and GORDY, W. *Phys. Rev.* 75: 1014. 1949.
9. HERZBERG, G. *In* Molecular spectra and molecular structure. I. Spectra of diatomic molecules. 2nd ed. D. Van Nostrand Company, Inc., New York. 1950.
10. LEECH, H. R. *Chem. Soc. London. "Quarterly Review"*, 3: 22. 1949.
11. MENZIES, A. C. and SKINNER, J. *J. Sci. Instruments*, 26: 299. 1949.
12. MURPHY, G. M. and VANCE, J. E. *J. Chem. Phys.* 7: 806. 1939.
13. RANK, D. H. and KAGARISE, R. E. *J. Optical Soc. Am.* 38: 279. 1948.
14. ROGERS, M. T., SCHOMAKER, V., and STEVENSON, D. P. *J. Am. Chem. Soc.* 63: 2610. 1941.
15. WARTENBERG, H. V., SPRENGER, G., and TAYLOR, J. *Z. physik. Chem. Bodenstein-Festb.* 61. 1931.

# EFFECT OF VARIABLE MASS OF THE ELECTRON ON THE SPACE-CHARGE LIMITED CURRENT IN A DIODE<sup>1</sup>

BY S. VISVANATHAN

## Abstract

The change in the current-potential distribution due to the relativistic variation of the mass of the electron has been calculated by suitable series expansions in the case of a plane parallel diode and has been shown to be considerable in the case of large power tubes.

## Introduction

The space-charge limited current between the electrodes varies as  $V^{3/2}/d^2$  (neglecting initial velocities), where  $V$  represents the potential difference and  $d$  the distance between the anode and the cathode. Langmuir (2) deduced by means of simple dimension theory that  $V^{3/2}$  dependence is independent of the geometry of the system. This conclusion has been widely quoted as the Three Halves Power Law. Experimentally, Chaffee has studied the current-potential characteristics of various three-element vacuum tubes, connecting the grid and plate together in order to obtain a diode system of complicated geometry. He has shown that under space-charge limitation the current can always be represented as  $V^n$ , where  $n$  is near  $3/2$ , over a part of the characteristic, though in some cases the value of  $n$  must be changed in order to fit  $V^n$  to the experimental data. The deviation from the Three Halves Power Law can be due to various causes, the most important one being the effect of the variable mass of the electron at high potentials.

The current-potential characteristic as predicted by Child's law (1) does not take account of the change in the mass of the electron due to its increase in velocity as it traverses the interelectrode space. This change, though very small in ordinary vacuum tubes, may be considerable in large power tubes, where the potentials are high. We shall calculate the magnitude of the effect in the case of plane parallel diodes in this paper.

## Plane Parallel Diode

The motion of the electrons is governed by the equation

$$eE = e \frac{dV}{dx} = \frac{d}{dt} (mv) \quad (1)$$

or

$$\frac{dV}{dx} = \frac{m_0}{e} \frac{d}{dt} \left( \frac{v}{\sqrt{1 - v^2/c^2}} \right) \quad (2)$$

$$\frac{d^2V}{dx^2} = \frac{m_0}{ev} \frac{d^2}{dt^2} \left( \frac{v}{\sqrt{1 - v^2/c^2}} \right)$$

<sup>1</sup> Manuscript received September 29, 1950.

Contribution from the Cruft Laboratory, Harvard University, Cambridge, Mass., U.S.A.



The current  $I$  is given by  $\rho v$

$$\frac{d^2}{dt^2} \frac{v}{\sqrt{1 - v^2/c^2}} = \frac{4\pi I e}{m_0}. \quad (3)$$

This equation is to be integrated subject to the boundary conditions

$$x = v = a = 0 \text{ at } t = 0.$$

So

$$\frac{v}{\sqrt{1 - v^2/c^2}} = \frac{2\pi e I}{m_0} t^2 \quad (4)$$

and

$$x = c \int \frac{\left(\frac{2\pi e I}{cm_0}\right) t^2 dt}{\sqrt{1 + \frac{4\pi^2 e^2 I^2 t^4}{c^2 m_0^2}}}. \quad (5)$$

The integral can also be written as

$$x = c \sqrt{\frac{cm_0}{2\pi e I}} \int_0^y \frac{y^2 dy}{\sqrt[4]{1 + y^4}}, \quad (6)$$

where

$$y = \sqrt[4]{\frac{2\pi e I}{cm_0}} t.$$

The above integral can be evaluated in terms of a sum of algebraic functions and elliptic functions of the first, second, and third kinds. In order to get an idea of the effect and also for computational purposes we integrate by a suitable series expansion.

Assuming  $y^4 < 1$  (usually true), expanding the integrand by the Binomial theorem, and integrating term by term, we obtain

$$x = \frac{c}{3} \sqrt{\frac{cm_0}{2\pi e I}} y^3 \left\{ 1 - \frac{3}{14} y^4 + \frac{9}{88} y^8 \dots \right\}. \quad (7)$$

The above series converges sufficiently rapidly so that  $x$  can be computed for all values of  $y < 0.8$  to within three significant figures.

Now for  $0.8 < y < 1$ , letting  $y = (1 - z)^{1/4}$ , the integral becomes

$$x = c \sqrt{\frac{cm_0}{2\pi e I}} \int \frac{-dz}{\sqrt[4]{2} (1 - z)^{1/4} (1 - z/2)^{1/2}} + A,$$

where the constant  $A$  can be evaluated from the first series Equation (7).

Again expanding by the Binomial theorem and integrating term by term,

$$x = c \sqrt{\frac{cm_0}{2\pi eI}} \left\{ 0.22 - \frac{z}{\sqrt[4]{2}} \left( 1 + \frac{z}{4} + \dots \right) \right\}. \quad (8)$$

From this equation, the value of  $x$  for  $z = 1$  can be determined. For values of  $1 < y$ , the substitution  $y = (1 + z)^{1/4}$  leads to

$$x = c \sqrt{\frac{cm_0}{2\pi eI}} \left\{ 0.220 + \frac{z}{\sqrt[4]{2}} \left( 1 - \frac{z}{4} + \dots \right) \right\}, \quad (9)$$

which is quite good for computation of  $x$  at  $y = 1.1$ . When  $1.1 < y$ , the integrand can be expanded in decreasing powers of  $y$  and

$$x = c \sqrt{\frac{cm_0}{2\pi eI}} \left\{ 0.910 + y \left( 1 + \frac{1}{6y^4} + \dots \right) \right\}. \quad (10)$$

Thus we see for large values of  $y$ , it is clear that the electrons would move with uniform velocity. However, the range of  $y$  as governed by Equation (7) is accompanied by prohibitively high potentials for vacuum tube work.

Now to find the potential distribution throughout the space charge region, we apply the energy law:

$$V = \frac{m_0 c^2}{e} \left\{ \frac{1}{\sqrt{1 - v^2/c^2}} - 1 \right\}. \quad (11)$$

Writing (4) as

$$\frac{v}{c} = \frac{y}{\sqrt{1 + y^2}} \quad (12)$$

and as seen above, only small values of  $y$  are applicable in vacuum tubes. Hence keeping only the first two terms of (7) we may write

$$x = \frac{1}{3} \sqrt{\frac{c^3 m_0}{2\pi eI}} y^3 \left\{ 1 - \frac{3}{14} y^4 \right\}. \quad (13)$$

Expressing  $V$  in terms of  $y$  by

$$V = \frac{m_0 c^2}{e} [\sqrt{1 + y^2} - 1]$$

then expanding by the Binomial theorem and solving for  $y$ , keeping only the first two terms,

$$y = \sqrt{\frac{2eV}{m_0 c^2}}. \quad (14)$$

Now substituting (14) in (13) and solving for the current

$$I = \frac{\sqrt{2}}{9\pi} \sqrt{\frac{e}{m}} \frac{V^{3/2}}{x^2} \left[ 1 - \frac{6}{7} \frac{e^2 V^2}{m_0^2 c^4} \dots \right]. \quad (15)$$

This equation is the same as Child's law except for the term in the bracket which corrects for the mass variation.

In a specific case for  $V = 100$  kv., the deviation is 4% as calculated with the term  $\frac{6e^2 V^2}{7m_0^2 c^4}$ . It is also obvious that one can neglect the initial velocities of emission. A similar calculation in the case of a cylindrical diode is contemplated for a future date.

#### Acknowledgment

The author thanks Prof. E. L. Chaffee for reading the manuscript.

#### References

1. CHILD, C. D. Phys. Rev. 32: 492. 1911.
2. LANGMUIR, I. Phys. Rev. 21: 419. 1923.

## ON THE STATIC DIELECTRIC CONSTANT OF DIPOLAR SOLIDS<sup>1</sup>

By J. H. SIMPSON

### Abstract

An application of Fröhlich's general formula for the static dielectric constant is made to a material having a cubic arrangement of dipolar molecules, each of which has two equilibrium positions  $180^\circ$  apart and ordering forces of the short range type which tend to make nearest neighbors antiparallel. It is shown that such a model cannot lead to a sharp transition in dielectric constant unless changes in lattice dimensions occur. Qualitative comparison with certain experimental results is made.

### Introduction

Various discussions on the static dielectric constant of crystalline solids in which the molecules can rotate have been given in the literature. Thus Fröhlich (5) has calculated the dielectric constant for a ketone on the assumption that each dipole has two equilibrium positions and that the probability of transitions between these depends upon the applied field and upon dipolar interaction between neighbors. Frank (4) has used a similar two-position model but has assumed that the field acting upon a given dipole is proportional to the mean resolved moment within the crystal. He thus obtains a second order transition using the Bragg-Williams approximation. The purpose of the present paper is to give results of a calculation of static dielectric constant using a model of the same type, but assuming (i) that dipolar molecules are arranged in a cubic structure, and (ii) that the more important forces between neighboring molecules are of the short range type (nondipolar). The energy of a particular molecule as a result of the action of its neighbors is taken into account, using the first approximation of Bethe, so that the effect of local order upon the dielectric constant is considered.

### Applicability of the Model

The importance of short range forces in dielectric materials has been discussed by Smyth (9) who has pointed out that some crystalline solids, glasses, etc., show dielectric behavior which is evidently due to dipole orientation, the restriction of which is dependent upon molecular shape, packing in the lattice, and internal energy,—or, put in another way, the restriction of dipolar motion is due largely to short range forces between molecules. This restriction of motion will normally be such that each molecule will have several possible equilibrium positions which may, or may not, have the same energy. The number of such positions will depend on the crystal structure and molecular shape. However, for some materials of rather special crystal structure and molecular shape there

<sup>1</sup> Manuscript received October 6, 1950.

Contribution from the Division of Radio and Electrical Engineering, National Research Laboratories, Ottawa, Canada. Issued as N.R.C. No. 2344.

Based on Report L/T 215 of the British Electrical and Allied Industries Research Association (E.R.A.).

may exist two positions—having dipole directions differing by  $180^\circ$ —whose energies in the completely disordered state are approximately equal, and considerably lower than the energy corresponding to any other position of the molecule. A model based on this type of structure will be used in this paper. It will also be assumed that changes in permanent moment of the dipoles, electronic polarization, and lattice dimensions are very small over the temperature range considered. The model is admittedly a highly idealized one and there will probably be no materials conforming closely to all these requirements. However, for one or two special substances it may be possible to obtain reasonable agreement with experiment and the results should be qualitatively applicable to materials of different crystal structure.

### Formula for the Static Dielectric Constant

The method used in calculating the static dielectric constant is that given by Fröhlich (6, 7) and is a generalization of Kirkwood's method for dipolar liquids. In Fröhlich's method a spherical region inside the dielectric medium is considered, within which the dipoles are treated according to the rules of classical statistical mechanics. This spherical volume is large compared to a region just big enough to have the same dielectric properties as a macroscopic specimen. The region outside the sphere is treated macroscopically as a continuous medium.

The spherical region is then divided into unit cells, each of which makes the same contribution to the mean square moment of the sphere. The static dielectric constant  $\epsilon$  is given by

$$\epsilon - n^2 = \frac{3\epsilon}{2\epsilon + n^2} \frac{4\pi N_0}{3} \frac{\overline{\mathbf{m}(x)\mathbf{m}^*(x)}}{kT}, \quad (1)$$

where  $n$  is the optical refractive index,  $\mathbf{m}(x)$  is the electric moment of the unit cell for a given set  $(x)$  of displacements of its elementary charges,  $\mathbf{m}^*(x)$  is the average moment of a spherical region of volume  $V$  inside the macroscopic specimen if the set  $(x)$  of displacements of a unit cell at the center (leading to  $\mathbf{m}(x)$ ) is supposed to persist for a long time.  $\overline{\mathbf{m}(x)\mathbf{m}^*(x)}$  is the average value of  $\mathbf{m}(x)\mathbf{m}^*(x)$  over all possible displacements  $(x)$  of the unit cell and is given by

$$\int \mathbf{m}(x)\mathbf{m}^*(x)p(x)dx = \overline{\mathbf{m}(x)\mathbf{m}^*(x)},$$

where  $p(x)$  is the probability of finding the displacements  $(x)$ , on an average over all possible states of the surroundings outside the unit cell.  $N_0 = N/V$  is the number of unit cells per unit volume.

Formula (1) is based on the assumption that the electronic contributions  $n^2$  to  $\epsilon$  may be separated from those due to rigid dipoles, etc., and treated on a macroscopic basis. This requires that the high-frequency dielectric constant be not altered when the molecule is turned from one position to another, and further, that over the temperature range considered there be no change in lattice spacing of the material. The latter condition may be rather a stringent

one, since a transition occurs which, in practical cases, is almost certain to produce a change in crystal dimensions and may affect the electronic charge distribution considerably. This will be discussed further when the application of the model to actual materials is considered.

### Detailed Calculations of the Dielectric Constant

The type of material considered in this calculation is one in which dipoles that are nearest neighbors have opposite directions in their lowest energy state, so that at the absolute zero of temperature when the lattice is completely ordered, the part of the dielectric constant due to rigid dipoles is zero. As the temperature is increased, some of the dipoles turn from their position of lowest energy, and the numbers of each type changing orientation must be equal. It is thus possible to consider each set of dipoles as forming one constituent of a mixture or alloy in which the quantities of the two constituents are equal, and the problem of calculating the change of order with temperature is the same as that solved by Bethe (1). Use will therefore be made of his results.

As in Bethe's case the lattice positions are divided into two types, "a" and "b", and a dipole is right (*R*) in an "a" position if it points in, say, the  $\rightarrow$  direction, and wrong (*W*) if it points in the  $\leftarrow$  direction. The opposite is true for dipoles in the "b" positions. The interaction energy of a pair of *RR* neighbors or *WW* neighbors is zero, and a pair of *RW* neighbors has interaction energy  $V$ .

The ratio of the probabilities corresponding to the two configurations is the Boltzman factor  $x = \exp(-V/kT)$ . The factor  $\epsilon$  of Bethe's first approximation including long-distance order is now called  $\lambda$ , since the symbol  $\epsilon$  has already been used for the dielectric constant.

The sphere is now divided into unit cells which contain one dipole of each type, and the quantities of Equation (1) calculated. A picture of one cell and its immediate surroundings for the case in which each molecule has six nearest neighbors (simple cubic NaCl type) is shown in Fig. 1. The cell dipoles are *A* and *B*. When *A* is right (*A-R*) its moment is  $+\mu$ , and when wrong (*A-W*),  $-\mu$ . The reverse is true for *B*.

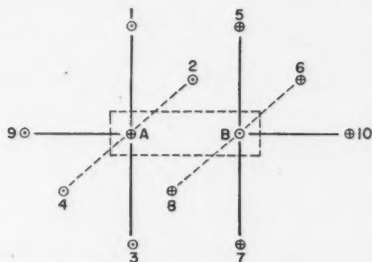


FIG. 1. Unit cell (enclosed by dotted line) and immediate surroundings in simple cubic (NaCl type)

The moments of the unit cell for the four possible configurations are shown in Table I.

TABLE I

Unit cell configuration	Unit cell moment	Probability of configuration
$A - R, B - R$	0	$p_{rr} = \frac{r}{1 + x\lambda}$
$A - R, B - W$	$2\mu$	$p_{rw} = \frac{x\lambda r}{1 + x\lambda}$
$A - W, B - R$	$-2\mu$	$p_{wr} = \frac{xw}{x + \lambda} = \frac{x\lambda r}{1 + x\lambda}$
$A - W, B - W$	0	$p_{ww} = \frac{\lambda w}{x + \lambda} = \frac{\lambda^2 r}{1 + x\lambda}$

The probability corresponding to the second configuration ( $A-R, B-W$ ) is the probability  $p_{rw}$  that a given (central) molecule is  $R$  and a certain one of its (first shell) neighbors is  $W$ . This is given by

$$p_{rw} = Cx\lambda \sum_{n=0}^{n=(z-1)} \binom{z-1}{n} x^n \lambda^n = Cx\lambda(1 + x\lambda)^{z-1} = \frac{x\lambda r}{1 + x\lambda},$$

where  $n$  is the number of  $W$  neighbors of the first shell (in addition to  $B$ ) for a certain configuration of that shell,  
 $z$  is the total number of nearest neighbors of  $A$ ,  
 $r$  is the total probability that a molecule is  $R$  and is equal to  $C(1 + x\lambda)^z$ ,  
 $C$  is a normalizing factor (see below).

The probability  $p_{wr}$  corresponding to the third configuration is similarly

$$p_{wr} = \frac{xw}{x + \lambda},$$

where  $w$  is the total probability that a molecule is  $W$  and is equal to

$$C(x + y)^z.$$

Since  $r + w = 1$ , 
$$C = \frac{1}{(1 + x\lambda)^2 + (x + \lambda)^2}$$

and since, from reference (1),  $\lambda = \left(\frac{x + \lambda}{1 + x\lambda}\right)^{z-1}$  it can be shown that  $p_{rw} = p_{wr}$  as should be expected, since, if the treatment is consistent, the same result should be obtained whether  $A$  or  $B$  is considered as the "central" molecule. The remaining two probabilities may be similarly determined and furnish a check that

$$p_{rr} + p_{rw} + p_{wr} + p_{ww} = 1.$$

There remains the problem of evaluating  $\mathbf{m}^*$  for each of the configurations, and here an approximation to the moment of the part of the sphere outside



the unit cell must be obtained. In doing this, care must be taken to treat equal numbers of "a" and "b" molecules by the same method. The following approximations will be considered:

1. Short range interaction between the unit cell and the remainder of the spherical region is neglected. Hence the moments of all molecules outside the unit cell are considered on a straight probability basis. The average moment of the "a" molecules outside the unit cell is, therefore,  $(N-1)(r-w)\mu$  since  $N$  is the number of unit cells in the spherical region. The average moment of the "b" molecules is similarly  $-(N-1)(r-w)\mu$ , so that the total moment of the spherical region is equal to that of the unit cell.

$$\text{Hence } \overline{\mathbf{mm}^*} = (2\mu)(2\mu) \frac{x\lambda r}{1+x\lambda} + (-2\mu)(-2\mu) \frac{x\lambda r}{1+x\lambda} = \frac{8\mu^2 x\lambda r}{1+x\lambda}. \quad (2)$$

2. Short range interaction between the unit cell and its immediate surroundings is taken into account so that the first layer of molecules outside the unit cell in Fig. 1 is included. The influence of the outer molecules on molecules 1, 2, 3, 4, 9 of this first layer is taken into account by the introduction of the  $\lambda$  factor for each wrong molecule of this group,—that is  $A$  is considered as the central atom in Bethe's method. The molecules 5, 6, 7, 8, 10, therefore, belong to Bethe's "second shell" around  $A$ . The factor  $\lambda$  cannot be introduced for these molecules and the effect of the outer layers on them cannot be considered by this method. The influence of this fact on the accuracy of the final result will be considered later.

A method which would undoubtedly be an improvement on that of this section would be one making use of Bethe's second approximation. The factor  $\lambda$  would then be introduced for molecules 5, 6, 7, 8, 10, and the remainder would form the central group. This method is considerably more complicated than the two described above, however, and will not be attempted in this paper. It is hoped that results of its application may be presented later.

Calculation of  $\overline{\mathbf{mm}^*}$  for the second approximation

(a) When  $A - R, B - W$ :

The group 1, 5 is first considered. The data for this group are shown in Table II.

TABLE II

Configuration	Probability	Moment
1 - R, 5 - R	$x$	0
1 - R, 5 - W	$x$	$-2\mu$
1 - W, 5 - R	$x^2\lambda$	$+2\mu$
1 - W, 5 - W	$x\lambda$	0

The average moment is, therefore,

$$\frac{-2\mu x + 2\mu x^2\lambda}{x(2 + \lambda + x^2\lambda)} = \frac{-2\mu(1 - x^2\lambda)}{2 + \lambda + x^2\lambda}. \quad (3)$$

There are four such pairs, and, since they are independent of each other and interact only with  $AB$ , their average moments may be added. For molecules 9 and 10 the average moments are

$$\frac{\mu x \lambda - \mu}{1 + x \lambda} = -\mu \left( \frac{1 - x \lambda}{1 + x \lambda} \right)$$

and

$$\frac{-\mu + \mu x}{1 + x} = -\mu \left( \frac{1 - x}{1 + x} \right) \text{ respectively.}$$

Hence

$$\overline{mm^*} p_{rw} = 2\mu \left[ 2\mu - \frac{8\mu(1 - x^2\lambda)}{(2 + \lambda + x^2\lambda)} - \mu \left( \frac{1 - x}{1 + x} \right) - \mu \left( \frac{1 - x\lambda}{1 + x\lambda} \right) \right] \frac{x\lambda r}{1 + x\lambda}$$

(b) When  $A - W$ ,  $B - R$ :

The average moments are calculated in exactly the same manner as in case (a) so that

$$\overline{mm^*} p_{rw} = -2\mu \left[ -2\mu - \frac{8\mu(x^2 - \lambda)}{(1 + 2\lambda + x^2)} - \mu \left( \frac{x - \lambda}{x + \lambda} \right) + \mu \left( \frac{1 - x}{1 + x} \right) \right] \frac{x\lambda r}{1 + x\lambda}$$

Since the remaining two configurations of  $A$  and  $B$  give zero moment for the unit cell, the over-all average  $\overline{mm^*}$  is given by:

$$\overline{mm^*} = 2\mu^2 \frac{x\lambda}{1 + x\lambda} \frac{1}{(1 + \lambda^{2/z-1})} \left[ 4 + \frac{8(x^2 - \lambda)}{(1 + 2\lambda + x^2)} - \frac{8(1 - x^2\lambda)}{(2 + \lambda + x^2\lambda)} + \left( \frac{x - \lambda}{x + \lambda} \right) - 2 \left( \frac{1 - x}{1 + x} \right) - \left( \frac{1 - x\lambda}{1 + x\lambda} \right) \right] \quad (4)$$

since

$$r = \frac{1}{1 + \lambda^{2/z-1}}$$

3. Another approximation is that of Bragg and Williams (2, 3) in which long range order only is considered. This treatment differs from those above in that the probability of a given configuration of the unit cell must now be considered as independent of the interaction between its elements. The probability of configurations  $A - R$ ,  $B - W$  and  $A - W$ ,  $B - R$  are, therefore, both equal to  $rw$ . Since the molecules outside the unit cell are also considered on a straight probability basis, their total moment is zero.

$$\text{Hence } \overline{mm^*} = 2\mu \cdot 2\mu rw + (-2\mu)(-2\mu)rw = 8\mu^2 rw = \frac{8\mu^2(1 - S^2)}{4}, \quad (5)$$

since  $r$  and  $w$  are now defined by  $r - w = S$ , where  $S$  is the long range order of Bragg and Williams. This quantity has been plotted accurately enough for the purpose of this paper by Nix and Shockley (8). It becomes zero at a transition temperature  $T_c = 1.216T_0$ , where  $T_0$  is the Bethe critical temperature at which long range order disappears.

The results for the three approximations may be summarized as follows:

$$\frac{(\epsilon - n^2)(2\epsilon + n^2)}{3\epsilon} = \frac{4\pi N_0}{3kT_0} \frac{T_0}{T} \overline{mm^*}, \quad (6)$$

where  $\overline{mm}^*$  has the following values for the simple cubic case:

$$\overline{mm}^* = \frac{8x\lambda\mu^2}{(1+x\lambda)(1+\lambda^{6/5})}$$

for the first approximation taking account of short range order.

$$\overline{mm}^* = \frac{8x\lambda\mu^2}{(1+x\lambda)(1+\lambda^{6/5})} \left[ 1 - \frac{2(x^2 - \lambda)}{(1+2\lambda+x^2)} - \frac{2(1-x^2\lambda)}{(2+\lambda+x^2\lambda)} \right. \\ \left. + \frac{(x-\lambda)}{4(x+\lambda)} - \frac{(1-x)}{2(1+x)} - \frac{(1-x\lambda)}{4(1+x\lambda)} \right]$$

for the second approximation taking account of short range order. (Note that this still refers to Bethe's first approximation but takes a more accurate account of the interaction between unit cell and the remainder of the spherical region.)

$$\overline{mm}^* = 2\mu^2(1 - S^2) \text{ for the Bragg-Williams case.}$$

### Limits of Error of the Approximation

Before discussing the results obtained with these approximations it is important to consider the directions and magnitudes of the errors involved. The probabilities used for the various configurations of the unit cell will be considered first. For the first two cases these are calculated directly from the results of Bethe's first approximation and suffer from the same limitations. These have been discussed elsewhere (8) and it is sufficient to point out here that the approximation is generally considered to be a reasonably accurate one. For the Bragg-Williams case the complete omission of short range order makes the error more serious and has the effect of raising the critical temperature by 22%.

The errors involved in the calculation of the moment  $\mathbf{m}^*$  of the whole sphere when  $A$  and  $B$  are fixed is now considered. Since interaction between molecules is assumed to make them unlike, the unit cell, for the case  $A - R, B - W$ , will tend to make 1, 2, 3, 4, 9,  $-R (= -\mu)$  and 5, 6, 7, 8, 10,  $-W (= -\mu)$ . In the first approximation this effect is neglected, so that when  $A - R, B - W$  the molecules 1, 2, 3, 4, 9 are less  $R$  (more positive) and the molecules 5, 6, 7, 8, 10 less  $W$  (also more positive) than they should be. Hence, since the moment of the unit cell is positive ( $= +2\mu$ ) in this case, the value of  $\overline{mm}^*p_{rw}$  is too large. Similar reasoning shows that when  $A - W, B - R (= -2\mu)$  the value used for  $\mathbf{m}^*$  is more negative than it should be so that  $\overline{mm}^*p_{wr}$  is again too large. We should, therefore, expect the first approximation to give a value of  $(T_0/T)\overline{mm}^*$  that is too large, and, since all interaction between the unit cell and its surroundings has been neglected, this error may be considerable. This same result refers also to the  $B - W$  approximation, since the method of calculating  $\mathbf{m}^*$  is the same.

For the second approximation the molecules 1, 2, 3, 4, 9 have been considered with an accuracy corresponding to that of Bethe's first approximation, so that

the influence of the outer molecules on them have been taken into account. For the molecules 5, 6, 7, 8, 10, however, the influence of the outer shells has been neglected. This influence will be in the same direction for all configurations of the unit cell, and if it were equally important for  $A - R$ ,  $B - W$  and for  $A - W$ ,  $B - R$  the net result on  $\overline{mm}^*$  would be zero. We should, however, expect that this influence will be more important when it is opposing the molecule  $B$  than when it is aiding, so that there is a slight net effect tending to increase  $m^*$  when  $A - R$ ,  $B - W$ ; i.e., tending to increase  $\overline{mm}^*$  (since  $m = +2\mu$  for  $A - R$ ,  $B - W$ ). This net effect has been neglected in the approximation, so that the value of  $\overline{mm}^*$  is smaller than it should be, although it is probably quite close to the true value. Thus, while the first approximation and the  $B - W$  methods both give results that are considerably above the true value, the second approximation gives one that is slightly below it.

### Results for the Simple Cubic (NaCl Type, $z = 6$ )

The curves of  $(T_0/T)\overline{mm}^*$  vs.  $T/T_0$  are plotted for the three cases in Fig. 2, and the second approximation using the Bethe factor is replotted to a larger scale in Fig. 3. These plots all show a discontinuity of slope (at  $T/T_0 = 1$  or

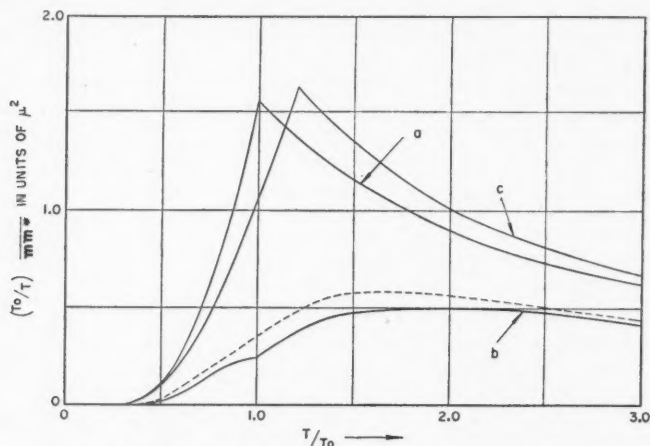


FIG. 2. Plot of  $\frac{(\epsilon - n^2)(2\epsilon + n^2)}{3\epsilon} \cdot \frac{3kT_0}{4\pi N_0\mu^2} = (T_0/T)\overline{mm}^*$  vs.  $(T/T_0)$  for simple cubic ( $z = 6$ ).

- (a) Bethe first approximation. Interaction of first outside layer with unit cell not considered.
- (b) Bethe first approximation. Interaction of first outside layer with unit cell included.
- (c) Bragg-Williams approximation.

$T/T_c = 1$ ) but for the most accurate approximation (Curve b) this is very slight. Furthermore, the change of slope at the transition temperature for b is in the opposite direction to those for a and c, and this may probably be taken

as confirmation of the fact that the approximations are on opposite sides of the true value. The position of the latter is perhaps very roughly similar to that shown dashed. It also seems probable that the true curve of  $(T_0/T)\underline{\text{mm}}^*$  (and hence of  $\frac{(\epsilon - n^2)(2\epsilon + n^2)}{3\epsilon}$ ) has no discontinuity at  $T/T_0 = 1$ . This is, of course, due to the fact that long range effects apply equally to the two types of dipole and, since for the model chosen these have opposite directions, they

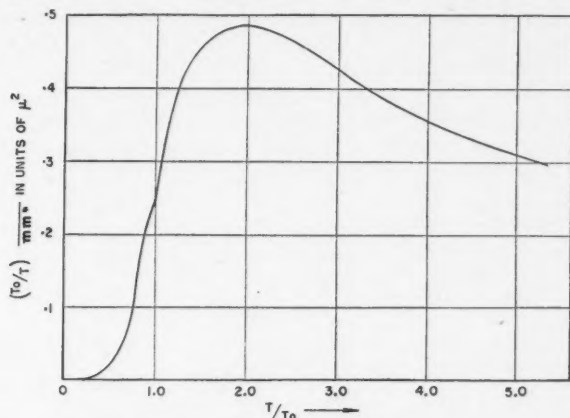


FIG. 3. Plot of Curve b of Fig. 2 to a different scale.

cancel each other and the net effect on the dielectric constant is zero. Thus, for this type of model (subject to the restrictions described in the second section above) there should be no sharp transition in the curve of dielectric constant. The presence of a sharp transition, as a result of an approximate calculation, merely indicates that part of the short range interaction has not been taken into account.

### Comparison with Experimental Results

The material 1, 2, 3-trimethyl-4, 5, 6-trichlorobenzene is a dielectric whose properties may probably be interpreted qualitatively in terms of the model of this paper. Accurate comparison is hardly justified since, in view of the shape of the molecule, one may question whether the crystal structure will be a simple cubic of the type here discussed and whether there will be only two equilibrium positions  $180^\circ$  apart. However it is reasonable to expect that the general forms of the calculated and experimental curves will be similar.

The curve obtained by White, Biggs, and Morgan (11) for the static dielectric constant of this material over a range of temperatures is shown in Fig. 4. These authors infer from the shape of the molecule that it rotates about one axis and, using a model proposed by White (10), assume that there are two

potential minima which differ in value and are  $72^\circ$  apart. They show that the curve of polarization calculated using this model fits reasonably well.

Using a reasonable value of  $n^2$ , the quantity  $\frac{(\epsilon - n^2)(2\epsilon + n^2)}{3\epsilon}$  can be readily determined from the curve of Fig. 4. It is proportional to the quantity plotted in Fig. 2 and by proper choice of  $T_0$  ( $-100^\circ\text{C.}$  approx.) the experimental data can be made to produce a curve which has the general form of Curve *b* of Fig. 2. Detailed comparison would probably be pointless however since, in addition

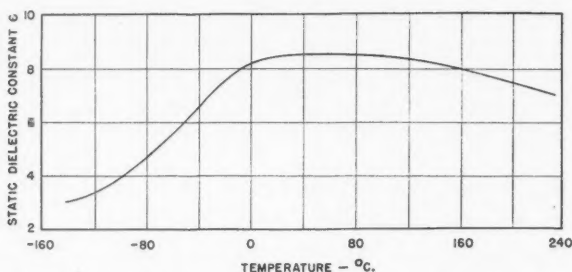


FIG. 4. Static dielectric constant (60 sec. charging time) of 1, 2, 3-trimethyl-4, 5, 6-trichlorobenzene as determined by White, Biggs, and Morgan (11).

to the factors mentioned above, neither the exact form of the true curve of  $\frac{(\epsilon - n^2)(2\epsilon + n^2)}{3\epsilon}$  (shown roughly by the dashed curve of Fig. 2), nor  $T_0$  is

known. It is possible that the latter could be determined by specific heat measurements. Such measurements would have to be quite accurate however, as the change in configurational specific heat at the transition temperature becomes a small fraction of the total specific heat for fairly large molecules of the type here considered. Further difficulties might arise if the rate of approach to the equilibrium state were very low.

The importance of this rate of approach to equilibrium should be especially emphasized. The order-disorder theory is based on statistical mechanical concepts which apply only if the system is in equilibrium. In many materials, even at temperatures near  $T_0$ , the establishment of equilibrium may require quite long periods of time. This is clearly brought out by measurements on 1, 2, 3-trimethyl-4, 5, 6-trichlorobenzene in the above-mentioned paper. From these it is apparent that, for temperatures below  $170^\circ\text{K.}$  (which, if this model applies, is approximately  $T_0$ ), even ballistic measurements of  $\epsilon$  using a charging time of 60 sec. may be in error. Relaxation times of the same order presumably apply to thermal measurements. If we make the usual assumption that the relaxation time is an exponential function of temperature the material may become essentially "frozen" at temperatures not very far below the transition temperature, and may not reach a very highly ordered state. This effect may

reduce the measured value of configurational specific heat considerably. In any event as much time as possible should be allowed for the material to reach equilibrium at low temperatures.

### Conclusions

From the comparison of the above theoretical results with experimental data we may draw some general conclusions concerning dielectric transitions in crystals whose structure is such that neighboring molecules tend to orient themselves with their dipoles in antiparallel directions. If a material of this type shows a sharp transition, it must be connected with an expansion of the lattice which allows a sudden increase in freedom of the dipoles (or of the whole molecule) with, usually, appreciable changes in electronic polarization. This expansion may be accompanied by a change to a completely different type of crystal structure with a different number of nearest neighbors to a given molecule. An accurate theoretical calculation of the variation in dielectric constant at a transition of this type can be made only if account can be taken of most of these factors, and practically every analysis therefore becomes a special case dealing with a specific material.

### Acknowledgments

The writer wishes to express his appreciation of the interest and guidance of Prof. H. Fröhlich who suggested this problem and to acknowledge his indebtedness to the British Electrical and Allied Industries Research Association for permission to publish this paper.

### References

1. BETHE, H. A. *Proc. Roy. Soc. (London)*, A, 150: 552. 1935.
2. BRAGG, W. L. and WILLIAMS, E. J. *Proc. Roy. Soc. (London)*, A, 145: 699. 1934.
3. BRAGG, W. L. and WILLIAMS, E. J. *Proc. Roy. Soc. (London)*, A, 151: 540. 1935.
4. FRANK, F. C. *Trans. Faraday Soc.* 42A: 24. 1946.
5. FRÖHLICH, H. *Proc. Roy. Soc. (London)*, A, 185: 399. 1946.
6. FRÖHLICH, H. *Trans. Faraday Soc.* 44: 238. 1948.
7. FRÖHLICH, H. *Theory of dielectrics*. The Clarendon Press, Oxford. 1949.
8. NIX, F. C. and SHOCKLEY, W. *Revs. Modern Phys.* 10: 1. 1938.
9. SMYTH, C. P. *Trans. Faraday Soc.* 42A: 175. 1946.
10. WHITE, A. H. *J. Chem. Phys.* 7: 58. 1939.
11. WHITE, A. H., BIGGS, B. S., and MORGAN, S. O. *J. Am. Chem. Soc.* 62: 16. 1940.



## ROTATIONAL ANALYSIS OF THE $\gamma$ BAND SYSTEM OF THE NS MOLECULE<sup>1</sup>

By P. B. ZEEMAN<sup>2</sup>

### Abstract

The band heads of the NS spectrum discovered in 1932 by Fowler and Bakker have been remeasured on plates taken on a large quartz spectrograph and on first order grating plates. The (0,0) and (0,1)  $\gamma$  bands have been photographed in the 6th, 8th, and 9th orders of a 21 ft. concave grating, and a rotational analysis of these bands has been carried out. For the ground state (<sup>2</sup>II) it was found that  $B'' = 0.7736$ ,  $\text{cm}^{-1}$ ,  $\alpha'' = 0.0061$ , and  $A = 223.03$ ,  $\text{cm}^{-1}$ . For the upper state the value  $B'_0 = 0.8267$  was obtained.

### Introduction

In 1932 Fowler and Bakker (2) discovered a new spectrum in a discharge through sulphur vapor containing nitrogen as an impurity. It consisted of two band systems bearing a striking resemblance to the  $\gamma$  and  $\beta$  systems of NO, both as regards structure and wave length. In view of experimental and theoretical considerations they attributed these bands to the NS molecule. Thus far no rotational analysis of these bands has been made, and it is the object of the present paper to submit such an analysis of the  $\gamma$  bands.

### Experimental

Since the NO and NS band spectra lie so nearly in the same spectral region it is essential to eliminate the NO bands completely from the light source in order to photograph the NS band systems successfully. Fowler and Bakker used commercial nitrogen, dried by passage over phosphorus pentoxide, and produced the NS bands by passing a gentle stream of this dried nitrogen through an ordinary end-on discharge tube while the sulphur reservoir was gently heated with a Bunsen flame. In the present research pure nitrogen prepared from pure  $\text{NaN}_3$  was used; and this gas was circulated at 2 mm. of mercury pressure through an ordinary end-on quartz discharge tube by means of a two-stage mercury diffusion pump. Sulphur was contained in a vertical reservoir attached to a side tube protruding horizontally from the capillary of the discharge tube. It was found essential to use vacuum distilled sulphur so as to eliminate CS bands which appeared on preliminary plates where ordinary flowers of sulphur were used. The partial pressure of the  $\text{S}_2$  in the discharge tube was adjusted until the second positive nitrogen bands and the visible  $\text{S}_2$  bands were of about equal intensity. This condition could be kept

<sup>1</sup> Manuscript received October 10, 1950.

<sup>2</sup> Merensky Institute for Physics, University of Stellenbosch, South Africa.

(The work described in the present paper was carried out by the writer as part of the research done toward the D.Sc. degree at the University of Stellenbosch. The manuscript was written while the writer was holding a postdoctorate fellowship at the National Research Council Laboratories, Ottawa, Ontario, Canada.)

constant for hours by means of a cylindrical electrical heater which surrounded the side tube.

Molybdenum electrodes were used instead of aluminum because the latter metal combined with nitrogen at higher temperatures causing the pressure in the tube to decrease unduly. The capillary of the discharge tube was 34 cm. long, and had an I.D. of 6 mm. with a wall thickness of 2 mm. A 3 k.v.a. transformer giving 6600 v. in the secondary circuit was used to pass the discharge through the tube. The primary current was kept constant at 18 amp., using a 220 v. supply.

It was found impossible to eliminate the persistent bands of NO completely from a discharge through N<sub>2</sub> alone even though this gas was circulated over heated copper turnings. However, when sulphur vapor was added the NO bands did disappear entirely. The final exposures were made on type I-O Eastman spectroscopic plates using the sixth, eighth, and ninth orders of a 21 ft. grating in a Paschen mounting. The exposure time was about 24 hr.

In order to photograph these high orders it was necessary to eliminate all wave lengths above about 2500 Å from the light entering the slit. This could not be done by means of a material filter, and the cylindrical lens method described by Herzberg and Curry (5) was employed. However, to eliminate completely the very strong N<sub>2</sub> and S<sub>2</sub> band systems it was found necessary to introduce an adjustable preliminary slit near the window of the discharge tube.

### Vibrational Analysis

The  $\gamma$  bands of NS originate from a  $B^2\Sigma^+ \rightarrow X^2\Pi$  transition quite similar to the  $\gamma$  bands of NO; they are degraded to the violet. The  $\beta$  bands of NS result from an  $A^2\Pi \rightarrow X^2\Pi$  transition, and are degraded to the red.

The heads of these bands have been remeasured on first order grating plates and plates taken on a large Hilger spectrograph. Essentially the same Deslandres diagrams as given by Fowler and Bakker were obtained with the new measurements. The heads of the  $\gamma$  bands can be represented by the following formulas:—

$$B^2\Sigma \rightarrow X^2\Pi_{3/2}: \nu_{head} = \begin{matrix} 43140.2 \\ 43162.4 \end{matrix} \left\{ - (1211.18\nu'' - 7.68\nu''^2) \right. \quad (1)$$

$$B^2\Sigma \rightarrow X^2\Pi_{1/2}: \nu_{head} = \begin{matrix} 43363.2 \\ 43383.9 \end{matrix} \left\{ - (1211.18\nu'' - 7.68\nu''^2) \right. \quad (2)$$

The heads of the  $\beta$  bands can be represented as follows:—

$$A^2\Pi_{3/2} \rightarrow X^2\Pi_{3/2}: \nu_{head} = 39697.6 + (935.60\nu' - 4.80\nu'^2) - (1211.25\nu'' - 7.35\nu''^2) \quad (3)$$

$$A^2\Pi_{1/2} \rightarrow X^2\Pi_{1/2}: \nu_{head} = 39882.4 + (953.35\nu' - 8.65\nu'^2) - (1211.25\nu'' - 7.35\nu''^2) \quad (4)$$

### Rotational Analysis

In Fig. 1 spectrograms of the (0, 1) and (0, 0)  $\gamma$  bands are reproduced. At some distance from the heads the branches were resolved into different series of lines which could be followed towards the heads by using constant second differences. By studying the relative intensities of these series of lines, the nature of the branches could be established. In the  ${}^2\Sigma^+ \rightarrow {}^2\Pi_{1/2}$  sub-bands the  $Q_1$  and  $R_1$  branches, and in the  ${}^2\Sigma^+ \rightarrow {}^2\Pi_{3/2}$  sub-bands the  $P_2$  and  $Q_2$  branches were found to be the strongest in both the bands analyzed. This is the same result as was obtained by Guillery (3) in the analysis of the NO bands. The (0, 1) band is much stronger than the (0, 0) band, and a higher degree of accuracy was obtained in the analysis of the former band. The plates were measured on an Abbé comparator, and the wave numbers computed by using the method described by Almy and Horsfall (1).

The  ${}^2\Pi$  ground state of NS is intermediate between case (a) and case (b) with a fairly large value for the coupling constant  $A$ . For such cases Hill and Van Vleck (6) have obtained the following formula for the spectral terms involved:—

$$T(J) = T_e + G + B_v \left\{ (J + \frac{1}{2})^2 - \Lambda^2 \pm \frac{1}{2} \left[ 4(J + \frac{1}{2})^2 - \frac{4A\Lambda^2}{B_v} + \frac{A^2\Lambda^2}{B_v^2} \right]^{\frac{1}{2}} \right\} + \phi_i(J). \quad (5)$$

For large  $A$  [case (a)] expansion of Equation (5) gives:—

$$T(J) = T_e + G \pm \frac{1}{2} A\Lambda + B_v \left\{ J(J+1) - (\Lambda \pm \frac{1}{2})^2 + \frac{1}{2} \pm [(J + \frac{1}{2})^2 - \Lambda^2] \frac{B_v}{A\Lambda} \right\} + \phi_i(J). \quad (6)$$

for regular doublet splitting with the + sign for the  $F_2$  component and the - sign for the  $F_1$  component of a  ${}^2\Pi$  state.

The formula for the rotational terms can be further simplified if we omit the terms independent of  $J$  and also introduce the "effective" value of  $B_v$  denoted by  $B_{v, eff}$ . (7), so that for doublet states

$$B_{v, eff}^{(2), (1)} = B_v \left( 1 \pm \frac{B_v}{A\Lambda} \right). \quad (7)$$

On substitution in Equation (6) and dropping the subscript  $v$ , the following formulas are obtained for the rotational terms of the two sub-levels of the  ${}^2\Pi$  state:—

$${}^2\Pi_{3/2}: F_2(J) = B_{eff}^{(2)} J(J+1) - D_{eff}^{(2)} J^2(J+1)^2. \quad (8)$$

$${}^2\Pi_{1/2}: F_1(J) = B_{eff}^{(1)} J(J+1) - D_{eff}^{(1)} J^2(J+1)^2. \quad (9)$$

In the present investigation of the  $\gamma$  bands no splitting in the upper  ${}^2\Sigma$  state was observed, and thus the expression

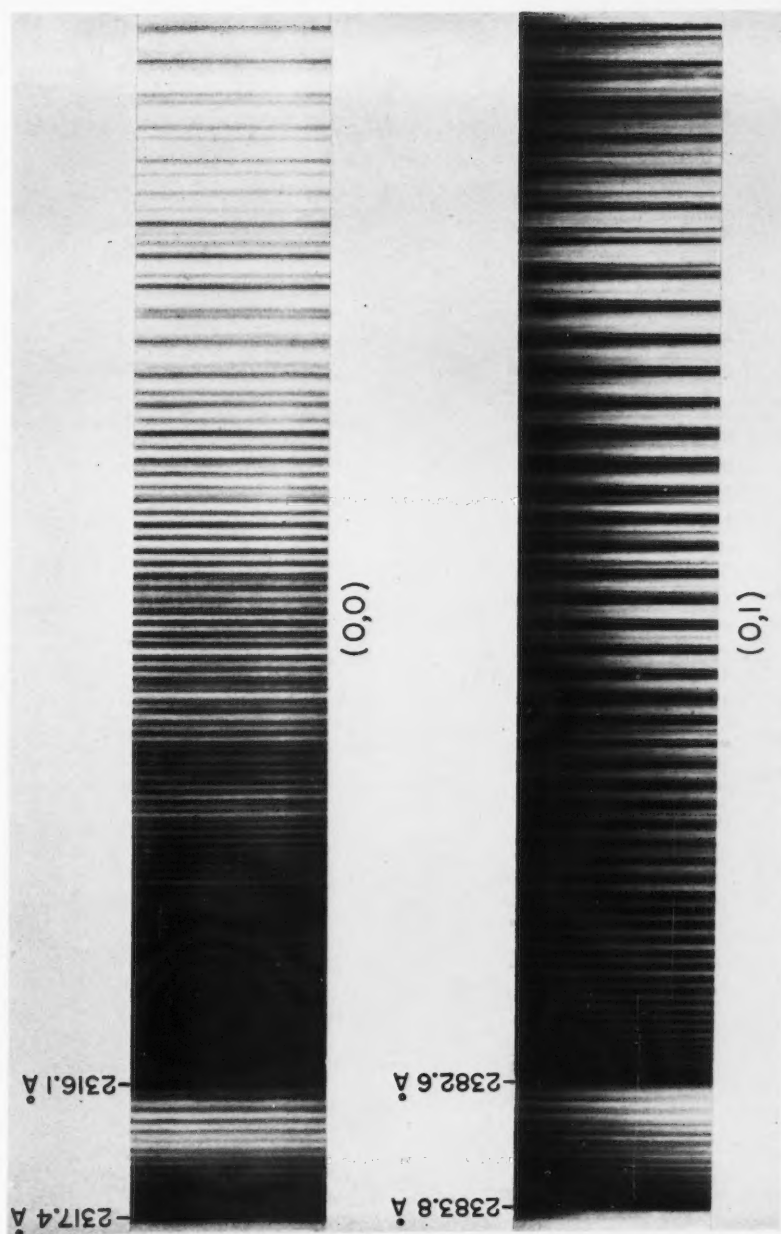
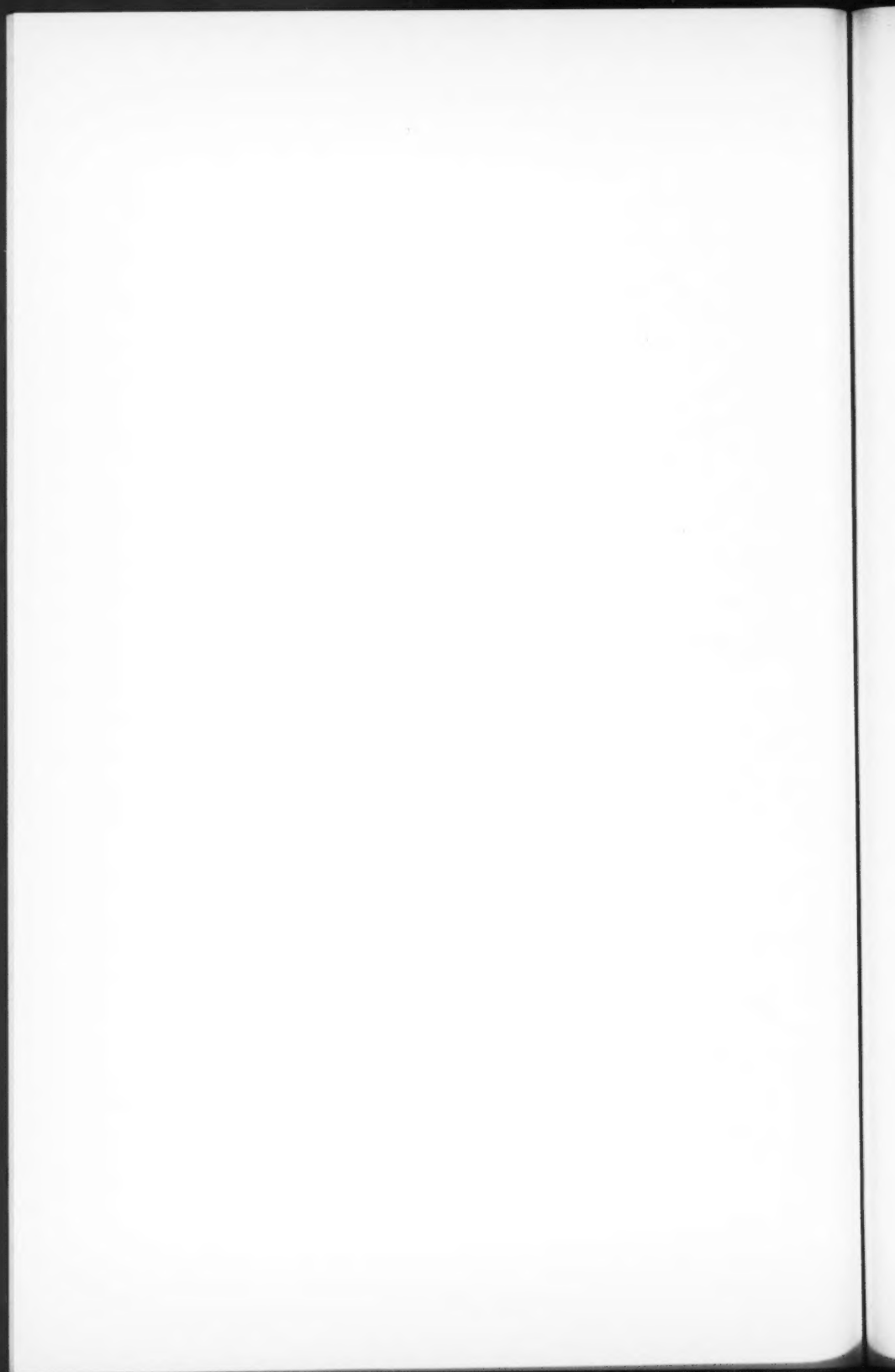


Fig. 1. Spectrograms of the  $B_{22} \rightarrow X_{III_{12}}$  components of the  $(0, 0)$  and  $(0, 1)$   $\gamma$  bands of NS taken in the eighth order of a 21 ft. concave grating in a Paschen mounting.



$$F(K) = B_r K(K+1) - D_r K^2(K+1)^2 \quad (10)$$

was sufficient for the rotational terms of this state. Hence omitting the term in  $D$  and the subscripts  $r$ , we have for the  $^2\Sigma$  state,

$$F_1(J) = B(J - \frac{1}{2})(J + \frac{1}{2}) \quad (11)$$

$$F_2(J) = B(J + \frac{1}{2})(J + 3/2).$$

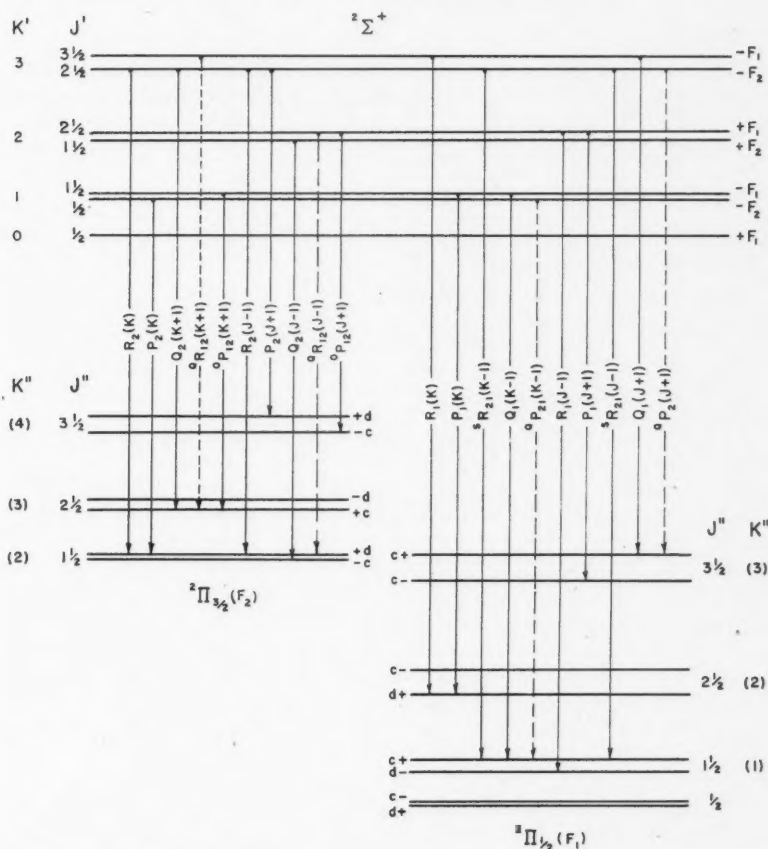


FIG. 2. Schematic energy level diagram for the first rotational lines of a  $^2\Sigma^+ \rightarrow ^2\Pi(a)$  band, showing the transitions for the determination of

$$\Delta_2 F_i'(K) \text{ and } \Delta_2 F_i''(J) \quad (i = 1 \text{ or } 2)$$

The broken lines represent the satellite branches for case (b). The branches  $SR_{21}$  and  $OP_{12}$  are forbidden in case (b).

The spin-doublet splitting in the lower state is much larger than shown, and the spin-doublet splitting in the upper state was not observed in the present case. The  $\Lambda$ -doubling splitting in the  $^2\Pi_{3/2}$  state is negligible in comparison with that in the  $^2\Pi_{1/2}$  state.

The designation of the extreme right-hand branch should be  $^0P_{21}(J+1)$  instead of  $^0P_2(J+1)$ .

According to Equations (8), (9), and (10) the expression for the term values involve  $J$  for  $^2\Pi$  states, and  $K$  for  $^2\Sigma$  states. However, the levels in a  $^2\Pi$  state can formally be numbered by  $K$  even for small  $J$  values. In this paper the combination relations dealing with the  $^2\Pi$  state are given in terms of  $J$  and those of the  $^2\Sigma$  state in terms of  $K$ . Hence to facilitate the evaluation of the combination differences and the rotational constants, the band lines were numbered in  $J$  as well as in  $K$ . An energy level diagram of a  $^2\Sigma^+ \rightarrow ^2\Pi$  transition is given in Fig. 2.

In Tables I and II the wave numbers of the band lines of the (0, 1) and (0, 0)  $\gamma$  bands are given. In Table III the combination differences of the upper states of the (0, 1) and (0, 0)  $\gamma$  bands are given. These quantities were determined from the following relations:—

$$\begin{aligned}\Delta_2 F'(K) &= R_2(K) - P_2(K) \\ &= Q_2(K+1) - {}^0P_{12}(K+1) \\ &= R_1(K) - P_1(K) \\ &= {}^S R_{21}(K-1) - Q_1(K-1).\end{aligned}\quad (12)$$

The combination differences for the lower states were obtained by using the following relations:—

$$\Delta_2 F''_2(J) = R_2(J-1) - P_2(J+1) = Q_2(J-1) - {}^0P_{12}(J+1) \quad (13)$$

and

$$\Delta_2 F''_1(J) = R_1(J-1) - P_1(J+1) = {}^S R_{21}(J-1) - Q_1(J+1). \quad (14)$$

Because of the  $\Lambda$ -type doubling that occurs for all states with  $\Lambda \neq 0$ , the lines of the  $P$  and  $R$  branches under these circumstances always end in somewhat different states from the lines of the  $Q$  branches. Hence the so-called "combination defect" occurs in the  $\Delta_1 F'(K)$  and  $\Delta_1 F''_i(J)$  values of, for example, a  $^2\Sigma \rightarrow ^2\Pi$  transition, so that these quantities cannot be used to determine the rotational constants accurately. However, the  $\Delta_1 F$  values were formed as shown below, in order to obtain an indication of the magnitude of the  $\Lambda$ -type doubling. A knowledge thereof enables us to decide whether the splitting of the  $^2\Pi$  state is normal or inverted. According to theory (4, p. 263) the  $\Lambda$ -type doubling for the  $^2\Pi_{3/2}$  sub-band is considerably smaller than that for the  $^2\Pi_{1/2}$  sub-band. In the present investigation, the combination defect was found to be of the order of the experimental error for the sub-bands with smaller wave numbers while it was considerably greater for the other sub-bands. This indicated that the spin-doublet splitting in the  $^2\Pi$  state is normal for NS. The following relations for example were used to evaluate the combination defect

$$\begin{aligned}\epsilon &= \Delta\nu_{dc}(J) + \Delta\nu_{dc}(J+1) \\ &= \{Q_2(J) - P_2(J+1)\} - \{R_2(J) - Q_2(J+1)\} \\ &\quad \text{for the } ^2\Sigma \rightarrow ^2\Pi_{3/2} \text{ sub-band}\end{aligned}\quad (15)$$

$$\begin{aligned}&= \{Q_1(J) - P_1(J+1)\} - \{R_1(J) - Q_1(J+1)\} \\ &\quad \text{for the } ^2\Sigma \rightarrow ^2\Pi_{1/2} \text{ sub-band.}\end{aligned}\quad (16)$$



TABLE I

WAVE NUMBERS OF THE LINES OF THE  ${}^2\Sigma^+ \rightarrow {}^2\Pi_{3/2}$  AND  ${}^2\Sigma^+ \rightarrow {}^2\Pi_{1/2}$  COMPONENTS OF THE (0, 1)  $\gamma$  BAND OF NS

$K''$	$J''$	${}^0P_{12}$	$P_2$	$Q_2$	$R_2$	$J''$	$P_1$	$Q_1$	$R_1$	$S_{R_{21}}$
1						1 $\frac{1}{2}$			42185.20	
2						2 $\frac{1}{2}$	42178.82		86.37	
3	2 $\frac{1}{2}$	41958.25	41960.13	41965.12		3 $\frac{1}{2}$	76.65	42181.92	87.81	
4	3 $\frac{1}{2}$	54.62	59.51	66.27	41974.40	4 $\frac{1}{2}$	74.39	81.37	89.32	
5	4 $\frac{1}{2}$	52.77	59.11	67.77	76.99	5 $\frac{1}{2}$	72.42	81.03	90.80	
6	5 $\frac{1}{2}$	50.81	59.05	69.25	80.88	6 $\frac{1}{2}$	70.98	80.85	92.60	
7	6 $\frac{1}{2}$	49.08	59.00	70.75	84.61	7 $\frac{1}{2}$	68.96	80.56	94.16	
8	7 $\frac{1}{2}$	47.48	59.05	72.67	87.66	8 $\frac{1}{2}$	67.77	80.85	96.08	
9	8 $\frac{1}{2}$	46.04	59.11	74.40	90.37	9 $\frac{1}{2}$	66.62	81.37	98.07	
10	9 $\frac{1}{2}$	44.79	59.51	76.13	94.23	10 $\frac{1}{2}$	65.63	81.92	42200.30	
11	10 $\frac{1}{2}$	43.50	59.95	78.14	97.21	11 $\frac{1}{2}$	64.68	82.78	02.65	
12	11 $\frac{1}{2}$	42.42	60.53	80.38	42001.85	12 $\frac{1}{2}$	63.75	83.54	05.02	42228.19
13	12 $\frac{1}{2}$	41.41	61.27	82.71	06.20	13 $\frac{1}{2}$	63.03	84.38	07.63	32.44
14	13 $\frac{1}{2}$	40.50	62.00	85.14	09.69	14 $\frac{1}{2}$	62.54	85.98	10.37	36.81
15	14 $\frac{1}{2}$	39.64	62.90	87.66	13.64	15 $\frac{1}{2}$	61.96	86.67	13.26	41.22
16	15 $\frac{1}{2}$	39.12	63.95	90.37	18.56	16 $\frac{1}{2}$	61.64	88.03	16.27	45.83
17	16 $\frac{1}{2}$	38.68	65.12	93.17	22.89	17 $\frac{1}{2}$	61.64	89.54	19.35	50.54
18	17 $\frac{1}{2}$	38.18	66.27	96.09	27.76	18 $\frac{1}{2}$	61.64	90.99	22.62	55.36
19	18 $\frac{1}{2}$	38.03	67.77	99.23	32.31	19 $\frac{1}{2}$	61.64	93.25	26.03	60.85
20	19 $\frac{1}{2}$	37.86	69.25	42002.18	36.97	20 $\frac{1}{2}$	61.80	94.59	29.41	65.76
21	20 $\frac{1}{2}$	37.86	70.75	05.60	41.42	21 $\frac{1}{2}$	61.96	96.60	33.32	71.48
22	21 $\frac{1}{2}$	38.03	72.67	08.93	46.95	22 $\frac{1}{2}$	62.54	98.79	36.81	76.52
23	22 $\frac{1}{2}$	38.18	74.40	12.55	52.24	23 $\frac{1}{2}$	63.03	42200.82	40.74	81.71
24	23 $\frac{1}{2}$	38.68	76.47	16.15	57.50	24 $\frac{1}{2}$	63.75	03.26	44.75	87.42
25	24 $\frac{1}{2}$	39.12	78.63	19.87	62.87	25 $\frac{1}{2}$	64.68	05.73	48.97	93.09
26	25 $\frac{1}{2}$	39.64	80.88	23.79	68.40	26 $\frac{1}{2}$	65.88	08.25	53.25	99.05
27	26 $\frac{1}{2}$	40.50	83.11	27.76	74.96	27 $\frac{1}{2}$	66.98	11.09	57.60	42305.24
28	27 $\frac{1}{2}$	41.08	85.64	31.75	79.73	28 $\frac{1}{2}$	67.95	13.91	61.96	11.37
29	28 $\frac{1}{2}$	41.99	88.18	36.08	85.67	29 $\frac{1}{2}$	69.39	16.87	66.65	17.56
30	29 $\frac{1}{2}$	43.10	90.82	40.46	91.67	30 $\frac{1}{2}$	70.98	20.07	71.48	24.07
31	30 $\frac{1}{2}$	44.37	93.73	44.89	97.77	31 $\frac{1}{2}$	72.78	23.30	76.52	30.41
32	31 $\frac{1}{2}$	45.61	96.60	49.52	42103.99	32 $\frac{1}{2}$	74.39	26.64	81.71	37.25
33	32 $\frac{1}{2}$	46.94	99.80	54.19	10.41	33 $\frac{1}{2}$	76.26	30.22	86.82	44.32
34	33 $\frac{1}{2}$	48.54	42002.96	58.99	16.79	34 $\frac{1}{2}$	78.38	33.98	92.08	51.06
35	34 $\frac{1}{2}$	50.22	06.20	63.94	23.34	35 $\frac{1}{2}$	80.56	37.71	97.54	58.00
36	35 $\frac{1}{2}$	52.04	09.69	68.96	29.99	36 $\frac{1}{2}$	82.19	41.47	42302.26	65.77
37	36 $\frac{1}{2}$	53.78	13.16	73.96	36.96	37 $\frac{1}{2}$	85.20	45.55	08.78	72.42
38	37 $\frac{1}{2}$	55.86	16.70	79.45	43.78	38 $\frac{1}{2}$	86.67	50.10	14.53	80.67
39	38 $\frac{1}{2}$	57.72	20.51	84.99	50.67	39 $\frac{1}{2}$	89.76	54.22	20.56	86.82
40	39 $\frac{1}{2}$	60.53	24.54	90.47	57.75	40 $\frac{1}{2}$	92.79	58.64	26.58	
41	40 $\frac{1}{2}$		28.51	96.45		41 $\frac{1}{2}$		63.11	32.90	
42	41 $\frac{1}{2}$		32.79	42102.07		42 $\frac{1}{2}$		67.96	39.07	
43	42 $\frac{1}{2}$		36.62	07.75		43 $\frac{1}{2}$		72.47	45.37	
44	43 $\frac{1}{2}$		41.42	13.69		44 $\frac{1}{2}$		77.24	51.97	
45	44 $\frac{1}{2}$		45.64	19.81		45 $\frac{1}{2}$		82.65	58.92	
46	45 $\frac{1}{2}$		50.62	26.02		46 $\frac{1}{2}$		87.88	65.77	
47	46 $\frac{1}{2}$		55.09	32.31		47 $\frac{1}{2}$		93.09	72.42	
48	47 $\frac{1}{2}$		60.07	38.81		48 $\frac{1}{2}$		98.41	79.47	
49	48 $\frac{1}{2}$		65.00	45.23		49 $\frac{1}{2}$		42304.15		
50	49 $\frac{1}{2}$		69.99	51.91		50 $\frac{1}{2}$		09.84		
			75.20	58.69		51 $\frac{1}{2}$		15.64		
						52 $\frac{1}{2}$		21.45		
						53 $\frac{1}{2}$		27.32		
						54 $\frac{1}{2}$		33.53		
						55 $\frac{1}{2}$		39.85		
						56 $\frac{1}{2}$		46.21		
						57 $\frac{1}{2}$		52.31		

TABLE II

WAVE NUMBERS OF THE LINES OF THE  $^2\Sigma^+ \rightarrow ^2\Pi_{3/2}$  AND  $^2\Sigma^+ \rightarrow ^2\Pi_{1/2}$  COMPONENTS OF THE (0, 0)  $\gamma$  BAND OF NS

$K''$	$J''$	$^0P_{12}$	$P_2$	$Q_2$	$R_2$	$J''$	$P_1$	$Q_1$	$R_1$	$S_{R_{21}}$
2	1 $\frac{1}{2}$					3 $\frac{1}{2}$	43379.60	43386.03	43391.70	43401.02
3	2 $\frac{1}{2}$		43165.48	43169.46		4 $\frac{1}{2}$	78.16	85.24	93.09	03.55
4	3 $\frac{1}{2}$		64.78	70.54		5 $\frac{1}{2}$	76.63	84.66	94.54	05.89
5	4 $\frac{1}{2}$	43157.28	63.73	72.04		6 $\frac{1}{2}$	74.75	84.54	96.06	09.47
6	5 $\frac{1}{2}$	55.43	63.32	73.74		7 $\frac{1}{2}$	72.81	84.05	97.63	12.63
7	6 $\frac{1}{2}$	53.72	63.32	75.33		8 $\frac{1}{2}$	71.45	84.54	99.58	15.43
8	7 $\frac{1}{2}$	51.65	63.32	77.03		9 $\frac{1}{2}$	70.50	85.24	43401.54	19.83
9	8 $\frac{1}{2}$	49.84	63.32	78.42	43194.87	10 $\frac{1}{2}$	69.21	85.50	03.55	23.65
10	9 $\frac{1}{2}$	48.05	63.32	79.72	98.25	11 $\frac{1}{2}$	67.98	86.03	05.89	27.10
11	10 $\frac{1}{2}$	46.77	63.32	81.70	43201.75	12 $\frac{1}{2}$	67.02	86.66	08.16	30.98
12	11 $\frac{1}{2}$	45.42	63.73	83.68	05.32	13 $\frac{1}{2}$	66.11	87.22	10.57	35.46
13	12 $\frac{1}{2}$	44.10	64.14	85.93	08.84	14 $\frac{1}{2}$	65.52	88.32	13.19	39.05
14	13 $\frac{1}{2}$	43.44	64.98	88.15	12.64	15 $\frac{1}{2}$	65.00	89.31	15.75	43.21
15	14 $\frac{1}{2}$	42.76	66.01	90.64	16.64	16 $\frac{1}{2}$	63.99	90.43	18.38	48.19
16	15 $\frac{1}{2}$	42.32	66.80	93.16	21.10	17 $\frac{1}{2}$	63.56	91.70	21.12	52.51
17	16 $\frac{1}{2}$	41.32	67.47	95.55	25.14	18 $\frac{1}{2}$	63.15	93.09	24.29	56.97
18	17 $\frac{1}{2}$	40.35	68.48	98.25	30.00	19 $\frac{1}{2}$	63.15	94.54	27.50	62.13
19	18 $\frac{1}{2}$	39.77	69.46	43201.12	34.08	20 $\frac{1}{2}$	63.15	96.06	30.98	66.73
20	19 $\frac{1}{2}$	39.37	70.54	03.78	38.77	21 $\frac{1}{2}$	63.15	97.63	34.21	72.02
21	20 $\frac{1}{2}$	39.37	72.04	06.99	43.00	22 $\frac{1}{2}$	63.56	99.58	37.87	77.04
22	21 $\frac{1}{2}$	39.37	73.74	10.29	48.10	23 $\frac{1}{2}$	63.99	43401.54	41.55	82.51
23	22 $\frac{1}{2}$	38.84	75.33	13.19	52.65	24 $\frac{1}{2}$	65.00	03.55	45.19	87.85
24	23 $\frac{1}{2}$	38.84	77.03	16.64	57.67	25 $\frac{1}{2}$	65.52	05.89	48.79	93.69
25	24 $\frac{1}{2}$	39.37	78.96	19.95	62.98	26 $\frac{1}{2}$	66.11	08.16	52.94	98.75
26	25 $\frac{1}{2}$	39.77	80.71	23.57	68.28	27 $\frac{1}{2}$	67.02	10.57	56.97	43504.12
27	26 $\frac{1}{2}$	39.77	82.78	27.20	73.42	28 $\frac{1}{2}$	67.98	13.19	61.25	10.35
28	27 $\frac{1}{2}$	40.35	84.85	30.97	79.02	29 $\frac{1}{2}$	68.71	15.88	65.43	16.33
29	28 $\frac{1}{2}$	40.91	86.99	34.93	84.52	30 $\frac{1}{2}$	69.84	18.76	69.89	22.17
30	29 $\frac{1}{2}$	41.32	89.17	38.77	89.95	31 $\frac{1}{2}$	71.45	21.64	74.49	28.44
31	30 $\frac{1}{2}$	42.32	92.04	43.00	95.97	32 $\frac{1}{2}$	72.31	24.29	78.92	34.72
32	31 $\frac{1}{2}$	43.44	94.19	47.19	43301.38	33 $\frac{1}{2}$	73.56	27.50	83.80	40.91
33	32 $\frac{1}{2}$	44.10	96.89	51.50	07.66	34 $\frac{1}{2}$	74.75	30.56	88.52	47.53
34	33 $\frac{1}{2}$	45.42	99.78	55.81	13.93	35 $\frac{1}{2}$	76.63	34.21	93.69	54.37
35	34 $\frac{1}{2}$	46.77	43202.59	60.31	19.80	36 $\frac{1}{2}$	78.77	37.87	98.75	60.89
36	35 $\frac{1}{2}$	48.05	05.64	64.91	25.83	37 $\frac{1}{2}$	81.24	41.55	43504.12	67.82
37	36 $\frac{1}{2}$	49.48	08.84	69.65	32.26	38 $\frac{1}{2}$	83.53	45.19	09.49	75.28
38	37 $\frac{1}{2}$	51.33	12.00	74.53	38.78	39 $\frac{1}{2}$		48.79	14.80	81.81
39	38 $\frac{1}{2}$		15.06	79.36	45.35	40 $\frac{1}{2}$		52.94	20.46	
40	39 $\frac{1}{2}$		18.51	84.20		41 $\frac{1}{2}$		56.97	26.42	
41	40 $\frac{1}{2}$		21.98	89.34		42 $\frac{1}{2}$		61.25	32.08	
42	41 $\frac{1}{2}$		25.42	95.11		43 $\frac{1}{2}$		65.43	37.60	
43	42 $\frac{1}{2}$		29.36	43300.13		44 $\frac{1}{2}$		68.87	42.94	
44	43 $\frac{1}{2}$		32.97	05.54		45 $\frac{1}{2}$		74.04	49.78	
45	44 $\frac{1}{2}$		36.71	11.09		46 $\frac{1}{2}$		78.92	56.25	
46	45 $\frac{1}{2}$		40.97	16.69		47 $\frac{1}{2}$		83.60	62.45	
47	46 $\frac{1}{2}$		45.22	22.29		48 $\frac{1}{2}$		88.52	69.93	
48	47 $\frac{1}{2}$		49.58	28.38		49 $\frac{1}{2}$			75.28	
49	48 $\frac{1}{2}$		53.78	34.23						
50	49 $\frac{1}{2}$		58.10	40.28						
51	50 $\frac{1}{2}$		62.35							
52	51 $\frac{1}{2}$		67.29							
53	52 $\frac{1}{2}$		72.09							
54	53 $\frac{1}{2}$		76.82							
55	54 $\frac{1}{2}$		81.50							
56	55 $\frac{1}{2}$		86.24							
57	56 $\frac{1}{2}$		91.82							
58	57 $\frac{1}{2}$		97.29							

TABLE III  
COMBINATION DIFFERENCES OF THE COMMON UPPER STATE OF THE (0, 1) AND (0, 0)  $\gamma$  BANDS OF NS

$K''$	(0, 1) Band				Average		(0, 0) Band				Average	
	$R_2(K) - P_2(K)$	$Q_2(K+1) - P_{12}(K+1)$	$R_1(K) - P_1(K)$	$S_{R_1(K-1) - Q_1(K-1)}$	$\Delta_2 F'(K)$	$\Delta_2 F(K)$	$R_2(K) - P_2(K)$	$Q_2(K+1) - P_{12}(K+1)$	$R_1(K) - P_1(K)$	$S_{R_1(K-1) - Q_1(K-1)}$	$\Delta_2 F'(K)$	$\Delta_2 F(K)$
4	14.89	15.00	14.93		14.94			14.76	14.93		18.32	14.85
5	17.88	18.44	18.38		18.23			17.31	17.91		21.33	17.85
6	21.83	21.67	21.62		21.71			21.61	21.31		21.23	21.38
7	25.61	25.19	25.20		25.33			25.38	23.82		24.93	25.04
8	28.61	28.37	28.31		28.43			28.57	28.13		28.89	28.59
9	31.25	31.34	31.44		31.34			31.66	31.04		30.89	31.29
10	34.72	34.65	34.68		34.68		31.55	34.93	34.33		34.59	34.70
11	37.25	37.96	37.97		37.73		38.43	38.26	37.91		38.14	38.19
12	41.33	41.30	41.27		41.30		41.60	41.83	41.41		41.07	41.41
13	44.93	44.64	44.60	44.65	44.71		44.71	44.71	44.46		44.32	44.55
14	47.69	48.02	47.84	48.07	47.91		47.67	47.88	47.83		47.87	47.87
15	50.74	51.25	51.30	50.84	51.03		50.64	50.83	50.75		50.72	50.75
16	54.61	54.49	54.48	54.56	54.53		54.30	54.23	54.38		53.90	54.20
17	57.77	57.91	57.71	57.80	57.80		57.67	57.40	57.56		57.76	57.72
18	61.49	61.20	60.99	61.00	61.17		61.52	61.35	61.14		60.80	61.20
19	64.55	64.50	64.39	64.37	64.45		64.63	64.40	64.34		63.86	64.38
20	67.72	67.73	67.61	67.60	67.67		68.23	67.62	67.83		67.60	67.82
21	70.67	70.90	71.36	71.17	71.04		70.97	70.92	71.06		70.67	70.91
22	74.29	74.37	74.28	74.45	74.45		74.36	74.35	74.32		74.39	74.36
23	77.83	77.47	77.71	77.74	77.69		77.32	77.81	77.56		77.46	77.55
24	81.03	80.75	81.00	80.89	80.92		80.64	80.58	80.19		80.97	80.61
25	84.25	84.15	84.10	84.16	84.18		84.02	83.80	83.27		84.30	83.84
26	87.52	87.26	87.38	87.36	87.37		87.57	87.43	86.83		87.80	87.40
27	91.85	90.67	90.62	90.80	91.00		90.64	90.63	89.95		90.59	90.45
28	94.00	94.09	94.02	94.16	94.08		94.17	94.02	93.27		93.56	93.77
29	97.49	97.37	97.26	97.46	97.40		97.54	97.45	96.71		97.16	97.23
30	100.85	100.53	100.50	100.69	100.65		100.78	100.68	100.05		100.45	100.50
31	104.04	103.91	103.75	104.00	103.92		103.92	103.75	103.04		103.40	103.54
32	107.39	107.25	107.32	107.11	107.28		107.19	107.40	106.61		106.80	106.99
33	110.61	110.55	110.45	110.61	110.55		110.77	110.39	110.24		110.42	110.45
34	113.83	113.72	113.71	113.85	114.11		114.15	114.54	113.77		113.41	113.95
35	117.14	116.92	116.98	117.08	117.04		117.21	116.86	117.05		116.97	117.01
36	120.29	120.17		120.29	120.25		120.18	120.18	119.98		120.16	120.11
37	123.59			124.30	123.90		123.41	123.21	122.88		123.02	123.11
38	127.08			126.87	126.98		126.78	125.95	125.95		126.27	126.32
39	130.17			130.57	130.37		130.28				130.09	130.19
40	133.21			133.60	133.41		133.58				133.02	133.30

These relations, as well as those already mentioned for the calculation of  $\Delta_2 F'(K)$  and  $\Delta_2 F_i''(J)$ , can easily be checked on the energy level diagram in Fig. 2.

To evaluate  $B_{eff.}$  for the various values of  $v$  for the lower state, use was made of the following method. By substituting the expressions (8) or (9) for  $F_i(J)$  we obtain

$$\begin{aligned}\Delta_2 F_i(J) &= F_i(J+1) - F_i(J-1) \\ &= 4B_{eff.}(J + \frac{1}{2}) - 8D_{eff.}(J + \frac{1}{2})^3.\end{aligned}\quad (17)$$

From Equation (17) it follows that if  $\frac{\Delta_2 F_i(J)}{(J + \frac{1}{2})}$  is plotted as a function of

$(J + \frac{1}{2})^2$ , a straight line is obtained. From the intercepts of these lines with the ordinate axis the values  $B_{eff.}^{(2)}$  and  $B_{eff.}^{(1)}$  can be obtained, and from the slope the corresponding  $D_{eff.}$  values. Finally  $B_v''$  is obtained by taking the mean value of  $B_{eff.}^{(2)}$  and  $B_{eff.}^{(1)}$  as is suggested by Equation (7).

The constants  $B_v'$  and  $D_v'$  can be obtained from the combination differences  $\Delta_2 F'(K)$  in a manner similar to that described for the  $^2\Pi$  state.

In this paper semifinal values of  $B_0'$  and  $B_1''$  were determined by this method, and the final values of  $D_0'$  and  $D_1''$ . The determined value,  $D_1'' = 1.22 \times 10^{-6}$  cm.<sup>-1</sup>, agrees well with the expected value  $D_e = 1.23 \times 10^{-6}$  cm.<sup>-1</sup>, calculated from the formula  $D_e = \frac{4B_e^3}{\omega_e^2}$ , using the new  $\omega_e$  and  $B_e$  values. However, the accuracy of the data for the (0, 0) band is not high enough to determine a reliable  $B_e$  value.

Using the value of  $D_0'$  thus obtained, and an approximate value of  $B_0$ , denoted by  $\tilde{B}_0'$ , a graph of

$$\Delta_2 F'(K) + 8D_0'(K + \frac{1}{2})^3 - 4\tilde{B}_0'(K + \frac{1}{2}) \quad (18)$$

against  $K$  values was constructed to obtain an accurate value of  $B_0'$ .

In order to obtain the best possible values of  $B_1''$  and  $B_0''$ , the differences  $(B_0' - B_1'')$  and  $(B_0' - B_0'')$  were determined.

However, the ordinary relations (4, p. 186) cannot be used for a  $^2\Sigma \rightarrow ^2\Pi$  transition, because additional terms now appear in these formulas. Fortunately the differences  $(B_v' - B_v'')$  can still be obtained by an appropriate choice of branches as is indicated by the following theory.

From Equations (8), (9), and (11) it follows that for a  $^2\Sigma \rightarrow ^2\Pi$  transition of the present type,

$$\begin{aligned}Q_1(J) &= \nu_0^{(1)} + B'(J - \frac{1}{2})(J + \frac{1}{2}) - B_{eff.}^{(1)} J(J+1) \\ Q_2(J) &= \nu_0^{(2)} + B'(J + \frac{1}{2})(J + \frac{3}{2}) - B_{eff.}^{(2)} J(J+1) \\ R_1(J) &= \nu_0^{(1)} + B'(J + \frac{1}{2})(J + \frac{3}{2}) - B_{eff.}^{(1)} J(J+1) \\ P_2(J) &= \nu_0^{(2)} + B'(J - \frac{1}{2})(J + \frac{1}{2}) - B_{eff.}^{(2)} J(J+1), \text{ etc.}\end{aligned}\quad (19)$$

Thus

$$Q_1(J) + Q_2(J) = \nu_0^{(1)} + \nu_0^{(2)} + \frac{B'}{2} + 2(B' - B'') J(J+1). \quad (20)$$

Hence by plotting  $Q_1(J) + Q_2(J)$  against  $J(J+1)$ , the quantities  $(B'_v - B''_v)$  and  $(\nu_0^{(1)} + \nu_0^{(2)})$  were determined for the (0, 0) and (0, 1) bands. However, to obtain  $B_{v,eff}^{(1)}$  and  $B_{v,eff}^{(2)}$  separately, as well as  $\nu_0^{(1)}$  and  $\nu_0^{(2)}$ , it is necessary to develop the following additional formulas.

From the above we have:—

$$R_1(J) - Q_2(J) = \nu_0^{(1)} - \nu_0^{(2)} + (B_{eff}^{(2)} - B_{eff}^{(1)})J(J+1). \quad (21)$$

Similarly it can be proved that

$$\left. \begin{aligned} R_1(J) - Q_2(J) &= Q_1(J) - P_2(J) \\ &= {}^S R_{21}(J) - R_2(J) \\ &= P_1(J) - {}^O P_{12}(J) \\ &= \nu_0^{(1)} - \nu_0^{(2)} + (B_{eff}^{(2)} - B_{eff}^{(1)})J(J+1) \end{aligned} \right\}. \quad (22)$$

Hence by plotting the average of the differences obtained from Equation (22) against  $J(J+1)$ , the quantities  $(\nu_0^{(1)} - \nu_0^{(2)})$  as well as  $(B_{eff}^{(2)} - B_{eff}^{(1)})$  were determined for the bands analyzed.

By means of the procedure explained above, the following values were finally obtained:—

$$B_1'' = 0.7644_7 \quad B_0'' = 0.7705_7 \quad \alpha_e'' = 0.0061_0$$

$$\begin{matrix} \nu_0^{(1)} - \nu_0^{(2)} = \Delta G_1^{(1)} = 1204.11 \text{ cm.}^{-1} \\ (0,0) \quad (0,1) \end{matrix}$$

and

$$\begin{matrix} \nu_0^{(2)} - \nu_0^{(2)} = \Delta G_1^{(2)} = 1204.17 \text{ cm.}^{-1} \\ (0,0) \quad (0,1). \end{matrix}$$

These values can be checked in the following way. For the same levels in the  $^2\Sigma$  (upper) state, it follows from the Equations (19) that

$$\begin{matrix} Q_1(J) - Q_1(J) = \nu_0^{(1)} - \nu_0^{(1)} - (B_{0,eff}^{(1)} - B_{1,eff}^{(1)})J(J+1) \\ (0,0) \quad (0,1) \quad (0,0) \quad (0,1) \end{matrix} \quad (23)$$

and

$$\begin{matrix} Q_2(J) - Q_2(J) = \nu_0^{(2)} - \nu_0^{(2)} - (B_{0,eff}^{(2)} - B_{1,eff}^{(2)})J(J+1) \\ (0,0) \quad (0,1) \quad (0,0) \quad (0,1) \end{matrix} \quad (24)$$

Hence by plotting  $Q_i(J) - Q_i(J)$  against  $J(J+1)$ ,  $\Delta G_1^{(1)}$ ,  $\Delta G_1^{(2)}$  and  $\alpha_e''$  can be obtained. The following values were determined in this way:—

$\Delta G_1^{(1)} = 1204.09 \text{ cm.}^{-1}$ ,  $\Delta G_1^{(2)} = 1204.20 \text{ cm.}^{-1}$ , and  $\alpha_e'' = 0.0061_3$ . These values agree well with those obtained by the method already described.

### Evaluation of the Coupling Constant $A$

From Equation (6) it follows that for  $\Lambda = 1$ , ( $^2\Pi$  state)

$$\begin{aligned} T_2(J) - T_1(J) &= \left( A - 2B_v - \frac{2B_v^2}{A} \right) + \frac{2B_v^2}{A} (J + \frac{1}{2})^2 \\ &= \left( A - 2B_v - \frac{3B_v^2}{2A} \right) + \frac{2B_v^2}{A} J(J + 1). \end{aligned} \quad (25)$$

The differences  $T_2(J) - T_1(J)$  in Equation (25) are identical with the quantities  $R_1(J) - Q_2(J)$ , etc., already mentioned above (Equation (22)). Hence by comparing Equations (25) and (22) we have:—

$$\nu_0^{(1)} - \nu_0^{(2)} = A - 2B_v - \frac{3B_v^2}{2A}. \quad (26)$$

In this way the coupling constant  $A$  was determined. As an example of this graphical determination of  $A$ , the graph for the (0, 1)  $\gamma$  band is given in Fig. 3.

In Table IV a summary of the rotational constants of the  $\gamma$  bands is given.

TABLE IV  
SUMMARY OF THE ROTATIONAL CONSTANTS OF THE  $\gamma$  BANDS OF NS

Band	$B_v'$ $\text{cm}^{-1}$	$D_v'$ $\times 10^{-6} \text{ cm}^{-1}$	$B_{eff}''^{(2)}$ $\text{cm}^{-1}$	$B_{eff}''^{(1)}$ $\text{cm}^{-1}$	$B_v''$ $\text{cm}^{-1}$	$D_v''$ $\times 10^{-6} \text{ cm}^{-1}$
(0, 0)	0.8267 <sub>0</sub>	0.77	0.7733 <sub>6</sub>	0.7677 <sub>7</sub>	0.7705 <sub>7</sub>	
(0, 1)	0.8267 <sub>0</sub>	0.77	0.7670 <sub>6</sub>	0.7618 <sub>7</sub>	0.7644 <sub>7</sub>	1.22

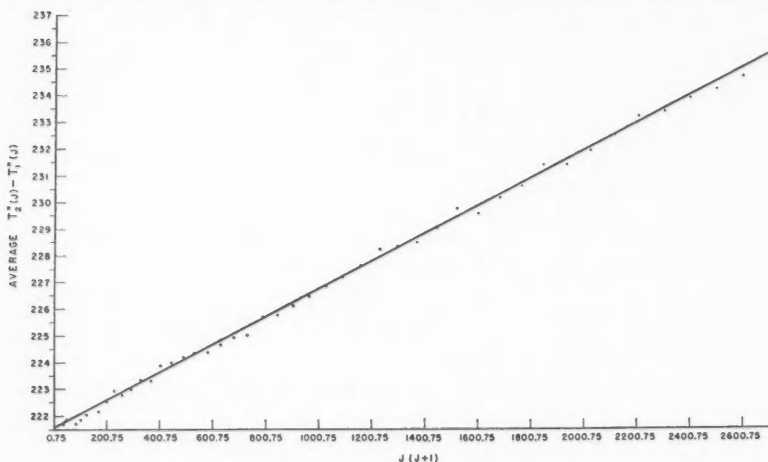


FIG. 3. Graph of  $T_2''(J) - T_1''(J)$  of the (0, 1)  $\gamma$  band of NS plotted against  $J(J + 1)$  to evaluate the coupling constant  $A$  as explained in the text.

For the ground state, we finally have the following constants\* for the NS molecule;

$$B_e = 0.7736_4 \text{ cm.}^{-1}$$

$$\alpha_e = 0.0061_2 \text{ cm.}^{-1}$$

$$r_e = 1.495_7 \times 10^{-8} \text{ cm.}$$

$$I_e = 36.17_1 \times 10^{-40} \text{ g. cm.}^2$$

Also, the following values were obtained for the constants listed below:—

$$\text{For the (0, 0) band: } \nu_0^{(1)} = 43387.35, \text{ and } \nu_0^{(2)} = 43165.88 \text{ cm.}^{-1}$$

$$\text{For the (0, 1) band: } \nu_0^{(1)} = 42183.24, \text{ and } \nu_0^{(2)} = 41961.71 \text{ cm.}^{-1}$$

$$\text{Average value of } \Delta G_1''^{(1)} = 1204.10 \text{ cm.}^{-1} \text{ and of } \Delta G_1''^{(2)} = 1204.19 \text{ cm.}^{-1}$$

$$\text{The coupling constant } A = 223.03 \text{ cm.}^{-1}$$

### Acknowledgments

The writer wishes to express his thanks to the South African Council for Scientific and Industrial Research for a grant in aid of the work done, and also to the Canadian National Research Council for the postdoctorate fellowship awarded.

The writer also wishes to thank Dr. G. Herzberg for suggesting the subject of the research, for continual interest and advice in the course of the work, and for reading and criticizing the manuscript.

### References

1. ALMY, G. and HORSFALL, R. Phys. Rev. 51: 492. 1937.
2. FOWLER, A. and BAKKER, C. Proc. Roy. Soc. (London), A, 136: 28. 1932.
3. GUILLERY, M. Z. Physik, 42: 121. 1927.
4. HERZBERG, G. Spectra of diatomic molecules (2nd Ed.). D. Van Nostrand Company, New York. 1950.
5. HERZBERG, G. and CURRY, J. Ann. Physik, 19: 800. 1934.
6. HILL, E. and VAN VLECK, J. Phys. Rev. 32: 250. 1928.
7. MULLIKEN, R. S. Rev. Mod. Phys. 2: 113. 1930.

\*All conversion factors were taken from "Spectra of Diatomic Molecules" (2nd edition) by G. Herzberg, D. Van Nostrand, New York, 1950.



AN ATTEMPT TO DETECT THE REACTION  $C^{14}(n, \gamma)C^{15}$ <sup>1</sup>

BY L. YAFFE AND W. H. STEVENS

## Abstract

A search has been made for the reaction  $C^{14}(n, \gamma)C^{15}$ . We have been unable to find any activity ascribable to  $C^{15}$ . If the  $\beta$ -ray energy of  $C^{15}$  is greater than 3 Mev. and the half life lies between 1 sec. and 1 min., the capture cross section for the above reaction is less than 1 microbarn.

## Introduction

The carbon isotopes found in nature have mass numbers 12 and 13. Carbon 10 and carbon 11 are short-lived positron emitters with half lives of 19 sec. and 20.5 min. respectively. On the neutron-excess side of the stability curve lies  $C^{14}$ , a long-lived negaton emitter with a half life variously estimated as between 5100 and 7200 years. Until recently no mention has been made in the literature of carbon of mass 15.

From the mass calculated by Bethe (1) for  $C^{15}$ —15.0165 amu—it can be seen that 10.8 Mev. difference exists between  $C^{15}$  and the stable end product  $N^{15}$  of mass 15.0049. Using the data assembled by Konopinski (5), one would expect roughly the following if all the energy were expended in a  $\beta^-$  transition: (a) if it were an allowed transition, the half life of  $C^{15}$  would be about 0.04 sec., (b) if first order forbidden, about 2 sec., (c) if second order forbidden, about 8 min. Using a recent value for the mass of  $C^{14}$  by Tollestrup, Fowler, and Lauritsen (8) of 14.007733 amu and the mass for  $C^{15}$  calculated by Bethe, one would expect that the  $(n, \gamma)$  reaction would occur with the release of about 0.2 Mev.

Recently, Hudspeth, Swann, and Heydenburg (3) have reported the production of  $C^{15}$  by the reaction  $C^{14}(d, p)C^{15}$ . They bombarded "normal" and active barium carbonate with deuterons from a Van de Graaff generator and obtained, by difference, a  $\beta^-$  emitter with a half life of 2.4 sec. and an energy of 8.8 Mev. which they ascribed to  $C^{15}$ . If the  $\beta^-$  transition is to the ground state of  $N^{15}$ , the mass of  $C^{15}$  should be 15.01434 amu. The reaction  $C^{14}(n, \gamma)C^{15}$  would then be exothermic by about 2 Mev., instead of 0.2 Mev.

Hudspeth *et al.* do not discuss chemical purification of the barium carbonate which was used in their experiment. Unless chemical identity was established between the active and inactive barium carbonate, the activity may have been due to an impurity in the active material, since the processing of the two materials was surely different.

In connection with a general program of determining cross sections of unstable nuclides and finding new nuclides, we have made a search for  $C^{15}$ . The

<sup>1</sup> Manuscript received in original form August 7, 1950, and, as revised, December 12, 1950. Contribution from the Chemistry Branch, Atomic Energy Project, National Research Council, Chalk River, Ontario. Issued as N.R.C. No. 2341.

nuclear reaction looked for was  $C^{14}(n, \gamma)C^{15}$  and the region of half lives investigated thus far has been 1 sec. to 1 min.

We have been unable to find any activity which might be ascribed to  $C^{15}$ . These results have previously been reported very briefly in a Letter to the Editor of the Physical Review (9).

## Experimental

### (a) Preparation of Material

The active carbon sample was received as a solution of sodium carbonate containing 6 atom %  $C^{14}$ . The carbon in both active and inactive sodium carbonate solutions was reduced to elemental carbon using the same technique and reagents. This assured the chemical identity of the two samples, which is a necessary prerequisite if the isotopic assignment is to be made without chemical purification after irradiation.

Barium carbonate was precipitated from the sodium carbonate solution, centrifuged, washed with water, then with acetone and gently dried. The barium carbonate was then mixed with lead chloride (2) and the mixture heated *in vacuo* to  $350^{\circ}\text{C}$ . where the lead carbonate which is formed in the dry reaction decomposes with evolution of carbon dioxide. The carbon dioxide was then frozen down and purified by repeated distillation.

The carbon dioxide was reduced to elemental carbon (6) in the following manner. The center of a 1 in. diameter iron pipe about 18 in. long was filled with a 10-fold excess of C.P. magnesium turnings. One end of this pipe was connected to the vacuum system. The other end was capped and the system was made air-tight using de Khotinsky cement and black wax. The reaction tube was evacuated to a pressure of  $10^{-4}$  mm. and the tube then filled to a pressure of 10 cm. with carbon dioxide. The center section of the pipe was heated to about  $650^{\circ}\text{C}$ ., the melting point of magnesium, at which temperature magnesium reacts with carbon dioxide, reducing it to carbon. The remainder of the carbon dioxide was converted to carbon by allowing successive small amounts of carbon dioxide into the pipe.

When the reaction was complete the solids were removed from the pipe and treated with water and hydrochloric acid, gradually increasing the hydrochloric acid concentration until it was 6 *N*. The carbon was leached for about one hour in this manner, then centrifuged. After a second treatment with 6 *N* hydrochloric acid for an hour it was centrifuged, washed with water, then acetone, and finally dried *in vacuo*.

### (b) Irradiation Procedure

Irradiation in the rapid action rabbit of the NRX pile requires the encasing of the sample in capsulelike containers. Since the half-life expected was short, in comparison with the time required to remove the sample from the capsule the activity of the irradiated material had to be measured in the capsule.

'Spec-pure' iron was chosen as suitable material for the capsule construction since the capture cross section of the iron is low and all resultant activities have reasonably long half lives. To ensure chemical identity, all capsules were fabricated from the same rod.

A special flask, as shown in Fig. 1, was used for receiving and immediately counting the sample. The flask was cylindrical and made of lead to provide adequate shielding. The sample in the capsule is drawn up above the positioning plunger *E* by suction applied at the valve *C*. *D* is a locating plunger

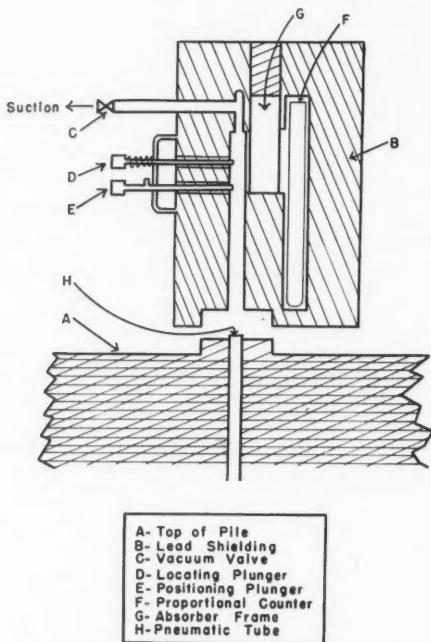


FIG. 1. Castle for receiving and counting samples.

which is normally held in position by a spring. When this plunger is depressed, its length of travel will indicate the presence or absence of the capsule. A proportional counter *F* with thin glass window (30 mgm. per cm.<sup>2</sup>) filled to a total pressure of 73 cm. at 20°C. with argon (67 cm.) and carbon dioxide (6 cm.) was placed in position as shown. When in position the capsule is directly opposite the thin window, with no intervening shielding. An absorber frame *G* is placed between counter and capsule so that the same apparatus may be used for obtaining absorption curves and determining the maximum energy of the  $\beta^-$  emitters found.

The entire assembly was placed over the pneumatic tube *H* which leads to a high flux position ( $6 \times 10^{13}$  neutrons per cm.<sup>2</sup> per sec.) in the pile.

The procedure followed was to have the capsule held above the positioning plunger by suction alone. When valve *C* was closed the capsule dropped to the bottom of tube *H*. After the desired irradiation, the capsule was again sucked up into counting position above *E* by reopening *C*.

(c) *Counter Assembly*

The counter assembly consisted of a preamplifier, linear amplifier, high voltage (3000 v.) set, scale of 1000, and an Esterline-Angus Recorder. The speed of motion of the paper on the recorder was determined using 60-cycle line frequency. Each division (0.75 in.) corresponded to 3.7 sec. at the speed used. This time interval could be further divided into smaller parts using dividers.

The linearity of the proportional counter assembly was checked and no losses greater than 1% were found up to a counting rate of 200,000 per minute.

(d) *Irradiations*

The various irradiations made are shown in Table I.

TABLE I  
IRRADIATION DATA

Results shown in	Material irradiated	Weight, gm.	Time of irradiation, sec.
Fig. 2	Fe block	Fe - 12.0	10
Fig. 3	Fe capsule + $C^{12} + C^{13} + \text{air}$	Fe - 8.5 $C^{12} + C^{13} - 0.021$	8
Fig. 4	Fe capsule + $C^{12} + C^{13} + C^{14} + \text{air}$	Fe - 8.5 $C^{12} + C^{13} - 0.021$ $C^{14} - 0.0013$	8
Fig. 5	Fe capsule + $\text{Li}_2\text{CO}_3 + \text{air}$	Fe - 8.5 $\text{Li}^7 - 1.2 \times 10^{-7}$	2

### Results

The results of the irradiations are shown in Figs. 2-5 incl. In Fig. 2, the decay curve obtained from the irradiation of a block of the 'spec-pure' iron used as capsule material is shown. At least three activities are present with half lives of  $4.4 \pm 0.2$  sec.,  $26.5 \pm 0.3$  sec., and  $12.9 \pm 0.1$  min. The limits shown are those of internal consistency. These activities are probably due to  $\text{Si}^{27}$ ,  $\text{O}^{19}$ , and a mixture of  $\text{Cu}^{62}$ ,  $\text{Mg}^{27}$ , and  $\text{Fe}^{53}$ . The first four are produced by ( $n, \gamma$ ) and ( $n, 2n$ ) reactions on impurities known to be present, the fifth by an ( $n, 2n$ ) reaction on  $\text{Fe}^{54}$ . The activities found on irradiation of the inactive

and active carbon samples are identical to those found in the iron itself, as shown in Figs. 3 and 4. No additional activity due to the introduction of  $C^{14}$  was found.

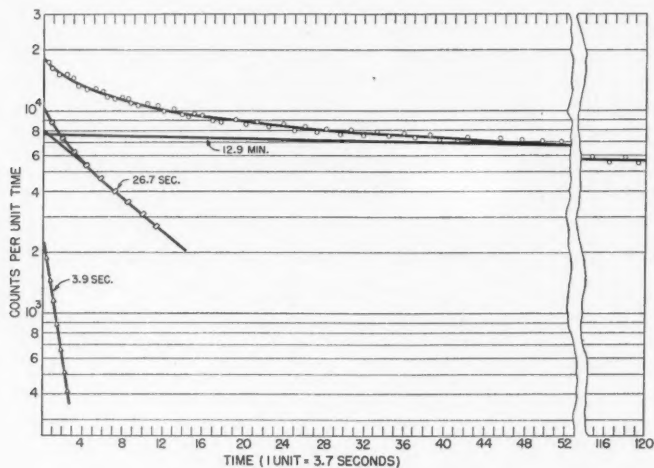


FIG. 2. Decay curve of irradiated iron cylinder.

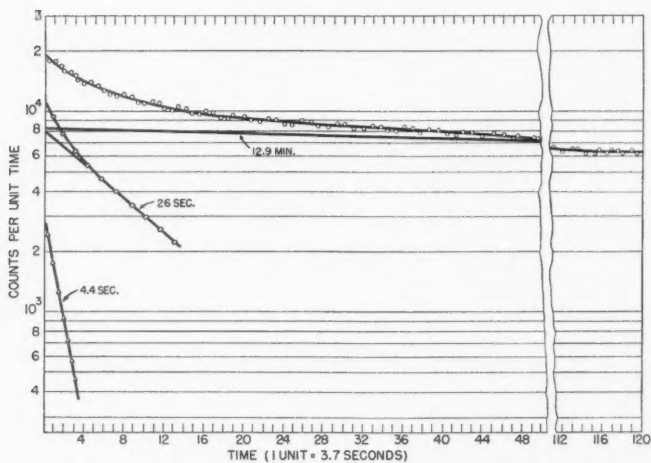


FIG. 3. Decay curve of normal carbon irradiated in an iron capsule.

Since it took approximately 1 sec. for the sample to leave the pile and the irradiation times were of 8 sec. duration, an activity which had a half life in the 1 sec. to 1 min. range would have been detected.

To set an upper limit on the cross-section of  $C^{14}$  for thermal neutron capture,  $Li^7$  (as lithium carbonate) was irradiated. A value of 33 millibarns (4) was taken as the cross section for the reaction  $Li^7(n, \gamma) Li^8$ . The amount of  $Li^7$

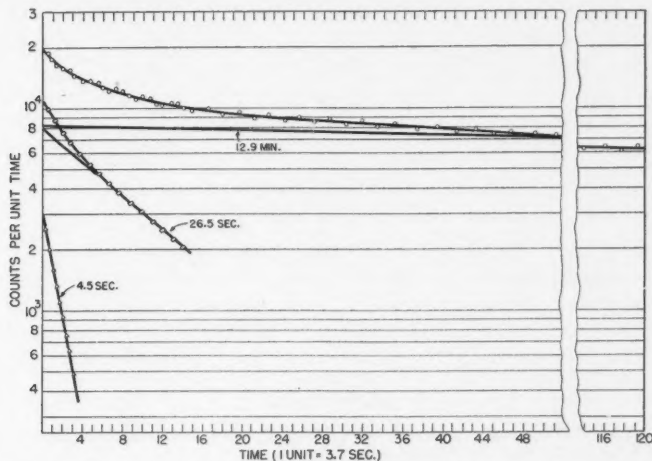


FIG. 4. Decay curve of carbon containing 6%  $C^{14}$ , irradiated in an iron capsule.

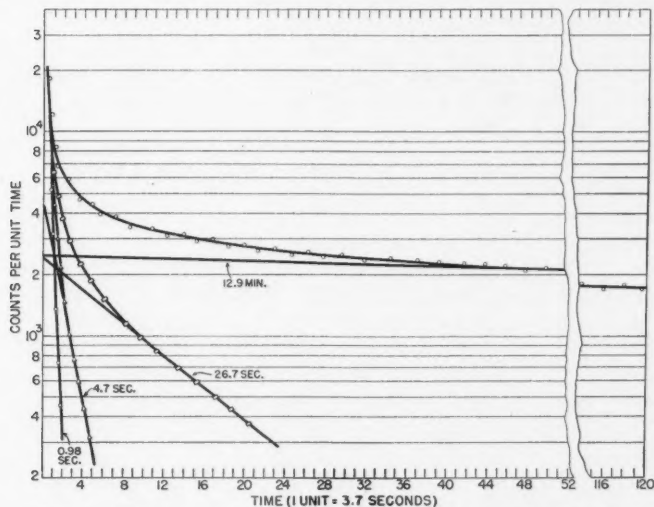


FIG. 5. Decay curve of lithium carbonate irradiated in an iron capsule.

irradiated ( $1.2 \times 10^{-7}$  gm.) corresponds to an equal absorption of neutrons for the weight of  $C^{14}$  used, assuming a cross section of 6 microbarns for the latter. The 0.88 sec. 12.7 Mev.  $Li^8$  activity was readily detected as is shown in Fig. 5.

To eliminate the possibility of nonresponse of the counting equipment to lower energies, lithium fluoride was irradiated. Both the  $\text{Li}^8$  and the 12 sec. 5 Mev.  $\text{F}^{20}$  were found in the amounts expected.

Even though the results are reproducible to better than 10%, it was assumed that the minimum increase in activity due to  $\text{C}^{15}$  which could have been detected was 20%. Using this as a reference, the cross section for capture by  $\text{C}^{14}$  was then calculated for various half lives of  $\text{C}^{15}$  in the range studied. It was assumed that the energy of  $\text{C}^{15}$  was greater than 3 Mev. so that significant absorption did not occur.

For a half life of 1 sec. the upper limit for the capture cross section of  $\text{C}^{14}$  is 0.05 microbarns. This increases to 0.6 microbarns for a half life for  $\text{C}^{15}$  of 1 min.

$\text{C}^{14}$  has eight neutrons in the nucleus and thus is one of the magic number nuclei suggested by Mayer (7) and others. Although one might expect the cross section to be low for this reason, yet our upper limit of less than 1 microbarn is 20 times smaller than the smallest cross section reported for any nuclide, namely for  $\text{N}^{15}$ .

### References

1. BETHE, H. The science and engineering of nuclear power. Addison-Wesley Press Inc. Cambridge, Mass. p. 381.
2. BONNER, F. T. and THOMPSON, S. O. Private communication.
3. HUDSPETH, E. L., SWANN, C. P., and HEYDENBURG, N. P. Phys. Rev. 77: 736. 1950.
4. HUGHES, D. J., HALL, D., EGGLE, C., and GOLDFARB, E. Phys. Rev. 72: 646. 1947.
5. KONOPINSKI, J. Rev. Mod. Phys. 15: 209. 1943.
6. LIBBY, W. F. Private communication.
7. MAYER, M. Phys. Rev. 74: 235. 1948.
8. TOLLESTRUP, A., FOWLER, W. A., and LAURITSEN, C. C. Phys. Rev. 78: 372. 1950.
9. YAFFE, L. and STEVENS, W. H. Phys. Rev. 79: 893. 1950.



# SUR LA CORRELATION ENTRE LES DISCONTINUITÉS DANS LA VALLÉE DES MASSES ET LES ENVELOPPES NUCLÉAIRES. APPLICATION À L'ÉTUDE DE LA SYSTÉMATIQUE $\alpha^1$

PAR A. BRONIEWSKI

## Sommaire

On montre que les discontinuités qui se produisent dans la variation régulière de la vallée des masses en fonction de  $A$  se rattachent approximativement, dans la première partie du tableau périodique, au phénomène de saturation des enveloppes protoniques et dans sa deuxième partie, à la saturation des enveloppes neutroniques dont l'ordre de succession a été établi par G. Mayer.

L'hypothèse de l'existence d'une discontinuité dans la région des éléments transuraniens est discutée. Une telle discontinuité aurait pour conséquence de modifier les prédictions actuelles faites sur les énergies  $\alpha$  des éléments transuraniens.

## I. Introduction

Il est bien connu que si l'on représente toutes les variétés nucléaires naturelles dans un plan rectangulaire Neutron-Proton, on obtient une multitude de points compris dans une bande assez étroite variant en première approximation d'une façon continue avec le nombre de masse  $A$ .

On sait aussi que les noyaux légers qui correspondent à des valeurs de  $Z \leq 20$  ont tendance à se grouper autour de la bissectrice des axes N-P, mais que, par suite de la répulsion Coulombienne, tous les isotopes plus lourds s'écartent de plus en plus de cette bissectrice, leur nombre de neutrons excédant celui des protons. Ainsi pour l' $U^{238}$  le nombre isotopique  $I$  ( $I = A - 2Z = N - Z$ ) atteint la valeur 54.

## II. Etude des discontinuités dans la vallée des masses

Nous allons examiner maintenant plus en détail l'allure de la vallée des masses dans le plan N-P. Un diagramme qui semble faciliter cette étude est représenté sur la Fig. 1. On y a fait figurer seulement les isotopes par le plus léger et le plus lourd de tous les éléments de  $Z$  pair et les points figuratifs ont été reliés par les lignes épaisses dans le but de faire ressortir les limites de stabilité dans chaque région. Avec Guggenheimer (6), nous appellerons ces limites les limites extérieures de stabilité. D'autre part, les noyaux de  $Z$  impair qui, n'étant représentés que par un ou par deux isotopes stables, sont particulièrement intéressants car ils marquent très sensiblement le fond de la vallée des masses (minimum des paraboles de Bohr-Wheeler) ont aussi été représentés et reliés entre eux par des lignes en pointillé (2). Un tel diagramme rend compte clairement de la double tendance qui préside à l'édification des noyaux stables. On sait en effet qu'approximativement dans la première moitié de la vallée des masses les noyaux stables s'édifient en moyenne par adjonction d'un neutron

<sup>1</sup> Manuscrit reçu le 17 octobre 1950.

Contribution de la Division de Physique, Conseil National des Recherches, Ottawa, Canada.  
Issue par le C.N.R. No. 2355

pour chaque proton ajouté, tandis qu'il faut deux neutrons pour chaque proton additionnel en vue d'atteindre une configuration comparablement stable au point de vue radioactivité  $\beta$  dans la dernière partie de tableau périodique.

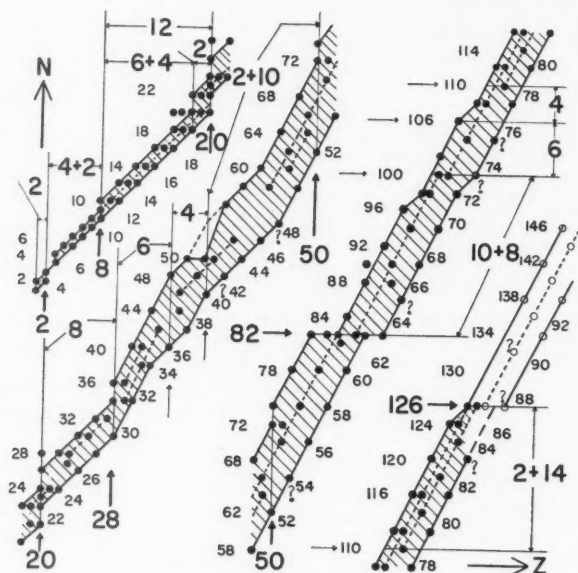


FIG. 1. Diagramme indiquant les limites de stabilité de la vallée de masse et leur liaison avec les enveloppes nucléaires dans le schéma de Mayer.

Lorsque la première de ces tendances intervient on voit, sur la Fig. 1, que les noyaux comparables entre eux au point de vue radioactivité  $\beta$  (c.a.d., ceux qui de  $Z$  impairs sont situés au fond de la vallée de masse et de même les noyaux qui marquent les limites extérieures de stabilité) se placent très exactement sur les droites de pente 1; lorsque c'est la deuxième tendance qui devient prépondérante, ils se placent sur les droites de pente 2. C'est d'ailleurs en considérant la régularité remarquable dans l'édification des noyaux lourds et très lourds, les moins riches en neutrons, (tombant sur les lignes épaisses inférieures de la Fig. 1) que Duckworth et collaborateurs (4) ont pu découvrir un nouvel isotope stable du platine, et l'existence probable de plusieurs autres isotopes rares qui sont suivis de points d'interrogation sur la Fig. 1.

L'examen de la Fig. 1 montre cependant que "le régime pente 1" et "le régime pente 2" s'applique d'une façon continue qu'à une portion, assez limitée de la vallée des masses ne correspondant environ qu'à dix éléments consécutifs. La preuve en est fournie par les brusques déplacements des limites extérieures de stabilité qui se produisent en plusieurs endroits du tableau et qui seront étudiés en détail par la suite. Notons dès maintenant que ces déplacements ne

se produisent pas de la même manière pour les deux régimes de stabilité considérés. On voit en effet qu'avec le système de coordonnées adopté, les droites de pente 1 se déplacent à plusieurs reprises vers le haut (en suivant sur la vallée des masses le sens des  $Z$  croissants), c'est à dire, que la discontinuité apparaît pour une certaine valeur du nombre atomique  $Z$ . Au contraire où "le régime pente 2" régit la stabilité nucléaire, la vallée des masses se décale vers la droite, c'est à dire que la discontinuité se produit pour une certaine valeur de  $N$ .

L'interprétation la plus simple de cette situation pourrait être que "le régime pente 1," appliqué sans discontinuité à une portion étendue de la vallée des masses, conduirait à des noyaux trop pauvres en neutrons et ayant par conséquent tendance à subir la radioactivité  $\beta^+$ . Les réajustements se font donc dans le sens qui accroît en plusieurs "points critiques" de la vallée le nombre isotopique  $I$ . Par contre, il semble que les noyaux qui s'édifient par l'adjonction de deux neutrons par proton arrivent à contenir après plusieurs opérations semblables plus de neutrons qu'il n'est requis par les diverses conditions de stabilité nucléaire. En conséquence en d'autres points critiques des réajustements se produisent dans le but cette fois de diminuer le nombre isotopique.

Passons maintenant à la détermination exacte de ces points critiques où la variation régulière de la vallée des masses se trouve interrompue.

Ellis (5) a rattaché l'apparition des discontinuités aux nombres 20, 50 et 82 neutrons qui correspondent aux "nombres magiques" bien connus et aussi aux nombres 32, 60 et 100 neutrons. Ellis n'a pas cru devoir associer les "nombres magiques" des protons aux discontinuités dans la vallée des masses. Il nous semble au contraire qu'il faille relier ces discontinuités à la fois aux nombres magiques de neutrons et aux nombres magiques de protons en ayant soin toutefois de bien préciser les régions du tableau périodique qu'on considère.

#### *A—Discontinuité se produisant à la saturation des enveloppes protoniques*

Considérons d'abord l'allure de la vallée des masses dans la région des éléments très légers. On sait que le proton et l'He 3 sont les deux seuls noyaux stables ayant le nombre isotopique  $I$  négatif, égal à  $-1$ ; aussi ils se placent sur la portion de droite de pente 1 située au dessous de la bissectrice des axes  $N$ - $P$ . Ensuite, et jusqu'à l'oxygène, il existe un régime où les noyaux se situent sur deux droites de pente 1, la droite inférieure correspondant à la bissectrice des axes et la droite supérieure aux noyaux de  $I = 1$ . A partir de l'oxygène ( $Z = 8$ ) la limite supérieure de stabilité se déplace encore vers le haut d'une unité, les noyaux situés sur cette droite ayant le nombre isotopique égale à 2. En d'autres termes, la vallée des masses subit deux premiers déplacements vers le haut pour les deux premiers nombres magiques de protons, 2 et 8. Ces nombres n'ont pas été mentionnés par Ellis, effectivement aucun déplacement similaire n'est observable pour ces deux nombres magiques (2 et 8) de neutrons.

En continuant à suivre la vallée des masses dans le sens des  $Z$  croissants on voit qu'il se produit d'abord, avec 18 protons, un déplacement de la limite

supérieure de stabilité vers le haut, de deux unités et ensuite, pour  $Z = 20$ , un autre déplacement vers le haut de la même importance mais intéressant, cette fois, les deux limites extérieures de stabilité.

On peut essayer de rattacher la première discontinuité au nombre magique de 20 neutrons comme le fait Ellis (il faudrait alors admettre que le déplacement se fait à gauche sur l'axe horizontal  $N = 20^*$ ) ou comme nous le préférons au fait que le nombre 18 correspond à la saturation des deux premières sous-enveloppes protoniques (comptant 6 et 4 états possibles) s'édifiant à partir de l'oxygène. De toute façon même si on l'admet qu'un déplacement de la vallée des masses se produit pour 20 neutrons la deuxième discontinuité signalée ci-dessus doit être incontestablement rattachée au nombre magique de 20 protons.

L'examen de la Fig. 1 montre ensuite qu'entre les axes  $Z = 20$  et  $Z = 28$ , les limites extérieures de stabilité obéissent encore strictement au "régime pente 1". La discontinuité qui se produit pour  $Z = 28$  est de double nature; d'une part la limite supérieure de stabilité se déplace vers le haut de deux unités, d'autre part à partir de l'axe  $Z = 28$  apparaît pour la première fois la tendance à l'édification des noyaux stables suivant le mode que nous avons convenu d'appeler "régime pente 2". Il est intéressant de remarquer qu'avec 28 protons la sous-enveloppe qui s'édifie à partir du calcium ( $Z = 20$ ) et comprenant 8 états se trouve saturée. Il existe même des indications expérimentales prouvant que la configuration de 28 nucléons correspond à un arrangement de nucléons particulièrement stable (3). Notons aussi qu'il n'y a pas de discontinuité dans la vallée des masses pour 28 neutrons.

Le "régime pente 2" ne se continue que pour quelques éléments à partir de  $Z = 28$ . Après  $Z = 34$  "le régime pente 1" apparaît de nouveau jusqu'à environ  $Z = 46$ . A partir de cette valeur et pour tous les éléments suivants on ne rencontre plus que la tendance d'adjonction de deux neutrons par proton. On peut noter qu'avec  $Z = 34$  la sous-enveloppe comportant 6 états qui s'édifie après le nickel ( $Z = 28$ ) se trouve saturée. Par contre le changement de pente qui se produit pour  $Z = 46$  ne peut être rattaché à aucun effet de saturation d'enveloppe nucléaire tout au moins dans le schéma de Mayer (7).

La Fig. 1 montre que la limite supérieure de stabilité s'affaisse avec  $Z = 38$ ; ce fait doit être relié à l'instabilité des isotopes de strontium contenant plus de 50 neutrons. Cette perturbation dans la vallée des masses se produisant pour 50 neutrons et qui a été signalée par Ellis, apparaît cependant comme un effet purement local n'impliquant ni changement de pente ni translation générale du fond de la vallée comme en témoigne, dans cette région, l'examen de la ligne pointillée reliant les éléments de  $Z$  impairs.

La discontinuité suivante dans la vallée des masses, la dernière à se produire suivant un axe vertical, c'est à dire, pour un nombre donnée de protons, cor-

\* Il faut remarquer que si on retient cette hypothèse et modifie en conséquence la Fig. 1, l'extension vers le haut de la limite supérieure de stabilité apparaît déjà pour  $Z = 16$ .

Nous sommes probablement ici dans une région du tableau où les limites de stabilité se trouvent influencées à la fois par une configuration stable en protons et en neutrons.

respond au nombre magique de 50 protons. La Fig. 1 montre que cette discontinuité consiste en une extension vers le haut de deux unités de la limite supérieure de stabilité. La considération de la ligne de stabilité  $\beta$  maximum indiquée par les noyaux de  $Z$  impairs montre que cet effet est aussi accompagné d'une translation analogue du fond de la vallée des masses. Nous venons de voir qu'aucun effet semblable ne se produit pour 50 neutrons.

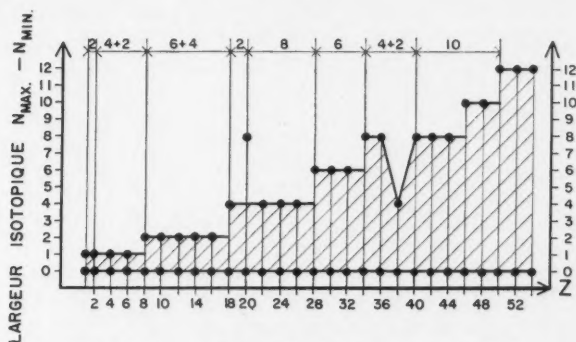


FIG. 2. Largeur isotopique  $N_{\max} - N_{\min}$  en fonction de  $Z$ .

La Fig. 2 résume la corrélation entre la variation de l'extension verticale de la vallée des masses et les nombres de protons qui correspondent à la saturation des enveloppes et des sous-enveloppes protoniques, c'est à dire, aux nombres magiques et ce que l'on pourrait appeler "sous-nombres magiques". Cette figure montre en fonction du nombre de protons "la largeur isotopique" des éléments de  $Z$  pairs. Avec Guggenheimer (6) nous entendons par cette grandeur la différence entre le nombre maximum et minimum de neutrons pouvant être liés à un élément donné. Une telle représentation a surtout l'avantage de bien montrer la constance de la largeur isotopique, à l'intérieur d'un interval de la vallée de masse qui correspond à une enveloppe, une sous-enveloppe ou une somme de sous-enveloppes protoniques données. En d'autres termes, la Fig. 2 indique que la largeur isotopique ne varie pas à l'intérieur d'une enveloppe, c'est à dire au cours de la saturation d'une enveloppe, sauf comme nous l'avons signalé plus haut pour  $Z = 48$ , et pour  $Z = 38$  cette dernière exception étant due à l'effet de 50 neutrons. Naturellement comme pour la Fig. 1, l'ordre de succession des enveloppes adopté dans la Fig. 2 est celui de Mayer (7).

#### *B—Discontinuités se produisant à la saturation des enveloppes neutroniques*

En examinant l'allure de la vallée des masses à droite de la discontinuité qui se produit pour le nombre magique de 50 protons on voit apparaître le plus important décalage de tout le tableau périodique à savoir celui qui a lieu pour 82 neutrons. Cette nouvelle discontinuité bien visible sur la Fig. 1 a été reproduite en détail sur la Fig. 3. Cette dernière figure montre qu'à partir de

l'axe  $N = 82$  la limite supérieure de stabilité se trouve déplacée vers la droite de 3 unités, et la limite inférieure de 2 unités. En d'autres termes, cette discontinuité, non seulement est différente de celles qui ont été étudiées jusqu'ici parce qu'elle se produit cette fois pour un nombre magique de neutrons et non pour un nombre magique de protons, mais aussi parce qu'elle s'opère dans le sens de la décroissance du nombre isotopique 1.

Les lignes pointillées épaisses de la Fig. 3 indiquent ce que serait l'allure de la vallée de masse si le réajustement s'était produit pour 58 protons, c'est à dire, à l'endroit de la saturation de la sous-enveloppe protonique s'édifiant après le nombre magique de 50 protons et comptant 8 états.

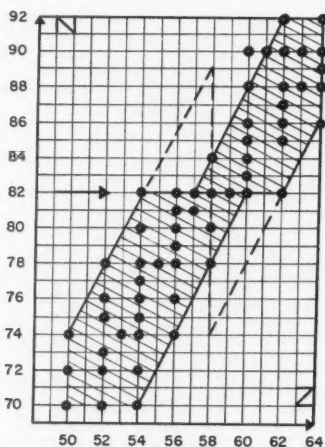


FIG. 3. Limites de stabilité dans la région de 82 neutrons.

Le schéma de Mayer prévoit, après le nombre magique de 82 neutrons, deux sous-enveloppes comptant 10 et 8 états possibles. Or, il se trouve que pour 100 neutrons ( $82 + 10 + 8 = 100$ ) la vallée de masse semble subir (5) une nouvelle discontinuité s'effectuant également vers la droite, comme dans le cas de la discontinuité précédente, mais moins prononcée. Cette discontinuité apparaît d'ailleurs comme certaine si l'on considère les droites pointillées de pente 2 qui relient les isotopes de  $Z$  impair et qui se brisent avec l'axe de 100 neutrons. Elle affecterait aussi la limite inférieure de stabilité si l'isotope de hafnium avec 100 neutrons, le Hf 172, était stable comme cela semble probable selon le raisonnement de Duckworth (4).

Avec 106 neutrons la sous-enveloppe neutronique suivante de 6 états est saturée; il semble encore qu'on puisse établir une corrélation entre ce fait et le déplacement vers la droite de la limite supérieure de stabilité qui se produit pour 106 neutrons et qui est visible sur la Fig. 1.



Enfin, l'examen des lignes pointillées fournit l'indication que pour 110 neutrons le fond de la vallée des masses se déplace vers la droite d'une unité. Ce nombre coïncide avec celui pour lequel la saturation de la sous-enveloppe neutronique s'édifiant après 106 neutrons, et comptant quatre états, est atteinte. Il est bien connu qu'aucun des noyaux contenant plus que le nombre magique de 126 neutrons n'est stable, aussi semble-t-il a priori plus difficile de suivre les limites extérieures de stabilité dans cette région de la vallée des masses en vu de les comparer aux limites de stabilité valables au dessous de l'axe  $N = 126$ . On peut cependant considérer dans la région de l'instabilité naturelle une ligne qui est comparable à la limite supérieure de stabilité des noyaux stables, à savoir celle qui relie les isotopes de Ra226, Th232, et de l'U238, stables par rapport à l'émission  $\beta$  et seulement radioactifs  $\alpha$  avec une très longue période (1). (Sur la Fig. 1 ces noyaux aussi que tous les autres noyaux étudiés ci-dessous dans la région de l'instabilité naturelle ont été indiqués sous forme de cercles blancs.) Cette ligne se trouve être une droite de pente 2, qui prolongée vers le bas, ne se recouvre pas avec la ligne de stabilité qui intéresse les noyaux avec  $N = 126$  mais se situe à droite de cette ligne. La même circonstance se retrouve pour le fond de la vallée des masses. En effet Seaborg et coll. (8) ont récemment publié une liste des noyaux  $\beta$  stables dans la région de l'instabilité naturelle montrant qu'à l'exception d'astatine les éléments de  $Z$  impair ont seulement un seul isotope  $\beta$  stable. Ces isotopes ont été reliés par une ligne pointillée sur la Fig. 1. On s'aperçoit que ces noyaux se situent à nouveau sur une droite de pente 2 décalée à droite par rapport à la ligne valable au dessous du plomb, le décalage se produisant pour 126 neutrons. Finalement la liste de Seaborg permet de considérer, dans la région de l'instabilité naturelle les noyaux  $\beta$  stables pauvres en neutrons qui sont comparables aux isotopes tombant sur la ligne inférieure de stabilité des autres régions. Ces noyaux, indiqués sur la Fig. 1 se situent encore sur une droite de pente 2 subissant elle aussi un déplacement d'une unité à droite à compter de l'axe  $N = 126$ .

### III. Discussion

#### A. Interprétation générale

L'étude précédente permet de faire quelques remarques générales au sujet de l'influence des enveloppes nucléaires sur l'allure de la vallée de masse.

Un fait très significatif semble être que la saturation des enveloppes, aussi bien protoniques que neutroniques, ne coïncide pas dans tous les cas avec un événement marqué dans l'allure de la vallée; ces exceptions s'observent pour  $Z = 6, 14$  et  $40$  (fin des sous-enveloppes  $1p/3/2$ ,  $1d/3/2$  et  $2p/1/2$ ) dans la région gouvernée par le "régime pente 1" et pour  $N = 92$  et  $112$  (fin des sous-enveloppes neutroniques  $1h9/2$  et  $3p1/2$ ) dans la région: "régime pente 2". Réciproquement nous avons vu que la discontinuité se produisant pour  $Z = 46$  n'est pas en corrélation avec la saturation d'une enveloppe nucléaire.

Tenant compte de ces exceptions il semble qu'on puisse avancer l'hypothèse selon laquelle les régions de la vallée de masse qui correspondent à la saturation



d'enveloppes jouent le rôle de régions privilégiées ou l'achèvement d'une discontinuité se trouve favorisée en supposant toutefois que le réajustement du rapport  $N/P$  au voisinage de ces positions se fait sentir. Si ce rapport, au point de saturation d'une enveloppe nucléaire correspond aux meilleures conditions de stabilité requises aucun effet de discontinuité à cet endroit n'est visible. Par contre si le rapport  $N/P$  devient trop inadéquat pour assurer la stabilité nucléaire au cours de l'édification d'une enveloppe, la discontinuité apparaît avant la saturation de celle-ci. Cette dernière hypothèse est proposée pour rendre compte de la discontinuité se produisant pour  $Z = 46$ . On peut remarquer que cette discontinuité s'est produite au cours de l'édification d'une "grande sous-enveloppe" comptant 10 états possibles. Si la saturation était atteinte pour  $Z = 44$  ou  $Z = 48$  il est vraisemblable que la discontinuité se fut produite pour l'une de ces deux valeurs.

En ce qui concerne la différence dans l'apparition des discontinuités qui se produisent dans la première partie de la vallée de masse, au point de saturation des enveloppes protoniques, et dans la deuxième partie au point de saturation des enveloppes neutroniques, elle est une étroite corrélation, comme il a été déjà remarqué, avec la nature du régime suivant lequel s'édifient les noyaux. On a vu en effet que le "régime pente 1" favorise l'apparition des discontinuités pour les nombres magiques et "sous-magiques" de protons tandis que dans le domaine de validité du "régime pente 2" toutes les discontinuités (sauf pour  $Z = 50$ ) se produisent pour les nombres magiques et "sous-magiques" de neutrons.

On peut aussi faire une remarque se rapportant à la fréquence de l'apparition des discontinuités. En effet l'examen de l'ensemble de la Fig. 1 montre que les discontinuités se produisent avec une plus grande fréquence dans la première partie de la vallée de masse que dans la seconde. On peut y voir la preuve que le "régime pente 2" qui gouverne les noyaux lourds est un mode d'édification des noyaux qui vérifie davantage les diverses conditions de stabilité que "le régime pente 1" ne le fait dans la région des noyaux légers et moyens.

#### *B. Applications à l'étude de la systématique $\alpha$*

L'étude qui vient d'être faite sur la corrélation entre la saturation des enveloppes nucléaires et l'apparition des discontinuités dans la vallée de masse suggère quelques idées nouvelles dans le domaine de la radioactivité naturelle  $\alpha$ .

Rappelons d'abord que dans la région de l'instabilité naturelle nous avons pu constater que 1° la vallée de masse obéit au régime "pente 2"; 2° une discontinuité se produit pour le nombre magique de 126 neutrons qui déplace les limites extérieures de stabilité d'une unité à droite par rapport aux limites valables pour plusieurs éléments au dessous du plomb. La question qui se pose tout naturellement est de savoir pour combien de noyaux avec  $N > 126$  "le régime pente 2" se continue sans subir une nouvelle discontinuité qui selon toute vraisemblance se produit suivant un axe horizontal, c.à.d., pour un nombre donné de neutrons (cf. sections IIB et III).

Le schéma de Mayer (7) prévoit après le nombre magique de 126 nucléons une sous-enveloppe comptant 12 états (1i 11/2). La Fig. 1 montre cependant qu'à l'endroit de la saturation de cette sous-enveloppe, c.à.d., pour 138 neutrons, aucun déplacement de la vallée de masse ne se produit. Cette circonstance n'a cependant rien d'étonnant et entre dans le cadre des exceptions discutées dans la section IIIA où la saturation d'enveloppe ne s'accompagne pas de discontinuité dans la vallée de masse. D'autre part, si on examine les étendues des intervalles durant lesquels les limites extérieures de stabilité se continuent sous forme de droite de pente 2 sans subir de discontinuité on arrive à la conclusion que l'accord entre les conditions de stabilité et le régime pente 2 est d'autant meilleur que les noyaux soumis à ce régime sont plus lourds. Comme au dessous de l'axe  $N = 126$  on observe une région où les limites extérieures de stabilité se poursuivent sans discontinuité pour 20 neutrons consécutifs, on peut s'attendre à un interval continu encore plus étendu au dessus de cet axe, c.à.d., qu'une discontinuité semble improbable avant que soit atteint un nombre de neutrons au moins égal à  $126 + 20 = 146$ .

Tenant compte de ce raisonnement qualitatif et en déduisant du schéma de Mayer que la seconde sous-enveloppe s'édifiant après le nombre magique de 126 neutrons contient 10 états possibles, on est conduit à envisager le nombre de 148 neutrons ( $126 + 12 + 10$ ) comme pouvant correspondre à une nouvelle discontinuité dans la vallée de masse.

La Fig. 4 représente dans le plan N-P les noyaux  $\beta$  stables autour de l'axe  $N = 148$ ; ceux prévus par Seaborg et coll. (8) ont été suivis de points d'interrogation. On voit que les résultats expérimentaux concernant cette région transurienne de la vallée de masse sont insuffisants pour que l'on puisse se prononcer d'une manière certaine sur l'existence d'une discontinuité se produisant pour 148 neutrons. Par contre, il est remarquable que les prédictions

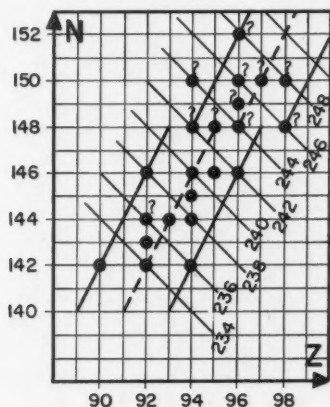


FIG. 4. Limites probables de stabilité  $\beta$  des noyaux transuraniens.

faites pour les noyaux contenant 148 neutrons en plus suggèrent l'éventualité d'une telle discontinuité, qui sur l'axe horizontal de 148 neutrons, se produirait d'une unité vers la droite et serait de ce fait comparable à celle qui existe pour 126 neutrons. La Fig. 4 montre les limites extérieures de stabilité  $\beta$  indiqués suivant les conventions adoptées pour la Fig. 1 dans l'hypothèse d'une telle discontinuité. On constate d'abord que le seul isotope de Bk prédit comme  $\beta$  stable, le Bk 247, se place sur la nouvelle ligne de stabilité  $\beta$  maxima et non sur l'ancienne. De plus, Seaborg prédit comme plus léger isotope  $\beta$  stable de Cf, le Cf 246, qui également tombe sur la ligne inférieure de stabilité tracée dans l'hypothèse d'une discontinuité se produisant pour 148 neutrons. Finalement le Cm 250 qui aurait dû être  $\beta$  stable si l'ancienne limite supérieure de stabilité était valable ne figure pas dans la liste précitée. Notons toutefois que Seaborg prédit comme  $\beta$  stable l'isotope 244 du Pu qui visiblement sur la Fig. 4 se situe en dehors de la nouvelle limite supérieure de stabilité.

Remarquons en terminant que l'hypothèse du nouveau décalage se produisant pour 148 neutrons suggère la revision des prédictions sur les propriétés des éléments transcuriens, prédictions faites en admettant implicitement la continuité des limites de stabilité dans cette région extrême de la vallée de masse.

En particulier, par extrapolation, Seaborg et coll. assignent 6.8 et 6.6 Mev. comme énergies des particules  $\alpha$  des isotopes 246 et 248 du Cf. Or dans l'hypothèse d'un déplacement de la vallée des masses pour 148 neutrons les isotopes précités se placeraient plus près du fond de la vallée des masses qu'en l'absence d'un tel déplacement ce qui est immédiatement visible sur la Fig. 4. En conséquence (ref. 8, p. 28) les énergies de leurs particules  $\alpha$  seraient plus faibles que 6.8 et 6.6 Mev. respectivement. C'est même probablement la détermination exacte des énergies des particules  $\alpha$  des isotopes transcuriens qui permettra en premier lieu par comparaison avec les prédictions de Seaborg de se prononcer sur la validité de l'hypothèse envisagée ici.

### Remerciements

L'auteur exprime sa vive reconnaissance au Conseil National des Recherches du Canada pour la bourse qui lui a été accordée et qui lui a permis d'entreprendre ce travail. Il remercie Monsieur D. Rushton pour son aide dans l'exécution des figures.

### Références

1. BRONIEWSKI, A. Compt. rend. 74: 1730. 1948.
2. BRONIEWSKI, A. Compt. rend. 228: 916. 1949.
3. BRONIEWSKI, A. Phys. Rev. 77: 846. 1950.
4. DUCKWORTH, H., BLACK, R., and WOODCOCK, R. Phys. Rev. 75: 1438. 1949.
5. ELLIS, C. B. Phys. Rev. 74: 1547. 1948.
6. GUGGENHEIMER, K. J. phys. radium 5: 252. 1934.
7. MAYER, M. G. Phys. Rev. 75: 1969. 1949.
8. PERLMAN, I., CHIORSO, A., and SEABORG, G. T. Phys. Rev. 77: 26. 1950.

## NUCLEAR DATA FOR LOW POWER RESEARCH REACTORS\*

The atomic energy authorities of Canada, the United Kingdom and the United States have agreed to the public release of certain information on low-power research reactors, including those nuclear properties of uranium of importance to the design and operation of such reactors. The following are the officially released data:

### 1. Thermal Neutron Cross Sections for Uranium

The following are currently accepted values in barns for an approximately Maxwellian neutron spectrum with a most probable neutron velocity of 2200 meters/second:

Thermal neutron cross section for	$U^{235}$	$U^{238}$	Natural $U$
Fission	545	0	3.9
Capture	100	2.6	3.3
Scattering	8.2	8.2	8.2

### 2. Natural Uranium Fission Cross Section between 0.7 Mev. and 5.0 Mev.

The cross section for fission of natural uranium by neutrons having energies between 0.7 Mev. and 5.0 Mev. is given in the accompanying figure. The curve has been drawn to fit the most reliable current experimental data.

### 3. Neutrons per Thermal Neutron Fission

$$\nu = 2.5 \pm 0.1 \text{ for } U^{235}$$

### 4. Prompt Neutron Energy Spectrum

The energy distribution of prompt neutrons resulting from the thermal neutron fission of  $U^{235}$  is given by the formula:

$$[\sinh \sqrt{2E}] \cdot \exp(-E),$$

where  $E$  is the neutron energy in Mev. in the laboratory system. This distribution function represents experimental data up to neutron energies of 13 Mev. with a maximum deviation of 15%.

### 5. Fast Fission Effect

The following are typical values of the fast fission contribution to the reactivity of research reactors:

- a. In a reactor of the "CP-2" or "GLEEP" type: 2.9%
- b. In a reactor of the "CP-3" or "ZEEP" type: 3.1%

*Note:* "CP-2" and "GLEEP" are low-power graphite, uranium reactors at the Argonne National Laboratory and Harwell, respectively.

"CP-3" and "ZEEP" are low-power heavy water, uranium reactors at Argonne and Chalk River, respectively.

\*Issued as N.R.C. No. 2332.

### 6. Resonance Absorption Integral

An approximate empirical formula for the effective value of the resonance absorption integral in natural uranium is

$$\int \sigma_c(E)(dE/E) = 9.25 [1 + 2.67 (S/M)],$$

where the value is in barns, the integral is over the range of neutron energy from fission energy to thermal energy, and where  $S$  = uranium surface area in  $\text{cm}^2$  and  $M$  = uranium mass in grams.

It is hoped that during later declassification actions appropriate credit may be given to the large number of individuals in the U.S., U.K., and Canada who have contributed to knowledge of the above nuclear data.

Values of the neutron cross sections for uranium at energies other than thermal will not be released at this time except for that information released under item 2 above. Similar data on other fissionable nuclei will also remain "classified".

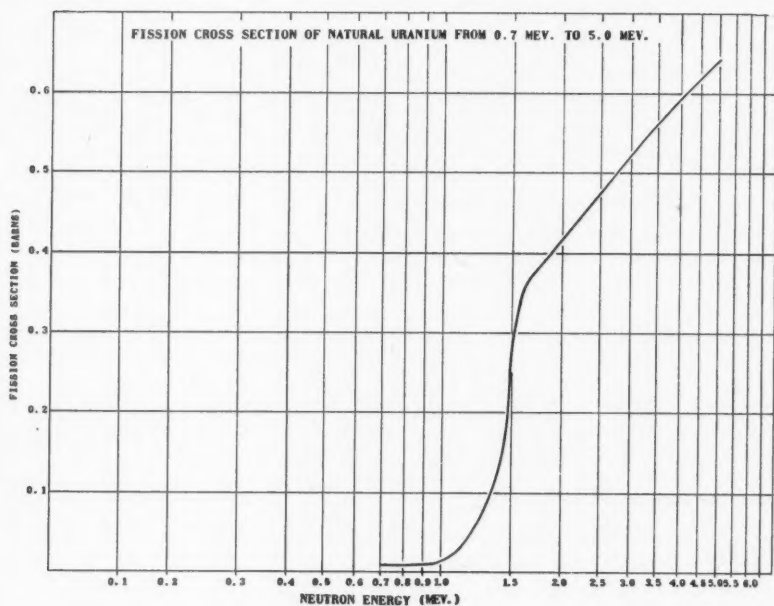
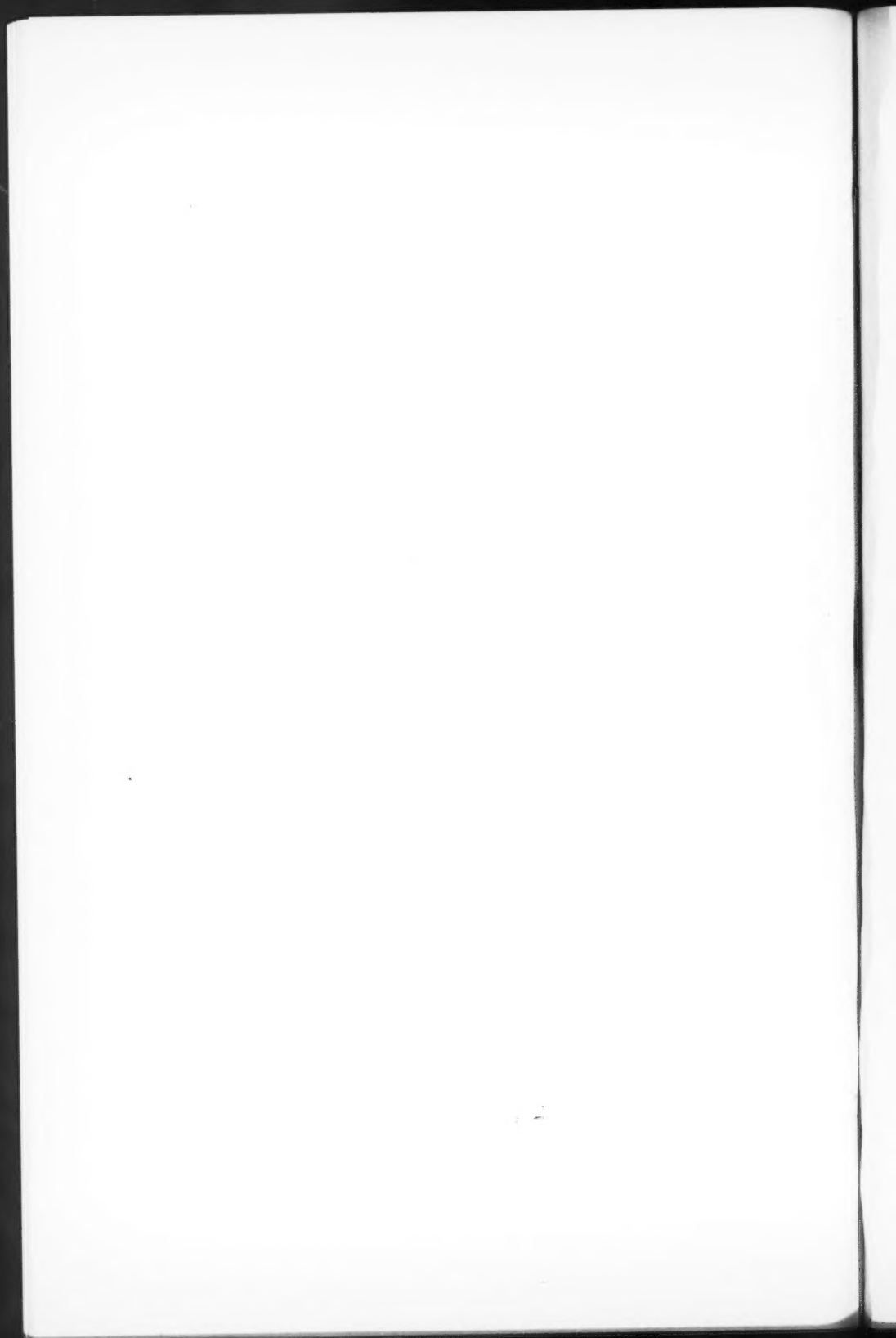


FIG. 1







## CANADIAN JOURNAL OF PHYSICS

### Notice to Contributors

**GENERAL:** Manuscripts should be typewritten, double spaced, and the **original and one extra copy** submitted. Style, arrangement, spelling, and abbreviations should conform to the usage of this Journal. Names of all simple compounds, rather than their formulas, should be used in the text. Greek letters or unusual signs should be written plainly or explained by marginal notes. Superscripts and subscripts must be legible and carefully placed. Manuscripts should be carefully checked before being submitted, to reduce the need for changes after the type has been set. If authors require changes to be made after the type is set, they will be charged for changes that are considered to be excessive. **All pages, whether text, figures, or tables, should be numbered.**

**ABSTRACT:** An abstract of not more than about 200 words, indicating the scope of the work and the principal findings, is required.

#### ILLUSTRATIONS:

(i) **Line Drawings:** All lines should be of sufficient thickness to reproduce well. Drawings should be carefully made with India ink on white drawing paper, blue tracing linen, or co-ordinate paper **ruled in blue only**; any co-ordinate lines that are to appear in the reproduction should be ruled in black ink. Paper ruled in **green, yellow, or red should not be used** unless it is desired to have all the co-ordinate lines show. Lettering and numerals should be neatly done in India ink preferably with a stencil (**do not use typewriting**) and be of such size that they will be legible and not less than one millimeter in height when reproduced in a cut three inches wide. All experimental points should be carefully drawn with instruments. Illustrations need not be more than two or three times the size of the desired reproduction, but the ratio of height to width should conform with that of the type page. **The original drawings and one set of small but clear photographic copies are to be submitted.**

(ii) **Photographs:** Prints should be made on glossy paper, with strong contrasts; they should be trimmed to remove all extraneous material so that essential features only are shown. Photographs should be submitted **in duplicate**; if they are to be reproduced in groups, one set should be so arranged and mounted on cardboard with rubber cement; the duplicate set should be unmounted.

(iii) **General:** **The author's name, title of paper, and figure number should be written in the lower left hand corner (outside the illustration proper) of the sheets on which the illustrations appear.** Captions should not be written on the illustrations, but typed on a separate page of the manuscript. All figures (including each figure of the plates) should be numbered consecutively from 1 up (arabic numerals). **Each figure should be referred to in the text.** If authors desire to alter a cut, they will be charged for the new cut.

**TABLES:** Each table should be typed on a separate sheet. Titles should be given for all tables, which should be numbered in Roman numerals. Column heads should be brief and textual matter in tables confined to a minimum. **Each table should be referred to in the text.**

**REFERENCES:** These should be listed **alphabetically by authors' names, numbered in that order, and placed at the end of the paper.** The form of literature citation should be that used in this Journal. **Titles of papers should not be given.** The first page only of the references cited should be given. **All citations should be checked with the original articles.** Each citation should be referred to in the text by means of the key number.

**REPRINTS:** Fifty reprints of each paper without covers are supplied free. Additional reprints, if required, will be supplied according to a prescribed schedule of charges. On request, covers can be furnished at cost.

Manuscripts should be addressed: *Canadian Journal of Physics,*  
*National Research Council,*  
*Ottawa, Canada.*

## Contents

	Page
The Absorption of Microwaves in Excited Hydrogen— <i>G. E. Reesor</i>	87
Meteorological Effects on Cosmic Ray Intensity and the Meson Spectrum— <i>D. C. Rose</i> - - - - -	97
Photoelectric Meteor Observations— <i>Barbara M. McKinley and D. W. R. McKinley</i> - - - - -	111
Study of Ionic Crystals Under Electron Bombardment— <i>D. E. McLennan</i> - - - - -	122
Energy Spectrum of Neutrons from a Thorium Active Deposit-Beryllium Source— <i>D. A. Bromley</i> - - - - -	129
Pulser for Cyclotron Oscillator— <i>W. H. Henry and J. D. Keys</i>	137
The Calibration of Platinum Resistance Thermometers in the Temperature Range 11° to 90°K— <i>J. M. Los and J. A. Morrison</i> - - - - -	142
The Raman Spectrum of Fluorine— <i>D. Andrychuk</i> - - - - -	151
Effect of Variable Mass of the Electron on the Space-Charge Limited Current in a Diode— <i>S. Visvanathan</i> - - - - -	159
On the Static Dielectric Constant of Dipolar Solids— <i>J. H. Simpson</i> - - - - -	163
Rotational Analysis of the $\gamma$ Band System of the NS Molecule — <i>P. B. Zeeman</i> - - - - -	174
An Attempt to Detect the Reaction $C^{14}(n, \gamma)C^{15}$ — <i>L. Yaffe and W. H. Stevens</i> - - - - -	186
Sur la Corrélation Entre les Discontinuités dans la Vallée des Masses et les Enveloppes Nucléaires. Application à l'Étude de la Systématique $\alpha$ — <i>A. Broniewski</i> - - - - -	193
Nuclear Data for Low Power Research Reactors— <i>Atomic Energy Project, Chalk River</i> - - - - -	203

